THESIS FOR THE DEGREE OF DOCTOR OF PHILOSOPHY

Development and performance evaluation of accident-tolerant coated fuel claddings for light water reactors

ANDREA FAZI

Department of Physics

CHALMERS UNIVERSITY OF TECHNOLOGY

Gothenburg, Sweden 2023

Development and performance evaluation of
accident-tolerant coated fuel claddings for light water reactors
ANDREA FAZI
ISBN 978-91-7905-781-7

Doktorsavhandlingar vid Chalmers tekniska högskola
Ny serie nr 5247
ISSN 0346-718X

Department of Physics
Chalmers University of Technology
SE-412 96 Göteborg
Sweden
Telephone +46 (0) 31-772 1000

Cover illustration

3D reconstructions of atom probe tomography data – Left: as-deposited nanolayered CrN-NbN coating. Right: as-deposited superlattice CrN-NbN coating. The presented boxes are 50x50 nm^2 in size and 20 nm thick. (Cr atoms are plotted in magenta, Nb atoms are plotted in orange).

Chalmers Reproservice
Göteborg, Sweden 2023

Development and performance evaluation of accident-tolerant coated fuel claddings for light water reactors

Andrea Fazi
Department of Physics
Chalmers University of Technology

ABSTRACT

The development of accident tolerant fuel has the aim of providing nuclear fuels able to endure severe accident conditions. Research in this field has also sparked a wave of material renewal in the nuclear industry that had been delayed for the last few decades. Climate change is an ever-growing public concern, and policies about greenhouse gas emissions are becoming more stringent both at the national and international level. Nuclear energy produces very low carbon emissions and the successful development of new accident tolerant materials might play a role in making this technology a viable solution to this global issue. Coated zirconium claddings are one of the most promising candidates as a near-term response to the need for accident tolerant materials. These coatings can be produced via a range of different technologies, but two main techniques are being currently employed for the development of such coatings: cold spray deposition and physical vapour deposition (PVD). In cold spray, high pressure gas is fed through a nozzle together with a powder. Powder particles are accelerated up to 1200 m/s and directed to the substrate, in this case cladding tubes made of zirconium alloy. In PVD, the coating material is evaporated from a target and sputtered onto the substrate as atoms or ions. The resulting coated zirconium claddings are the subject of this work.

As-fabricated samples, autoclave tested material, and specimens tested under simulated accident conditions are characterized with atom probe tomography and a range of electron microscopy techniques. The scope of the investigation is to evaluate the performance of the coated claddings under operating conditions and in simulated accident conditions. Metallic Cr has emerged as the best candidate for accident tolerant coatings for pressurised water reactors. In this work, the focus was on Cr-coatings deposited with cold spray, which performed well in both tested environments. A passivating layer of chromia formed during autoclave exposure, and a protective scale of chromia prevented any oxidation of the Zr-substrate for up to 40 min in 1200 °C steam. The nature of the adhesion in cold spray coatings and the effects of this deposition method on the substrate were studied. The formation of a Cr_2Zr phase at the Cr/Zr interface was observed both under autoclave and simulated accident conditions. The search for an effective accident tolerant coating for boiling water reactors is more challenging and many coatings have been tested in autoclave, where PVD (Cr,Nb)N coatings showed the best performance under operating conditions. A 200 nm thick passivating oxide film composed of an outer Cr, Nb, Ni phase and an inner layer of oxidised coating was found after exposure.

Keywords: accident tolerant fuel, cold spray, PVD, Cr coating, nitride coatings, oxidation.

PREFACE

The work presented in this thesis was performed at the Division of Microstructure Physics, Department of Physics, Chalmers University of Technology, during the period 2018–2023, under the supervision of Associate Professor Mattias Thuvander, Professor Krystyna Stiller, Professor Hans-Olof Andrén, and Dr Mohammad Sattari.

This research is part of the SAFETY Project and it is financially supported by the Swedish Foundation for Strategic Research (SSF) (Grant number: EM16-0031). The studied material was supplied by Westinghouse Electric Sweden. The experimental work presented was performed at Chalmers Materials Analysis Laboratory (CMAL). Part of the Atom Probe data was collected at Karlsruhe Nano Micro Facility (KNMFi).

Parts of the work presented in this doctoral thesis have previously been published in a licentiate thesis by the same author.

LIST OF APPENDED PAPERS

i. *Characterization of as-deposited cold sprayed Cr-coating on Optimized ZIRLO™ claddings*
A. Fazi, H. Aboulfadl, A.H.S. Iyer, M. Sattari, K.M. Stiller, P. Lokhande, M. Thuvander, H.O. Andrén
Journal of Nuclear Materials 549, p.152892 (2021)

ii. *Cold sprayed Cr-coating on Optimized ZIRLO™ claddings: the Cr/Zr interface and its microstructural and chemical evolution after autoclave corrosion testing.*
A. Fazi, K.M. Stiller, H.O. Andrén , M. Thuvander.
Journal of Nuclear Materials 560, p.153505 (2022)

iii. *Performance and evolution of Cold Spray Cr-coated Optimized ZIRLO^{TM} claddings under simulated loss-of-coolant accident conditions*
A. Fazi, M. Sattari, K. Stiller, H.-O. Andrén, M. Thuvander.
Accepted for publication in Journal of Nuclear Materials

iv. *Comparing CrN and TiN Coatings for Accident-Tolerant Fuels in PWR and BWR Autoclaves*
A. Fazi, P. Lokhande, D.A. Lopes, K. Stiller, H.-O. Andrén, M. Thuvander.
Journal of Nuclear Engineering, 3(4), p.321–332 (2022)

v. *CrN-NbN nanolayered coatings for enhanced accident tolerant fuels in BWR*
A. Fazi, M. Sattari, T. Boll, K. Stiller, H.-O. Andrén, D. A. Lopes, M. Thuvander.
In manuscript

CONTRIBUTIONS

My contributions to the papers are listed below:

i. I performed specimen preparation by FIB/SEM, most of the APT measurements, data analysis and interpretation, EBSD mapping, TKD mapping, TEM imaging, and wrote the paper with input from the co-authors. Nano-hardness measurements and HR-TEM were not performed by me.

ii. I performed specimen preparation by FIB/SEM, APT measurements, data analysis and interpretation, SEM imaging, EDS analysis, EBSD mapping, TEM imaging, and wrote the paper with input from the co-authors.

iii. I performed specimen preparation by FIB/SEM, data analysis and interpretation, SEM imaging, EDS analysis, EBSD mapping, TEM imaging, and wrote the paper with input from the co-authors.

iv. I performed specimen preparation by FIB/SEM, data analysis and interpretation, SEM imaging, EDS analysis, STEM imaging, and wrote the paper with input from the co-authors.

v. I performed specimen preparation by FIB/SEM, APT measurements, data analysis and interpretation, SEM imaging, EDS analysis, part of the TEM imaging, and wrote the paper with input from the co-authors.

LIST OF ACRONYMS

ADF	Annular dark field
AE	Auger electrons
APT	Atom probe tomography
arc-PVD	Arc discharge physical vapor deposition
ATF	Accident tolerant fuel
BCC	Body centred cubic
BF-TEM	Bright field TEM
BIB	Broad ion beam
BSE	Backscattered electrons
BWR	Boiling water reactor
CS	Cold spray
CVD	Chemical vapour deposition
DP	Diffraction pattern
EBSD	Electron backscattered diffraction
EELS	Electron energy loss spectroscopy
EFTEM	Energy filtered TEM
ESEM	Environmental SEM
FCC	Face centred cubic
FIB	Focussed ion beam
GIS	Gas injection system
HAADF	High angle annular dark field
HCP	Hexagonal close-packed
HiFi	High corrosion resistance and high Fe zirconium alloy ™
HWR	Heavy water reactor
IBR	Intermixed bonding region
IPF	Inverse pole figure
LOCA	Loss of coolant accident

LWR	Light water reactor
MS-PVD	Magnetron sputtering physical vapour deposition
OPZ	Optimized ZIRLO™
PVD	Physical vapor deposition
PWR	Pressurized water reactor
SAD	Selected area diffraction
SE	Secondary electrons
SEM	Scanning electron microscopy
SL	Superlattice
SPP	Secondary phase particle
STEM	Scanning TEM
TEM	Transmission electron microscopy
TKD	Transmission Kikuchi diffraction

TABLE OF CONTENTS

CHAPTER 1

INTRODUCTION

Nuclear energy represented approximately 10 % of the total world electricity production in 2021 and it is characterized by extremely low carbon emissions [1]. The effects of greenhouse gases are now becoming a global concern, and national and international regulatory bodies are issuing policies to drive change in the way electricity is produced. Nuclear power is one technology that can help in this transition. New reactor concepts, such as small modular reactors and fast neutron reactors, are being developed to improve two of the most problematic aspects of nuclear energy: the extremely high upfront costs of building new power plants and the production of nuclear waste [2]. However, the deployment of these new designs in commercial reactors will require several more years. Of the 438 nuclear power plants currently operable or in commercial operation, 368 are light water reactors (LWRs) – 307 pressurized water reactors (PWRs) and 61 boiling water reactors (BWRs). LWRs produce approximately 90 % of the total nuclear energy output. Beyond the existing plants, 57 additional nuclear power plants are currently being constructed around the world, particularly in China, India, Russia and the United Arab Emirates; of these, 51 are LWRs – 49 PWRs and 2 BWRs [1,3,4].

Since the Fukushima Daiichi accident in 2011, the concept of accident tolerant fuels (ATFs) has emerged in the nuclear industry with the intent of developing safer and more functional nuclear fuel designs for LWRs. ATFs should be able to better survive severe accident conditions while modernizing the nuclear industry. Coated claddings can provide improved corrosion resistance (both in normal operation and during an accident), and better abrasion resistance, without requiring extensive design changes to the current reactors. As such, coated claddings represent an effective short-term solution to the need for ATFs. Some of the materials studied in this work could become commercially available in the coming few years, and understanding how these materials behave is ever more relevant. Cr-coatings have attracted attention for their exceptional performance under PWR operating conditions and under simulated accident conditions. Cold spray (CS) is a novel technology used for additive manufacturing and coating deposition, and it is one method currently being used to deposit Cr-coatings for ATF applications. CS does not require vacuum or heating of the substrate, and it can be used to quickly grow dense coatings in a large range of thicknesses, making it a well-suited technique for large-scale production. The basics of LWRs and an introduction to ATFs are presented in Chapter 2. More details about the CS technology are reported in Chapter 3. An alternative coating deposition method is physical vapour deposition (PVD). PVD can also be used to deposit Cr-coatings for ATFs, but in this work, the incredible flexibility that PVD offers in terms of coating composition has been facilitated to test a wide range of coatings and to find a suitable ATF coating design for BWRs. More about PVD can be found in Chapter 4. In Chapter 8, the differences between PWR and BWR are analysed and the challenges associated to BWRs are highlighted. The search for an effective coating for BWR is a crucial part of the development of ATFs, and having the possibility to test a multitude of coating compositions was instrumental in the identification of (Cr,Nb)N coatings as an effective candidate.

In this work, CS Cr-coated zirconium cladding tubes, plus a multitude of cladding tubes coated with various PVD nitride coatings, including (Cr,Nb)N, are extensively studied through the employment of numerous characterisation techniques. As-fabricated samples, samples exposed to simulated operating PWR and BWR conditions, and samples tested under simulated accident conditions are examined with the main intent of collecting relevant data for the performance assessment of the different coating/substrate systems. The possibility of studying the same materials before and after exposure allowed to determine trends in the microstructural and chemical evolution of coatings and substrate. Analysing coated claddings tested in simulated accident environment was central to the development of ATFs. The materials and characterization techniques used are reported and explained in Chapter 7. A summary of the main results is given in Chapter 8.

1.1 AIM OF THE STUDY

During fuel rod operation, most of the evaluation of the rod conditions is performed combining models with the reading of certain external parameters. Building the models needed for this scope requires profound comprehension of all the phenomena that can occur on the coated cladding rod once it is in operation, for example, microstructural or chemical changes, and the rates at which these changes happen. Although the primary reason behind the potential adoption of coatings in nuclear fuels is to act as protection in case of a severe accident, these coatings need to perform at least as good as traditional materials in normal operation, especially in regard of oxidation. Determining rates and mechanisms by which the coating oxidises and is eventually consumed is another very important aspect needed to calculate fuel life.

Research questions:

Question 1: Do ATF coatings offer improved high-temperature steam oxidation resistance under accident conditions?

The principal design objective of coatings for accident tolerant fuels is protecting the Zr substrate from high temperature steam oxidation. The first step in the development of a coating is to test if it works. Many tests have been conducted for example on Cr-coatings where they have shown excellent ability to protect the substrate. The second step, often deemed less impactful but very important nonetheless, is to investigate all the transformation mechanisms and interaction between the environment and the coating. The oxidation rate, and the oxide scale microstructure, morphology, adhesion, and properties are all important parameters that are needed to be able to estimate for how long a coating can effectively protect the cladding and how much additional buffer time is offered by the coating in a severe accident scenario.

In *Paper III* we investigate the performance of CS-Cr coated Zr-claddings under simulated accident conditions.

Question 2: Is chromia stable in LWR operating environments?

Generally, chromia is one of the most commonly used oxides for corrosion protection of metallic materials. It is stable in most environments, dense and an effective barrier to oxygen diffusion, and it has a single possible crystalline structure. It is perfect for passivating the surface of any metallic industrial component, such chromia scale is usually obtained by adding Cr as an alloying element in steels and Ni-alloys. Pure metallic Cr is very brittle and is rarely used as bulk material, and as a consequence there are few studies about its corrosion behaviour in water at reactor temperature. Additionally, the other elements in the steel or Ni-alloy usually interact among themselves and with Cr in forming complex, layered, oxide scales composed of chromia and spinel-oxides. Chromia is considered the main diffusion barrier for oxidation, but, depending on the environment, the role of the other oxides cannot always be neglected. Pure Cr or CrN can only form Cr-oxides or Cr-oxynitrides. The question whether chromia, grown in the absence of other oxides is stable or not in LWRs needs to be investigated and understood. In order to protect the Zr-cladding from severe oxidation during an accident scenario, the Cr coating has to survive years of in-reactor nominal conditions. If chromia were to be unprotective in such environments, the chromia-forming coatings could dissolve or degrade, and would not be there in the event of an accident. If chromia would not work in LWR environment, it would be important to find a way of stabilizing the formation of a passivating chromia-like oxide scale.

In *Paper II* we study the performance of pure Cr in PWR water chemistry, while *Paper IV* deals with the difference between PWR and BWR water chemistry and its effects on corrosion. *Paper V* focuses on corrosion behaviour of (Cr,Nb)N PVD coatings in BWR reactor conditions.

Question 3: To what degree do coating and cladding interact during coating deposition, in reactor operation and under accident conditions?

Zr-claddings must have specific mechanical properties in order to work well in a reactor. The application of the coating could modify or change these properties. Additionally, any diffusion phenomena between coating and substrate could produce slow and continuous transformations during the fuel-rod life cycle. If these new materials are going to be used in commercial applications, their properties need to be fully understood and all active phenomena need to be studied. Under accident conditions, the coatings must provide additional protection against oxidation and other deterioration mechanism, but it is pointless to have a great coating if it reacts with the substrate and loses its properties or disappears. Hence, it is very important to focus on the cladding-coating interaction during an accident scenario as well.

Paper I focuses on the effects of CS deposition on the microstructure of the Zr-cladding. In *Paper II* and *Paper III* we study the coating-cladding interaction for CS-Cr coated claddings under reactor conditions and in an accident scenario, respectively. *Paper V* investigates the interaction between PVD (Cr,Nb)N and Zr-cladding in simulated BWR environment.

CHAPTER 2

ACCIDENT TOLERANT MATERIALS FOR LIGHT WATER REACTOR FUELS

2.1 LIGHT WATER NUCLEAR REACTORS

2.1.1 BASIC CONCEPTS

In a nuclear reactor, the heat produced by a controlled fission reaction is transferred to a coolant, the hot coolant is subsequently used to heat water so to produce steam, the steam is used to power a steam turbine that drives an electric generator and produces electricity. Some of the main elements of a nuclear reactor are: fuel, moderator, coolant, control rods, steam generator and containment. Uranium oxide (UO_2 or urania) is the basic fuel. Small pellets of UO_2 are arranged inside cladding tubes to form fuel rods. Many fuel rods assembled together form a fuel assembly. The coolant and the neutron moderator used in the core can vary, but it is most often water. Water in a nuclear reactor not only acts as a coolant transporting heat away from the core, but also acts as moderator. The role of the moderator is to slow down fast neutrons produced during fission and to reduce their mean free path so to cause more fission. In some reactors, deuterium-enriched water (heavy water) is used as coolant and moderator. These reactors are called heavy water reactors (HWRs). The reactors where normal water is used as coolant and moderator are instead referred to as light water reactors (LWRs). Inside the core of a LWR, fission is initiated and sustained by a neutron flux. To control the neutron flux, control rods are inserted into the core. Additionally, neutron adsorbers can be added to the cooling water. The coolant coming from the core is then directed to a steam generator where the heat from the fission reaction is used to produce high pressure steam fundamental for operating the steam turbine that ultimately generates power.

Table 2-1: Nuclear power in the world: number of reactors by type (2022) [1].

REACTOR TYPE		REACTORS IN OPERATION	REACTORS UNDER CONSTRUCTION
PWR	Pressurized Light-Water Moderated and Cooled Reactor	307	49
BWR	Boiling Light-Water Moderated and Cooled Reactor	61	2
PHWR	Pressurized Heavy-Water Moderated and Cooled Reactor	47	3
LWGR	Light-Water Cooled, Graphite Moderated Reactor	11	-
GCR	Gas Cooled, Graphite Moderated Reactor	8	-
FBR	Fast Breeder Reactor	3	3
HTGR	High Temperature Gas Cooled Reactor	1	-
TOTAL		**438**	**57**

LWRs can be further divided into pressurized water reactors (PWRs) and boiling water reactors (BWRs). PWR is the most common type of reactor (307 out of 438 of the total operable nuclear reactors in the world are PWRs), see Table 2-1. In this design, water acts both as moderator and coolant and it is circulated in two separate loops. In the primary cooling circuit, water flows through the core at high pressure and temperature (around 150 bar and 325 °C), while the secondary circuit is kept at lower pressures and used to generate steam. In BWRs, instead, a single water circuit is used. Water is let to flow in the core at 75 bar and 285 °C, and these conditions are designed to have about 12-15 % of the water in the top part of the core as steam. The same steam is used to drive the steam turbine. A schematic representation of PWR and BWR designs is presented in Figure 2-1.

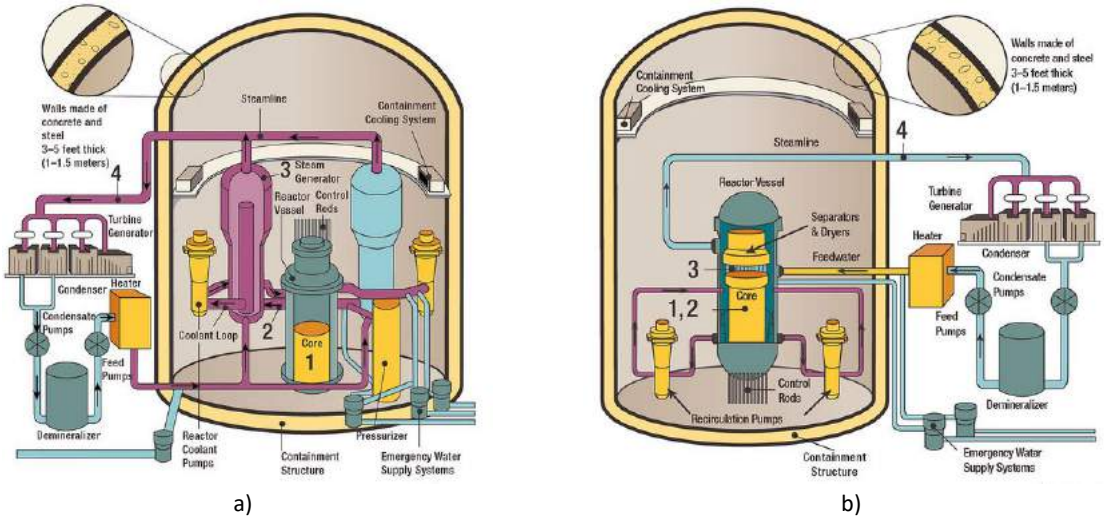

Figure 2-1: Schematics of light water reactor designs: PWR (a), and BWR (b). (Source NRC)

2.2 Zirconium alloys in the nuclear industry

2.2.1 Fuel assemblies

As anticipated in the previous section, the fuel of choice for LWRs is UO_2. UO_2 is used in the form of pellets, the pellets are piled vertically inside 4 m long cladding tubes made of zirconium alloys. Typically, Zircaloy-2 or HiFi are used for BWRs, and Zircaloy-4, M5 or ZIRLO are used for PWRs, see Table 2-2 for the alloy compositions. The cladding tube diameter is approximately 10 mm, while the cladding wall thickness can vary between 0.6 and 0.8 mm. Multiple tubes are stacked together using spacer grids, guide tubes and end plugs in arrays of 10x10 for BWRs and 14x14 or 17x17 in PWRs, forming a fuel assembly. An example of a fuel assembly is displayed in Figure 2-2. Up to 800 assemblies can be found in a BWR core and 150-300 assemblies for a PWR, amounting to 25–40 tonnes of zirconium in a LWR core [5,6]. The fuel assembly is designed to let water or steam flow through the fuel without the insurgence of turbulences, allowing the cooling of the core and extracting effectively the heat from the fission reaction to drive the steam turbine. The cladding is fundamental in keeping the UO_2 and the water apart, while containing fission products and avoiding the possibility of radioactive species ending up in the coolant. Efficient heat transmission across the cladding wall is

necessary for the heat generated inside the pellet to escape into the water. The cladding tube needs to withstand its own rod weight, it has to contract inwards at the beginning of its fuel cycle to accommodate the in-reactor pressure, and to expand in later stages to follow the swelling of the fuel pellets. All these requirements dictate minimum mechanical strength and good ductile creep behaviour. Additionally, to maintain a sustained fission reaction, any cladding material needs to have very low adsorption of thermal neutrons.

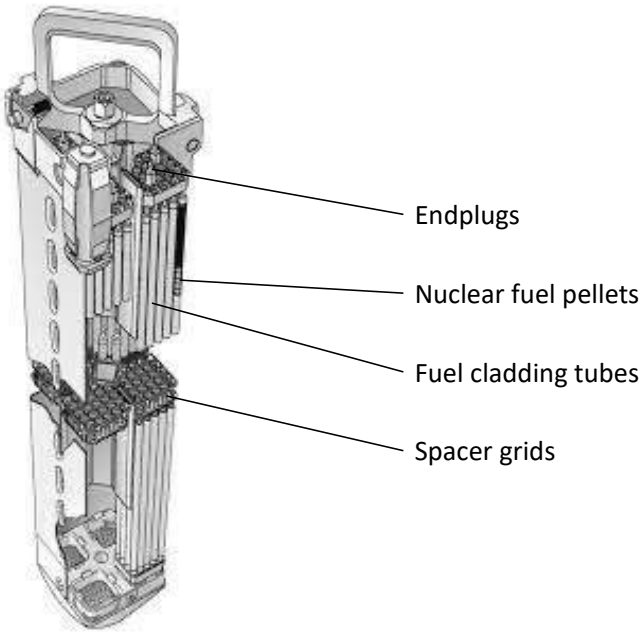

Figure 2-2: Schematic representation of a BWR fuel assembly and its components (courtesy of Westinghouse Electric Sweden)

2.2.2 ADVANTAGES OF ZIRCONIUM

During the first deployment of commercial nuclear power plants in the 1950s, steel was selected as cladding material, while zirconium was deemed too expensive and its use was limited to submarine reactors. By the mid-1960s though, the price of zirconium decreased enough to allow its use for civil power generation, and most commercial reactors switched from austenitic steels to zirconium alloys. The main reason for this change was the very low thermal neutron cross-section of Zr, which is of fundamental importance for the neutron efficiency and overall neutron economy inside the core. Zirconium is virtually transparent to thermal neutrons (which are the most likely ones to produce a fission event in the fuel) allowing them to travel through the cladding, which is a key factor in maintaining the fission reaction. Pure zirconium, though, has poor mechanical properties and low resistance to corrosion. For this reason, the aforementioned Zr-alloys were developed. Their mechanical properties were improved through solid solution hardening induced by Sn and O, and by the precipitation of second phase particles, SPPs. Corrosion resistance was greatly improved by the addition of Fe, Cr and Ni [7]. Heat treatments and careful forming are also important in providing optimal properties. For example, Optimized ZIRLO^{TM} claddings are produced with a fabrication process that involves forging of a billet, homogenization quenching of the billet, extrusion of the billet

into an extruded tube, followed by an annealing. The extruded tube is then reduced to the final thickness and diameter by alternating pilgering and annealing steps. Finally, a PRXA (partial recrystallization annealing) heat treatment is used to produce the desired equiaxed partially recrystallized microstructure [8]. This microstructure is characterized by the presence of larger grains (3–5 μm in size) surrounded by smaller sub-micron grains.

As a result of the finely tuned chemistry and microstructure of the claddings, the materials currently used perform well under normal operating conditions and most of the degradation mechanisms that affect zirconium alloys inside the core of a LWR are reasonably understood and controlled. One degradation mechanism that still occurs in operating reactors is debris fretting of the cladding tubes. In debris fretting, a foreign debris carried by the water gets trapped between the cladding tube and the spacer grid. When in this position, the water flow keeps moving the debris against the cladding tube resulting in wear and abrasion of the cladding. This phenomenon can even result in cladding perforation and it is the most common cause of rod failure [5,9].

Table 2-2: Chemical composition of some of the mostly used zirconium alloys [10].

Alloy	Composition (wt.%)						
	Sn	Fe	Ni	Nb	Cr	O (typical)	Zr
Zircaloy-2	1.2-1.7	0.07-0.20	0.03-0.08	-	0.05-0.15	0.125	balance
HiFi	1.2-1.7	0.25-0.50	0.03-0.08	-	0.05-0.15	0.125	balance
Zircaloy-4	1.2-1.7	0.18-0.24	-	-	0.07-0.13	0.125	balance
M5	-	<500 ppm	-	0.8-1.2	-	0.125	balance
ZIRLO	1.0-1.1	0.09-0.10	-	1.0-1.2	-	0.125	balance

2.3 Challenges and requirements for cladding materials

2.3.1 Aqueous oxidation and hydrogen pick-up

Water side oxidation of the cladding tube is one of the main factors limiting fuel burnup and consequently of fuel efficiency. During oxidation, hydrogen is produced, and some of this hydrogen enters the Zr-cladding and induces embrittlement. This link between oxidation, hydrogen pick-up and embrittlement is at the core of the oxidation limits imposed by regulatory bodies. A certain amount of residual ductility in the cladding is always required to withstand transients, loss of coolant accidents (LOCA) and other accident scenarios. Hence, a maximum limit to the oxidation of the cladding wall is set to avoid having embrittled material inside the core [11–13]. The alloys M5, ZIRLO and HiFi have been developed to improve corrosion performance and lower hydrogen pick-up, allowing for higher burnup [14]. Still, aqueous corrosion represents an important challenge for cladding materials, even during

normal operation. Any improvement on this front is welcomed and would allow for better fuel efficiency and longer fuel cycles.

2.3.2 Mechanical properties and creep

The cladding tube has to separate the cooling water from the fuel pellets, but it is also the main structural material for the fuel assembly. As a result, certain mechanical properties are required for the cladding to sustain the weight of the fuel and to be geometrically stable while manufacturing and loading the fuel assembly. On top of these minimum requirements, the cladding has to present some ductility and good creep properties. During the fuel cycle, the cladding starts by shrinking down under reactor pressure until it gets in contact with the fuel pellets, and subsequently the cladding has to follow the increasing swelling of the pellet due to the growing burnup. Zirconium is a relatively ductile material and its alloys are well suited to meet these requirements. Any change in the cladding material needs to keep ductility and creep behaviour into consideration [6].

2.3.3 Debris fretting and hardness

Debris fretting is currently the main cause of cladding failure in commercial reactors [9]. This phenomenon occurs when debris transported by the cooling water remain stuck between the cladding tube and the spacer grids. Once stuck, the flow of cooling water constantly moves the debris against the cladding tube. When the debris is composed of materials with higher hardness than Zr and ZrO_2, this continuous movement result in abrasion of the oxide scale and eventually of the cladding itself. In the most severe cases, this process can produce cladding perforation, which then needs to be attended by stopping the reactor and changing the damaged fuel assembly. Any interruption of the production of electric power is very costly, and reducing the occurrence of such undesired events is very important. Grids filtering the cooling water that enters the reactor have been installed in most power plants but, ultimately, only the use of harder cladding materials can remove the risk of cladding perforation to happen. Zr is a relatively soft metal, and alloying and thermal treatments can increase hardness to a certain extent. Switching to ATF materials that come with higher hardness could solve the problem, and it is deemed one of the biggest secondary advantages that can be drawn from material renewal associated with ATFs.

2.3.4 Effects of irradiation on materials

The main effect of neutron irradiation on crystalline materials is the creation of point defects as vacancies and self-interstitial atoms. On the macroscopic scale, accumulation and motion of these defects can induce irradiation growth (volume conserved, no load), irradiation creep (volume conserved, little load) and irradiation swelling (volume increase induced by formation of microscopic voids or gas bubbles – not seen in Zr claddings) [15]. Different amount of irradiation damage will translate to distinct degrees of deformation, which means that the same type of component placed in regions of the core with different neutron fluences will experience different degrees of deformation. When a single component is exposed to a gradient of fluence, it will undergo different degrees of irradiation induced deformation from point to point, causing buckling and bending of the component itself. On top of this, materials can be affected in different ways depending on their properties. The hexagonal crystalline

structure of Zr, for example, reacts to irradiation in an anisotropic way – self-interstitial atoms will diffuse preferentially along the basal plane, while vacancies move more randomly. As a result, the direction of irradiation growth in Zr claddings depends mostly on the grain orientation and consequently on the texture of the cladding. Cubic crystals, on the other hand, tend to be more isotropic [15]. Irradiation can also enhance diffusive processes, it can dissolve secondary phase particles, and cause embrittlement. For example, pure chromium appears to undergo significant irradiation embrittlement [16] which could deteriorate the mechanical properties of any applied coating. All considered, the effects of irradiation on materials can produce unexpected behaviour and represent an additional challenge to the employment of any ATF coating design.

2.4 Accident tolerant fuels

2.4.1 An opportunity for new materials

The concept of ATFs has emerged in response to the Fukushima Daiichi accident in 2011. In this unfortunate accident, the inability to pump cooling water into some of the reactors in the plant triggered an increase in the core temperature beyond the design conditions. This type of accident is generally referred to as a loss of coolant accident (LOCA). Under these conditions the temperature in the core can rapidly rise to 700–900 °C. At these temperatures the oxidation rate of zirconium in contact with hot steam can drastically increase. As the reaction is exothermic, it can cause further temperature rise and it can trigger an autocatalytic exothermic oxidation reaction. This chemical reaction, expressed in Equation 2.1, results in the transformation of the cladding tubes into ZrO_2 and in the production of ignitable H_2 gas.

$$Zr(s) + 2H_2O(l,v) \leftrightarrow ZrO_2(s) + 2H_2(g) + Heat\ of\ reaction \qquad (2.1)$$

The oxidized claddings lose most of their integrity and mechanical strength, the fuel pellets and fission products are let into the water, the large amount of generated hydrogen builds up pressure in the core and any leak of this gas can result in large explosions. Considering that there are between 25 and 40 tons of zirconium in a LWR core and that this runaway reaction can take place in a relatively short amount of time (∼2h [17]), the severity of this accident scenario becomes immediately clear.

The accident at the Fukushima Daiichi power plants shook the nuclear industry. Nuclear electricity production had stagnated from the 1990s to the 2010s, especially in western countries, and this accident represented an additional obstacle to any further growth for this technology. In the years following the accident, many nuclear power plants were shut down, especially in Europe, and it was clear that the nuclear industry had to invest in innovation and safety if nuclear was to be considered again a viable technology for the decades to come. Parallel to this, governments and international energy agencies started to pay more attention to other fossil-free energy sources, with the green revolution acquiring momentum. Nuclear energy is not a renewable source of energy, but it has the advantage of having an extremely low carbon footprint and of being independent from weather conditions. These two features make nuclear energy a valuable technology to be coupled with wind, solar and hydro in the attempt to move away from fossil fuels. The possibility of nuclear energy being part of the solution to climate change and the unfortunate Fukushima accident created the perfect

conditions for a wave of technology renewal, driving a great amount of research focused on improving current designs and creating new ones.

Accident tolerant fuels aim at creating a better technology for nuclear energy production through the improvement of existing LWR based designs. The research on ATFs is divided into two main groups, improvements of the fuel pellets and improvements of the cladding tubes. When dealing with the cladding tubes, the main objectives are to avoid the repetition of a Fukushima-like accident by delaying (or by making impossible) the runaway oxidation of the Zr, and to improve the cladding performance under normal operation providing more flexibility and increased fuel lifetime. In order to achieve these objectives, both near-term and long-term solutions are being investigated. For the near term, the application of a thin, corrosion resistant coating on the outer surface of the currently used zirconium cladding is the mainstream of work. The solutions for the long-term aim at the integral substitution of the Zr cladding from the core, and the two main designs that are being considered are FeCrAl alloys and SiC/SiC composite materials. Since changing any parameter inside a LWR core would inevitably change the neutron economy and the reactor physics, it is important to consider the research on the fuel pellets and on the claddings as complementary. A schematic of the research organization around the concept of ATFs is presented in Figure 2-3 [6,18].

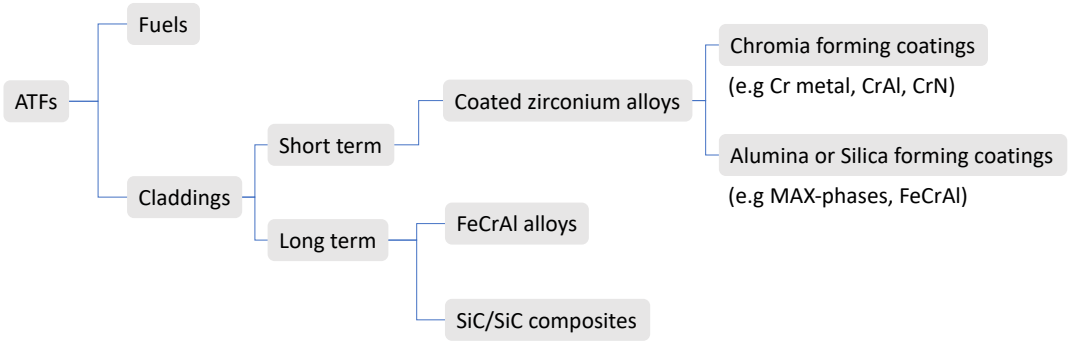

Figure 2-3: Organization of the global research on accident tolerant fuels.

2.4.2 COATED ZIRCONIUM CLADDINGS

The main reason why the application of a thin coating is compelling is that it would have little or no effect on the properties of a standard Zr-based cladding, and it would not influence excessively the core neutron economy. Thin coatings would not change the core physics too much and might even result in better overall performance while providing longer coping times in case of a severe accident. Beyond the improved safety under accident conditions, increased debris fretting resistance and better corrosion resistance are the main expected advantages that a coating could provide. Adding a step in the production process of the cladding tubes is expensive and it would result in a higher fuel cost. Improved debris fretting resistance would reduce the number of times the production of electricity in the plant needs to be stopped to perform rod maintenance, while better corrosion resistance could lead to higher burnup and fuel efficiency, partly compensating for the higher production cost of the fuel. The main drawback of this approach is that Zr is still kept inside the core. It is true that the outer diameter of the cladding would be protected from oxidation, but under LOCA conditions the rapid increase in temperature can simultaneously cause build-up of pressure in the tube and

deterioration of the mechanical properties of the cladding, often resulting in ballooning and bursting. Once a cladding has burst, the steam has a path to get to the inner surface causing Zr oxidation and making the coating partly ineffective. Nevertheless, the oxidation of the outer wall of an uncoated Zr cladding is one of the co-causes of cladding ballooning and bursting: since severe Zr oxidation causes strong impoverishment of its mechanical properties, the more oxidized the cladding becomes the weaker and more likely to burst it gets. In conclusion, the application of a thin coating would not be an infallible solution but it is generally deemed to be able to significantly delay the complete failure of a traditional Zr cladding under severe accident conditions. [19]

As shown in Figure 2-3, two main families of coatings are being investigated: chromia forming coatings, and alumina or silica forming coatings. Among the chromia forming coatings, metallic Cr has been studied profusely as ATF solution for PWRs. Metallic Cr is selected because it forms a passivating and dense scale of chromia when exposed to water corrosion. This oxide scale has low permeability to oxygen and it inhibits or slows down significantly the oxidation process. In simulated PWR environment, Cr-coatings on Zr-claddings have resulted in lower oxidation rates, reduced hydrogen pickup, enhanced resistance to debris fretting and improved mechanical properties of the cladding [20–26]. Under simulated accident conditions, Cr coated claddings have exhibited smaller ballooning sizes and significantly improved high temperature steam oxidation resistance [27–29]. The properties possessed by metallic Cr make it one of the best candidates as near-term ATF for PWRs. Cr coatings can be deposited with different deposition technologies, and the most important coatings currently under development are deposited with PVD or CS deposition. On the other hand, no definitive candidate coating has been identified yet for BWRs. Dissolution of chromia in water is possible and its rate depends on temperature and chemical environment. Overall, chromia growth and dissolution are the main factors determining if the coating is going to be consumed or if the system stabilizes once an initial protective scale has formed [30–32]. Chromia was found to dissolve in BWR simulated water chemistry, making the use of metallic Cr in this system impossible. Many ceramic PVD coatings have been tested in this work and, among them, (Cr,Nb)N coatings have been identified as a potential prospect thanks to its very good oxidation performance demonstrated in simulated BWR environments.

CHAPTER 3

COLD SPRAY DEPOSITION TECHNOLOGY

Cold spray is a process employed for coating deposition, additive manufacturing, and in-situ component restoration. This technique was initially developed in the mid-1980s at the Russian Academy of Science in Novosibirsk [33]. It is part of a wider group of thermal spray techniques and it is characterized by low particle temperatures and high particle velocities as displayed in Figure 3-1. Unless specified otherwise, references to this chapter are [34,35].

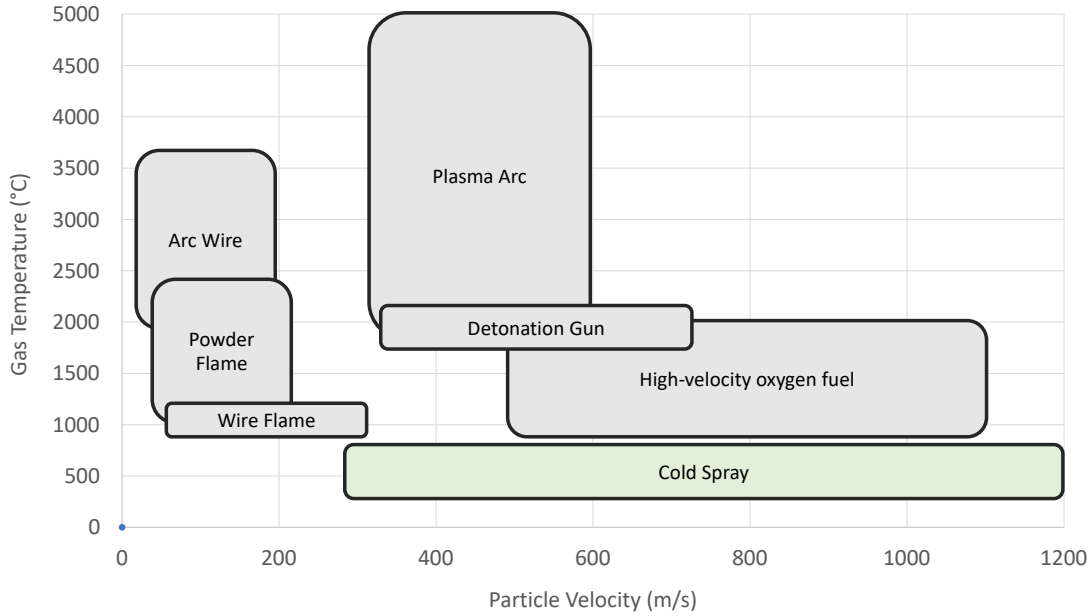

Figure 3-1: Comparison of particle speed and gas temperature in cold spray and other thermal spray processes (Reproduced from [35]*).*

3.1 WORKING PRINCIPLES OF COLD SPRAY DEPOSITION

In CS deposition, particles from a feedstock powder are the building blocks. The deposition process is based on accelerating the particles up to supersonic velocity and directing this jet onto the substrate. The coating is built particle by particle via ballistic collision between the particle and the substrate and/or other previously deposited particles. The particle size is usually ranging from a few micrometres up to 100 µm, the achieved particle velocity can reach 1500 m/s, but is more typically varying between 300 and 1200 m/s. Each powder-substrate system is characterized by a critical particle velocity, the minimum velocity at which particle adhesion and coating formation occurs. Below this velocity the particles are going to bounce off producing a shot peening effect, above this velocity the particles are going to consume the substrate with no deposition occurring, as for grit blasting. The critical velocity is mainly influenced by the hardness and ductility of the powder and the substrate. A schematic description of a CS deposition setup is displayed in Figure 3-2. High-pressure gas is supplied to

a gas heater where the gas temperature is increased to 100–800 °C. Then the gas stream is let through the nozzle where it expands and accelerates to form the supersonic gas jet. The same high pressure gas supply is used to create a separate gas stream that transports the feedstock powder to the main gas jet. The powder is typically fed to the main gas jet before the nozzle, but there are systems where the powder is injected in the nozzle, after the nozzle throat. The mix of hot, high-pressure gas and the powder accelerates through the nozzle, and the particles are sprayed onto the substrate at high velocities. Particle adhesion and coating formation is achieved by high velocity collision with the substrate. During the collision, particles and substrate are subjected to high rate, high strain plastic deformation that is at the origin of particle adhesion. Because of this, a certain ductility in the particles and the substrate is needed. This requirement on ductility makes the use of ceramic powder as feedstock material challenging. Composite ceramic coatings where one ductile material is coupled to a hard material are possible. However, metals remain the most commonly employed materials as feedstock powder for CS deposition. Thermoplastic polymers are also a feasible powder option for polymeric coatings [36]. The name *cold* spray technique comes from the fact that the temperature of the final powder/gas supersonic jet is usually below a few hundred degrees Celsius.

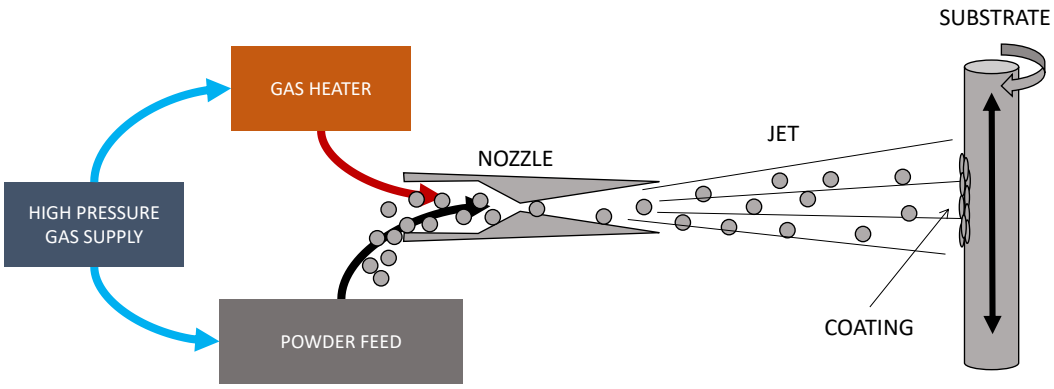

Figure 3-2: Schematic representation and basic working principle of a cold spray setup.

3.2 Advantages and disadvantages of cold spray deposition

As shown in Figure 3-1, the main differences between CS and other thermal spray techniques are the lower temperature of the gas jet and the higher particle velocity. The low temperatures involved in this deposition method, plus the use of an inert gas, lead to a strong advantage of CS: no significant phase transformation or oxidation processes occur on the particles or substrate during the deposition. Additionally, the thermal input on the substrate is minimal, making CS deposition suitable for temperature sensitive materials with little effect on the substrate microstructure. Each particle has a thin native oxide layer, as the particle impacts with the substrate the oxide shatters and detaches from the particle and gets flushed away by the gas jet [37,38]. Then, the exposed bare metallic surface of the particle bonds with the surrounding particles or substrate. As a secondary effect of this intimate interparticle contact, the electric conductivity of CS metallic coatings is typically extremely high. In addition, CS coatings retain the chemical purity of the base material and this can be advantageous in

preserving the good corrosion resistance of certain metals. The other fundamental characteristic of CS is the high particle velocities involved in the deposition process. High particle velocities together with the velocity distribution (which results in some particles moving below the critical particle velocity) produces a triple effect of grit blasting, spray coating and shot peening, where the substrate surface is prepared, loosely attached particles are removed and the coating is made denser. Summing up all effects, including the high degree of plastic deformation involved in the coating formation process, the result is a dense coating, with significant compressive residual stresses, a small grain size, high hardness, high strength, and with no grain growth induced in the substrate or in the coating. Anyhow, there are some disadvantages. As-sprayed coatings have almost no ductility left. Due to the nature of CS, the adhesion is strongly linked to plastic deformation. Some degree of plastic deformation of the substrate is expected in order to have good adhesion, and as a consequence, CS coatings on ceramic substrates have limited bonding strength. To achieve a high particle velocity, light molecular weight gases are used. Helium is commonly used but it is a limited resource and the application of this technique on a large scale using this gas is problematic. Moreover, it can be challenging to coat complex shapes or large areas because the spray beam is usually relatively small (10 mm in diameter) and must be kept at a short, fixed distance from the substrate for optimal coating formation [39].

3.3 Cold spray process parameters

The working principle and the schematic of the CS setup are quite simple. Nevertheless, to achieve particle adhesion and to obtain the desired coating properties, many different parameters need to be optimized. Particle velocity is the most important factor for the successful formation of a cold sprayed coating. The adhesion of the particles to the substrate involves high strain and high-rate plastic deformation in both particle and substrate. Below a certain particle velocity, the impact energy can be insufficient to produce such deformation and to achieve good adhesion. Powder size, shape, microstructure and material properties all have important consequences on the CS process. These properties can be controlled to a certain degree but are also strongly affected by the powder manufacturing process and by the material selected for the coating. Common powder manufacturing processes are gas atomisation and ball milling, and these methods provide spherical particles and flake-like powders, respectively. The particle size is particularly important for the achieved particle velocity, since smaller particles will be accelerated faster by the gas jet but will slow down earlier than bigger/heavier particles once they leave the nozzle. Hence, it is easier to achieve high particle velocities with finer particles, but the use of finer particles will require shorter spray distances [40]. The shape of the particles can also have an effect on the final particle velocity: irregularly shaped particles achieve higher velocities than spherical particles [41]. Particle microstructure can influence particle hardness and final properties of the obtained coating. Powders obtained by atomization are often characterised by very small sub-particle grains, and a fine grain size leads to higher hardness and reduced ductility. For this reason, annealing the feedstock powder before use in CS can be an effective way of increasing the ductility of the powder. Scanning electron microscopy (SEM) images of the feedstock powder used to deposit the CS-Cr coatings used in this study are presented in Figure 3-3.

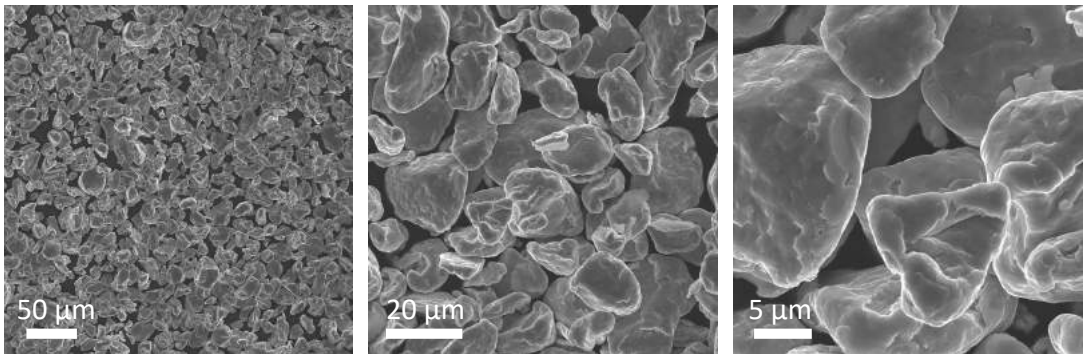

Figure 3-3: SEM images of pure Cr powder employed in the deposition of cold spray Cr-coatings.

Once all other parameters have been fixed and the characteristics of the jet of particles are determined, deposition strategies and parameters can affect the resulting CS coating. The nozzle traverse velocity influences the deposited coating thickness for each passage. The spray distance influences the velocity of impact of the particles: the particles are accelerated while in the gas jet but start decelerating when interacting with the ambient air resistance. For longer spray distances the deceleration in air increases in importance. The scanning step distance affects the overlap between different sprayed tracks and can result in different coating profiles. Finally, the substrate surface preparation can greatly influence the interaction between the sprayed particles and the substrate, affecting deposition efficiency and rate.

CHAPTER 4

PHYSICAL VAPOUR DEPOSITION

Physical vapour deposition (PVD) is an umbrella term that covers a relatively wide group of deposition techniques. In all PVD techniques, the surface of a target is evaporated, and the target atoms are sputtered onto a substrate to form a solid and dense coating. The coating is going to be made of the same material as the target, and the coating composition can be changed by changing the composition of the target. PVD is generally a vacuum technique, but small amounts of gasses can be let into the deposition chamber as process gas or in order to have the target atoms mix with the gas to produce coating chemistries that include the gas atoms (e.g. nitrides and oxides). PVD is distinguished from chemical vapour deposition (CVD) mainly by the deposition process mechanics and by the process temperature. In CVD a precursor gas (or gases) reacts onto the hot surface of the substrate, decomposes into a solid product and forms the desired coating. In PVD no chemical reaction occurs on the substrate, and the deposition occurs atom by atom or ion by ion. When sputtered onto the substrate surface, the atom/ion will find a local environment represented by atoms arranged into a solid surface and it will bind to the neighbouring atoms, condensing and promoting coating formation. Since no chemical reaction has to occur, the temperature of the substrate is theoretically not a critical parameter of the process. In practice though, temperatures ranging between 250 and 600 °C are generally used in order to optimize the deposition process and the coating quality. Lower process temperatures are advantageous when the properties of the substrate are important for the final application and elevated temperatures would modify them, for example in the case of steels or other metallic materials where the microstructure can be changed by heat treatment. Another advantage of PVD is the high deposition rate. Because there is no chemical reaction limiting the coating growth rate, the main factor limiting coating development is the amount of target material that is possible to evaporate and direct onto the substrate without affecting the quality of the coating. PVD deposition is widely employed to produce high hardness coatings for drilling, turning, or cutting tools. The coating chemistry can include metallic alloys, nitrides, carbides, and oxides. The deposited coatings can be monolithic or layered. The thickness of PVD coatings is usually around a few microns, but thicknesses up to a few tens of microns can be achieved. Multi-layered coatings can be obtained with relative ease, by alternating between different targets made of different materials, and layer thickness can vary from 1–2 µm down to a few nanometres. One of the main drawbacks of PVD is that the evaporated atoms/ions generally fly on a straight path away from the target surface into the process chamber. In order to obtain deposition, the substrate surface has to be preferably situated inside the conical region in front of the evaporated target, normal to the flight direction of the atoms/ions. This means, for example, that a tube can be coated only on the outer wall and no coating can be obtained on the inner wall with PVD [42].

4.1 CATHODIC ARC EVAPORATION PVD

In cathodic arc evaporation PVD (arc-PVD), a low voltage, high current plasma discharge between the target (cathode) and the reactor chamber (anode) is the energy source for

evaporating the target. The high energy density of this discharge at the arc spot leads to the transition from a solid to a metal vapour plasma that evaporates from the target material, together with a significant amount of metal droplets. These metal droplets can condense on the surface of the substrate creating a rough surface that can reduce the coating performance. The target material needs to be conductive (due to the high current associated with the arc discharge) and can have neither too low nor too high melting temperature, as the droplets then become too many or the evaporation rate becomes too low. Even though these factors can limit its range of application, thanks to the high deposition rate and the high target ionization ratio, arc-PVD is the most widely used technology for the deposition of thin coatings for industrial use. A schematic of an arc-PVD system is displayed in Figure 4-1. [43–46]

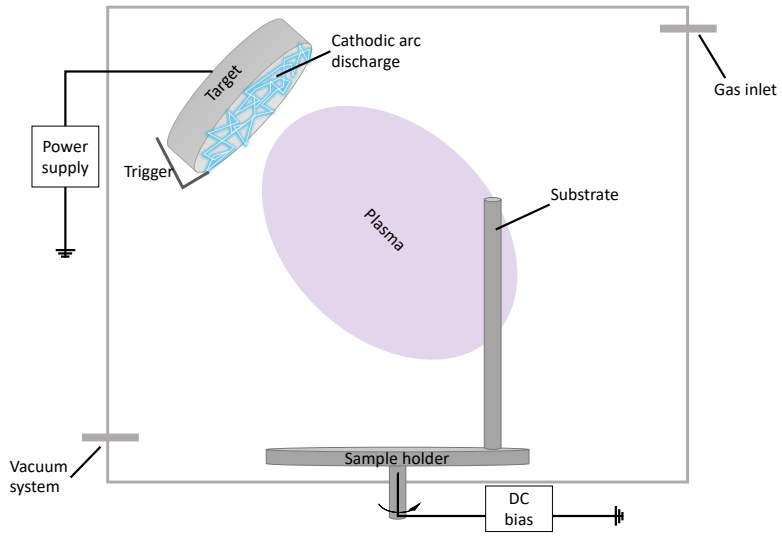

Figure 4-1: Schematic drawing of a cathodic arc evaporation PVD system

4.1.1 CATHODE CONFIGURATION AND MACROPARTICLE FILTERING

Metallic droplets are the main issue associated with arc-PVD and optimizing the configuration of the cathodes and of the arcs is one way of drastically reduce the amount of droplets. As shown in Figure 4-2 (a), the power supply for arc-PVD is a low-voltage DC power. If run continuously, droplets have the time to nucleate and grow. One way to reduce their size is to pulse the current instead of running it continuously. If the pulse duration is kept below the time required for a droplet to form, no large particles will be allowed to form. Pulsing the arc inevitably reduces the deposition rate but by increasing the peak current it is still possible to achieve industrially viable deposition rates [47]. An interesting consequence of pulsing the current is the generation of a significant magnetic field that is able to affect the arc plasma, moving around the spot where the arc hits the target material and further reducing the formation of droplets [44,48]. This phenomenon opened the door for the introduction of magnetic fields on the target, coupled with pulsed current, to move the arc plasma spot uniformly around the target surface. An example of this method is the “steered arc” [48,49]. Furthermore, playing with intensity and axial/transverse components of the magnetic field it is possible to transform the arc-plasma from a single large spot to a series of thin, linear arcs that move across the target distributing the current more uniformly and consuming the target material more homogeneously [50–53]. Targets currently used for commercial applications

come in many different shapes, ranging from a simple circular planar target to rectangular or cylindrical targets. The combination of the shape of the targets, the pulse frequency, current and voltage, and the intensity and direction of the applied magnetic field, provides a specific cathode configuration that every company tunes for its system in order to minimize the number of droplets while maintaining a high deposition rate. The optimal cathode configuration will drastically reduce the number of particles generated during the deposition, but it will never reduce their number to zero. One additional way to tackle their presence is by introducing a macroparticle filtering system [54], potentially achieving a perfectly smooth coating with no droplets. These filtering systems can consist of mechanical shields, the use of a pulsed bias, or magnetic filters. Mechanical shields work because the metallic plasma produced by the arc can move around physical obstacles and reach the substrate, while macroparticles will have a specific trajectory that, if intercepted by the shield, will stop the particle from reaching the substrate. This method is very easy to implement but it does reduce the deposition rate as well. The droplets formed during arc-PVD usually display a negative charge [55], and it is hence possible to apply a negative bias on the substrate that will repel the macroparticles while attracting the metallic plasma (metallic ions are generally positively charged). In this way, the amount of droplets that reaches the substrate can be reduced (but not eliminated) [56]. Finally, it is possible to separate the plasma from the particle with the implementation of a magnetic filter. A magnetic field is used to transport the plasma through a filter tube while the heavier particles are mostly unaffected [55]. Particle free, plasma deposition of coatings can be achieved, but during the time spent in the filter tube, some recombination of the ions and electrons occurs, and the deposition rate is drastically reduced [47].

4.2 Magnetron sputtering technology

In magnetron sputtering PVD (MS-PVD), the target material is evaporated by a glow discharge plasma. In a glow discharge plasma, electric current passing through a gas (usually Ar in MS-PVD) creates a cascade of electron collisions with gas ions that generates free moving electrons and positively charged gas ions. In MS-PVD, a magnetic field is used to force electrons to move along spiral trajectories. This has two main effects: prolonging the stability of the discharge plasma, and knocking electrons off gas atoms, ionizing the gas even further. The magnetic field does not affect the gas ions, as their mass is orders of magnitude higher than that of the electrons. A negative bias is applied to the evaporation target, and this bias attracts the gas ions which are accelerated toward the target surface. The accelerated gas ions collide with the target material and knock the target atoms off the target. Thus, sputtered atoms are created that can fly to the substrate surface and condense. A schematic of this process is presented in Figure 4-2 (a). No droplets are formed in this process since the coating deposition occurs only through low temperature sputtering and the target material is not restricted to a metal (or other electric conductor). However, the sputtered target atoms are mostly neutral (very low ionization ratio), which makes this technique mostly a line-of-sight deposition process, as neutral particles cannot be directed with electromagnetic fields.

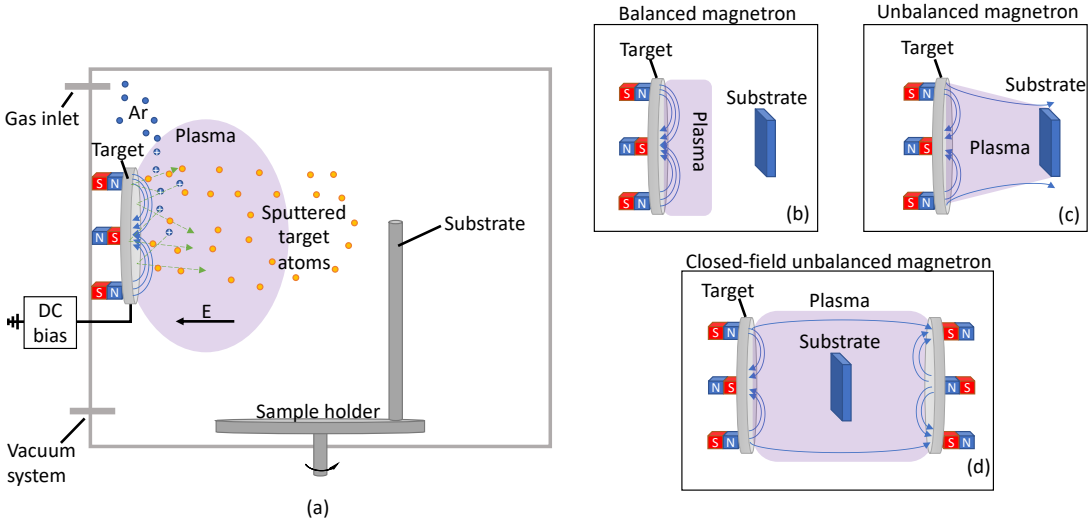

Figure 4-2: Schematic drawing of a magnetron sputtering PVD system (a). Schematic of the different possible magnetron configurations: balanced magnetron (b), unbalanced magnetron (c), closed-field unbalanced magnetron (d).

4.2.1 Target power supply, reactive gas and magnetron configuration

Magnetron sputtering techniques can be differentiated by the power supply used to sputter the target. The simplest power supply is direct current. Direct current MS-PVD produces nice and smooth coatings with deposition rates comparable to arc-PVD. As anticipated before, though, the plasma is going to be composed of gas ions and neutral metal atoms, which means that the plasma cannot be steered and the deposition of the sputtered metal atoms is going to happen only when the substrate is in line-of-sight with the target. Additionally, the coating becomes relatively loose with little control over the characteristic columnar microstructure. In order to achieve a higher ionisation ratio, which would allow to collimate the plasma, to attract ions in trenches or other high aspect ratio features of the substrate, and to control the ion bombardment energy onto the substrate, pulsed MS-PVD was introduced [57]. In pulsed MS-PVD, a rectangular or sinusoidal wave is used instead of a DC power supply. The duration, peak intensity, and frequency of the pulsed power supply can be controlled and optimized to achieve a high-energy plasma with a high ionisation ratio (up to 90 %) [58–61]. Once the high ionisation plasma is generated, applying a bias to the substrate can modify the energy of the sputtered ions, and this can be used to control the microstructure and morphology of the obtained coating [62–66]. To expand the range of coatings to ceramic materials and other dielectrics, a reaction gas can be included in the deposition chamber. In this way, the gas ions sputtered onto the target surface will not only be Ar ions but can include other elements as N or O that are going to react with the target surface and finally end up in the final coating as well. Another extremely important parameter in MS-PVD is the magnetron configuration. The main possible configurations are balanced magnetron, unbalanced magnetron and unbalanced closed-field magnetron, as shown in Figure 4-2 (b), (c) and (d) [58]. In a balanced magnetron, all the field lines from one of the target poles ends in the opposite pole. In an unbalanced magnetron, the poles in the periphery of the target are set to be more intense as compared with the poles in the inner part of the target and a few field lines manage to escape from the target and are directed toward the substrate. This system allows the plasma to travel to the substrate producing an ionic current density onto it. Unbalanced magnetrons allow for higher

deposition rates. The most commonly used magnetron configuration, though, is the closed field unbalanced magnetron (CFUBMS-PVD). In CFUBMS-PVD, multiple unbalanced magnetrons are put together and the field lines from each one close on the other magnetron. This makes it possible to increase the density of the plasma improving coating deposition rates and quality [67–69]. The possibility to use multiple targets in CFUBMS-PVD makes it possible to use multiple materials in the same deposition process, achieving alloyed coatings or alternating layers of different compositions [42,64].

4.3 Microstructure and morphology of PVD coatings

PVD coatings are generally characterized by columnar grains. These grains or domains nucleate at the substrate surface and grow along the deposition direction [63,65,70]. By changing the substrate bias and temperature, it is possible to affect the size of these columnar domains (from amorphous, to fibre-like, to large columnar grains), and to favour one crystalline direction over the other, producing textured coatings. Each coating system reacts differently to different combinations of these parameters, and it is difficult to extract a general rule. Still, higher bias voltages and higher substrate temperatures both promote coating density and produce coarser columnar grains. The densification of the coating is often attributed to the higher kinetic energy of the ions that embed into the growing coating. The substrate bias has also another important effect on the properties of the deposited coating: higher biases produce higher acceleration of the depositing ions and consequently a stronger bombardment of the forming coating. Bombarding the coating with ions during its formation causes a cascade of events that produces lattice defects and increases hardness. Higher biases can partially compensate for lower deposition temperatures while still granting a high coating density. Another crucial parameter in the deposition of PVD coatings is the choice of reactive gas. Clearly, depositing a pure metallic coating is different from depositing a nitride coating. Beyond that, controlling the partial pressure of the reactive gas, the final content of N or O in the coating can be tuned. Through this mean, one specific stoichiometry can be promoted above others, and it is possible to favour specific phases or crystalline structures. When depositing coatings using multiple targets, multi-layered coatings can be obtained by alternating the deposition from the different targets. This is usually achieved by rotating the substrate towards one target and then towards the second target. The rotation velocity determines the thickness of the layers, and nanolayered structures are possible and often show extremely high values of hardness [64]. A TEM image and an APT reconstruction of a nanolayered coating is displayed in Figure 4-3 (a) and (b), respectively.

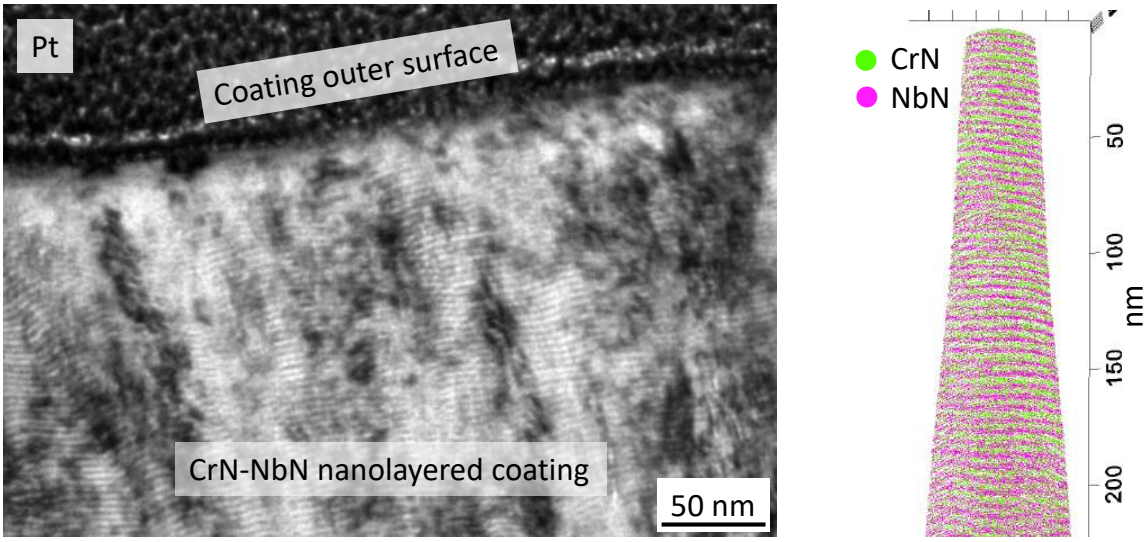

Figure 4-3: Nanostructured nitride coating deposited with closed field unbalanced magnetron PVD: BF-TEM image (a), APT 3D reconstruction (b).

CHAPTER 5

FUNDAMENTALS OF CORROSION

Corrosion refers to a series of deterioration processes that can occur when a material interacts with a certain environment. Corrosion affects all classes of materials but, generally speaking, metallic materials are the most susceptible to this phenomenon, and finding ways to protect metals from it has allowed the use of metallic components in ever more challenging environments. A metal in contact with the environment can react in three main ways: active corrosion, immunity to corrosion, and passivation. Active corrosion is a continuous process that progressively consumes or deteriorates the metallic component until the component becomes unfit for the application. If properly controlled and modelled, this process does not hinder the function of the component, as maintenance and substitution can be scheduled to avoid any failure. Noble metals, such as gold, are thermodynamically stable in a wide range of environments and are immune to corrosion. Passivation of a metal, instead, involves an initial interaction with the environment to form a layer of (hydr-)oxide, which, being less permeable to oxygen or other reagents present in the corroding environment, slows down or prevents further corrosion. Depending on the environment and on the temperature, different mechanisms are activated. Oxidation (through redox chemical reactions) and electrochemical interaction with the environment are the two main phenomena, and their effects can overlap but they tend to follow different dynamics and are usually handled in different ways. In an aqueous media (or other ionic liquids) at temperatures below the critical temperature of water, electrochemistry is the main tool used to describe corrosion processes. Oxidation can and does occur in aqueous corrosion, but it is usually expressed through electrochemical half reactions occurring at an anode and a cathode. Depending on the chemistry of the corrosive media, other electrochemical reactions can occur, and the presence of acids, bases and ionic species dissolved in the water can have significant effects on the overall corrosion process. Electrochemical corrosion can be used to describe the water corrosion undergone by cladding tubes in autoclave and under operating conditions. When higher temperatures are involved, for example during a LOCA scenario, corrosion is often described through redox chemical reactions where oxygen, water (if steam is present) and other chemical elements found in the oxidizing gas react with the metal forming more stable phases (e.g., oxides). Thermodynamics is the main theoretical framework used to describe these kinds of material-environment interactions. Unless otherwise specified, references to this chapter are [71–75].

5.1 ELECTROCHEMICAL CORROSION

5.1.1 BASICS

Electrochemical corrosion occurs in water or when surface moisture is allowed to form on the surface of the metal, and it describes the corrosion process through electrochemical thermodynamics. Corrosion generally occurs at the anode through the ionization and dissolution of the metal, while at the cathode, either the oxygen or the hydrogen reaction takes place.

These reactions can be described as follow:

$$Anode\colon\ M \rightarrow\ M^{2+} + 2e^{-} \tag{5.1}$$

$$Cathode\ (Option\ 1)\colon\ \frac{1}{2}O_2 + H_2O + 2e^{-} \rightarrow 2OH^{-} \tag{5.2}$$

$$Cathode\ (Option\ 2)\colon\ 2H^{+} + 2e^{-} \rightarrow\ H_2 \tag{5.3}$$

Where M stands for a generic metal.

Passivation, instead, involves the adsorption of oxygen or the formation of an oxide layer on the surface of the metal (anode):

$$Anode\ (Adsorption)\colon\ M +\ H_2O \rightarrow\ MO_{ad} + 2H^{+} + 2e^{-} \tag{5.4}$$

$$Anode\ (Oxidation)\colon\ M +\ H_2O \rightarrow\ MO_{ox} + 2H^{+} + 2e^{-} \tag{5.5}$$

$$Cathode\colon\ 2H^{+} + 2e^{-} \rightarrow\ H_2 \tag{5.6}$$

Passivation is the most desired situation, as a passivation layer stops the oxidation process and can self-heal if breached. The most commonly used oxide for passivation in water environment is chromia, but metallic chromium, being very brittle, is rarely used as structural material. The way chromia is obtained on the surface of steels or Ni-alloys is by adding Cr as an alloying element (at least 10 at.% is usually needed to form a passivation chromia layer on steels).

The electrochemical equilibrium of thermodynamically stable species can be affected by temperature, pH, electrochemical potential and concentration of dissolved species in the water. By calculating these equilibria in all conditions, it is possible to determine which species will be stable and hence be favoured under specific conditions. The results of these calculations are often displayed in Pourbaix diagrams (electrochemical potential vs pH diagrams). Pourbaix diagrams are plotted at a specific temperature and concentration of solute species in the water, and are valid only for the set conditions. Once obtained, these diagrams can be used to identify regions of immunity, corrosion or passivation. An example of a generic Pourbaix diagram is displayed in Figure 5-1. Here it is possible to see that immunity represents a region where the metal is thermodynamically stable in the solid state, corrosion is represented by a region where the metallic ion in water solution is stable, and passivation is represented by a region of stability of a solid oxide of the metal. It is important to mention that, in order to achieve passivation, the formed oxide needs to be dense and to stop or slow down water/oxygen ingress. A flaky oxide, for example, does not represent a barrier for the water, so the corrosive environment can still reach the metal surface and further oxidise the metal (no passivation). Other important lines usually present on these diagrams are the water lines (blue) indicating the range of stable water. Outside this range, water becomes unstable in favour of O_2 gas or H_2 gas, respectively, for the top and bottom blue line. A line along the neutral pH value for water at that specific temperature and pressure (red) is also often added.

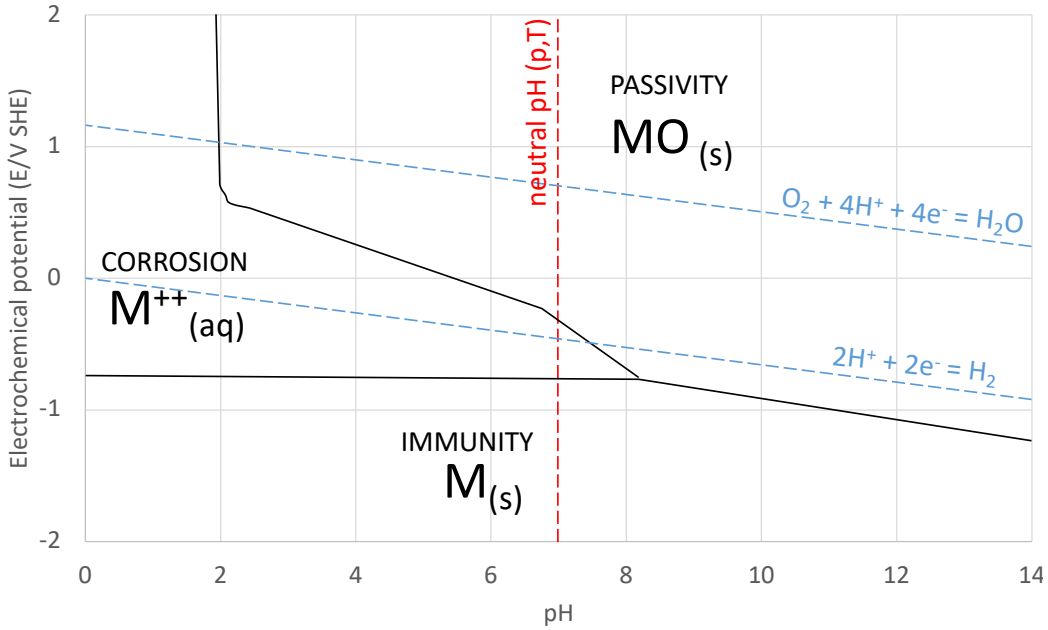

Figure 5-1: Example of Pourbaix diagram showing regions of corrosion, passivity and immunity.

5.1.2 CHROMIUM IN AQUEOUS ENVIRONMENT

Chromium is one of the most widely used alloying element for corrosion protection in aqueous environments. When oxidised, Cr can form Cr_2O_3, also known as chromia. This oxide is one of the solid reaction products of Cr oxidation, and it is a barrier to water and oxygen. This oxide generally grows through the diffusion of Cr-cations from the metal to the oxide surface where they react with O and promote oxide growth [76]. The diffusion of Cr-cations is very slow and the scale grows at a steady low rate, granting long-lived passivation of the metallic object – passivation in a system containing Cr is often strictly associated with the formation of stable Cr_2O_3. Pourbaix diagrams for Cr in water for a range of temperatures are shown in Figure 5-2. From these plots it is possible to see that temperature has an effect on the stability of the species. Chromia is stable in presence of pH neutral water, within the stability region of water at 25 °C and 100 °C, but no chromia can be found at 200 °C and 300 °C. At these higher temperatures chromia dissolves into the water in the form of water-soluble Cr-hydroxides. These diagrams can provide information about the stability of a phase, but no information can be drawn about the kinetics of dissolution, hence, the resulting corrosion rate could be extremely slow. The selected diagrams were chosen at a concentration of 10^{-8} mol/kg of dissolved species in water. Concentrations between 10^{-6} – 10^{-8} mol/kg well represent the purity of the water utilized in LWRs [76–78]. Higher concentrations of solute species can generally increase the stability range of the solid oxidation products.

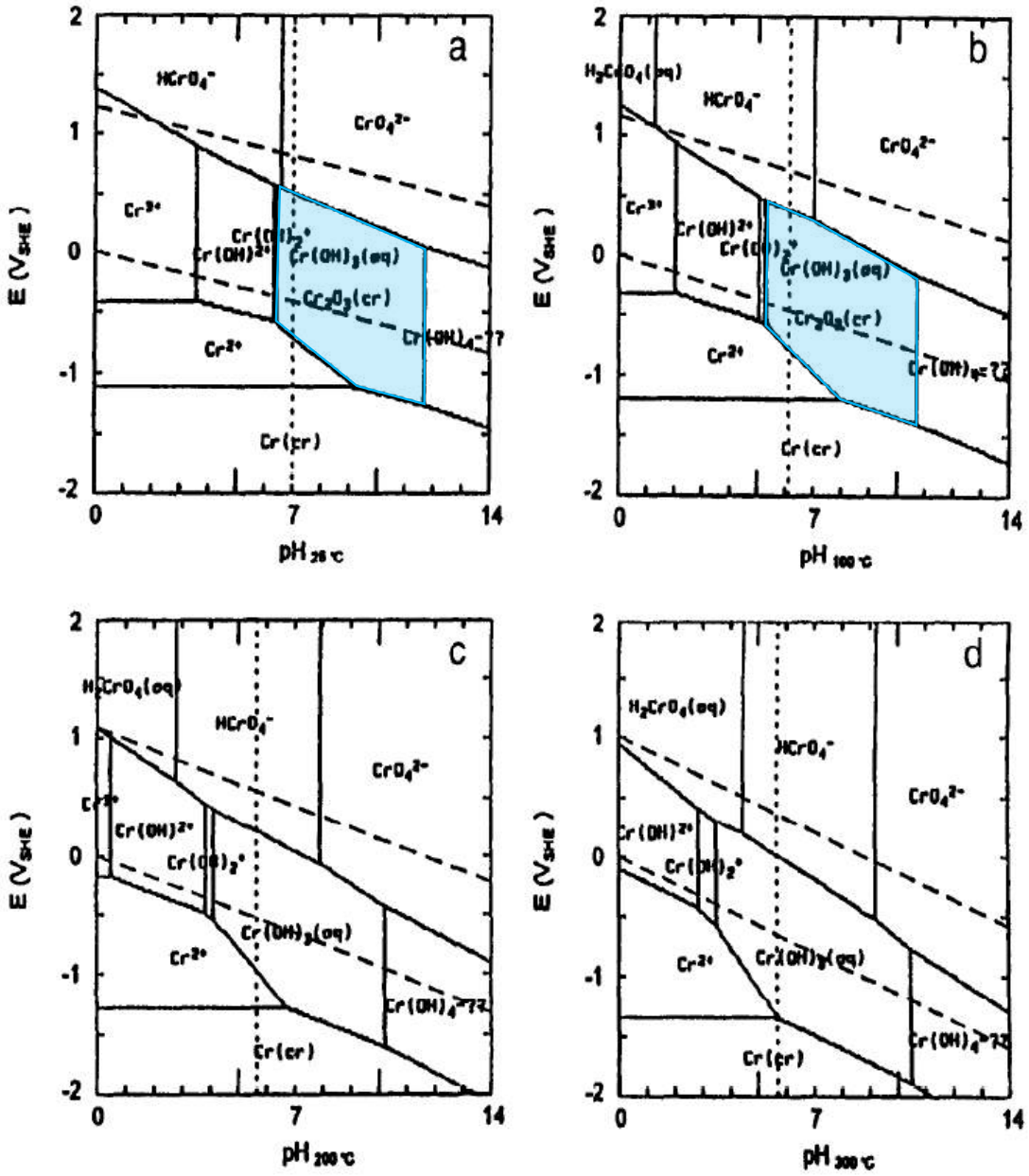

Figure 5-2: Pourbaix diagrams for chromium and $[Cr(aq)]_{tot}$= 10^{-8} mol/kg at 25°C, 100°C, 200°C and 300°C (Reproduced from [76] with permission from Elsevier). *Regions of chromia stability high-lighted in light blue.*

The effect of the concentration of dissolved Cr in the water is displayed in Figure 5-3. In these Pourbaix diagrams calculated at 300 °C and 10 MPa of pressure (close to LWR water temperature and pressure), chromia is stable for $[Cr(aq)]_{tot}$= 10^{-6} mol, but no range of stable chromia is found at $[Cr(aq)]_{tot}$= 10^{-8} mol. This means that the solubility of chromia in this system at this temperature and pressure is somewhere between the two values. One additional consideration that can be made, is that passivation films consist often of a layered structure. In the case of pure Cr, an outer layer of $Cr(OH)_3$ can form on the surface, reduce the oxygen potential underneath while creating a protected environment where Cr_2O_3 can develop and be stable as inner oxide [78–83]. All considered, drawing definite conclusions from Pourbaix

diagram without running corrosion experiments is somehow challenging and many factors can come into play, but these thermodynamic calculations can still be used to identify problematic regions of the pH, electrochemical potential, temperature, pressure, or solute concentration where it is unclear if Cr would help passivate the alloy or surface.

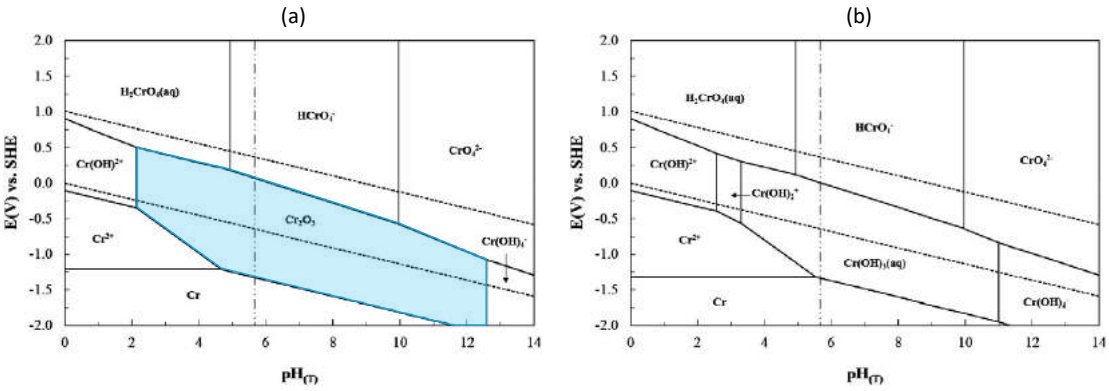

Figure 5-3: Pourbaix diagrams for chromium at 300 °C and 10 MPa pressure. (a) $[Cr(aq)]_{tot}$= 10^{-6} mol/kg; (b) $[Cr(aq)]_{tot}$= 10^{-8} mol (Reproduced from [77] with permission from Elsevier). Regions of chromia stability high-lighted in light blue.

From Figure 5-3, it is possible to identify some of the reactions that can cause dissolution of chromium or chromia. The most relevant equation for the dissolution of chromia is the following:

$$2Cr_2O_{3(s)} + 4H_2O_{(aq)} + 3O_{2(aq)} \rightarrow 4H_2CrO_4{}^-{}_{(aq)} \quad (5.7)$$

Metallic chromium has displayed very good corrosion resistance in PWR simulated operating conditions in autoclave [20,23,25,84,85]. This success is mostly attributed to the formation of chromia on the exposed surface. An example of this oxidation process can be seen in Figure 5-4. Pure metallic chromium in the form of coins (1 inch in diameter) were exposed to PWR operating environment in autoclave and a progressively thicker oxide layer can be found on the surface (this oxide layer was measured to be 100 – 150 nm thick after 90 days).

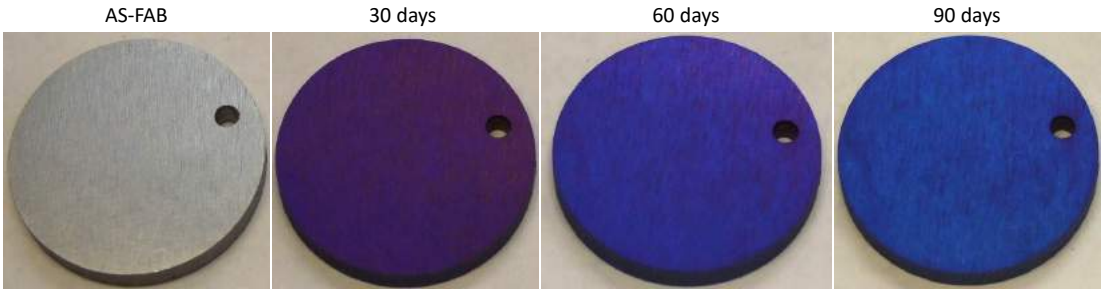

Figure 5-4: Coins made of pure metallic Cr exposed to PWR autoclave for 30, 60 and 90 days.

5.2 HIGH-TEMPERATURE CORROSION

High-temperature corrosion refers to a series of deterioration mechanisms that occur when the metallic object reacts with a hot gas. Water cannot be in liquid form and humidity is generally expressed as partial pressure of steam in the gas mixture. The environment most commonly studied is air (dry or humid), where the oxygen present in air is the main oxidating reagent. In high-temperature corrosion the oxidation process can be described as the oxidation of the metal at the oxide-metal interface, plus the reduction of oxygen at the oxide-gas interface. The two reactions can be described as follow:

$$\text{At metal} - \text{oxide interface} \qquad xM \rightarrow xM^{(2y/x)+} + 2ye^{-} \tag{5.8}$$

$$\text{At oxide} - \text{gas interface} \qquad \frac{y}{2}O_2 + 2ye^{-} \rightarrow yO^{2-} \tag{5.9}$$

$$\text{Overall metal oxidation reaction} \qquad xM + \frac{y}{2}O_2 \rightarrow M_xO_y \tag{5.10}$$

Where M stands for a generic metal.

Considering Eq. 5.10, it is possible to calculate the change in Gibbs free energy (ΔG) associated with this reaction as shown below:

$$\Delta G = RTln(p_{O_2}) \tag{5.11}$$

R is the gas constant, T is temperature in K, and p_{O2} is the partial pressure of oxygen.

Which can be rewritten as:

$$ln(p_{O_2}) = \frac{\Delta G}{RT} \tag{5.12}$$

As can be seen rearranging Eq. 5.11 into Eq. 5.12, the relationship between temperature and Gibbs free energy for a given oxygen partial pressure is a straight line in a $\Delta G\ vs\ T$ plot. Plotting these formulae for multiple oxide-metal reactions, it is possible to obtain an Ellingham diagram (oxide reaction at the standard state and $p_{O_2} = 1\ atm$) as shown in Figure 5-5. Once the energies for each reaction are plotted, a scale indicating the partial pressure of oxygen is generally added outside the main plot. These values are used to easily read the oxygen partial pressure in equilibrium with a specific oxide. In order to obtain this information, one needs to draw a line from the origin of the ΔG axis (point O) to the intersection of the oxidation reaction line at the temperature of interest and then extend that line until the oxygen partial pressure scale is met. Using this method (green lines), the equilibrium oxygen partial pressure for Cr at 1200 °C is measured to be around 10^{-17} atm. For higher O concentrations Cr will oxidise. The axis labelled H_2/H_2O and CO/CO_2 can be used in the same way to obtain the equilibrium ratio of H_2 and H_2O (or CO and CO_2) in a gas mixture containing those species. In this case, point H and point C are going to be used as origin of the lines.

When dealing with high-temperature corrosion, melting point and partial pressure of the oxide are also important factors. During oxidation at these temperatures, the transport of vacancies through the oxide scale is often the limiting factor for the oxidation kinetics. For this reason,

thicker scales will slow down the oxidation. If the oxide starts evaporating, the scale can be consumed, and oxidation can proceed faster. If the oxide melts, protectiveness will be lost. Another issue worth keeping in mind is the thermal stability of oxides. Cr_2O_3, for example, at temperatures higher than 1000 – 1200 °C starts forming CrO_3. CrO_3 is volatile, has a significantly higher partial pressure than Cr_2O_3, and can have an important role in the loss of protection from oxidation [86,87].

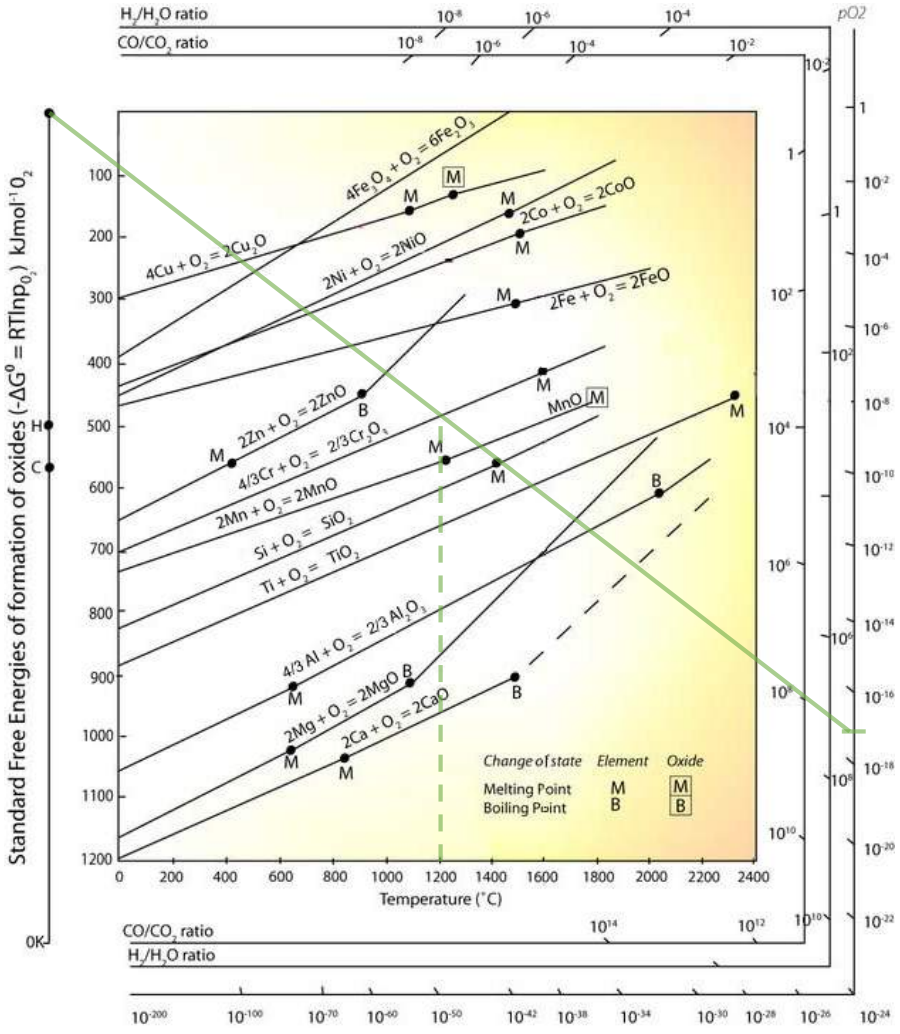

Figure 5-5: Example of Ellingham diagram (Image source DoITPoMS, Plotted data from [88]).

5.3 Corrosion protection

Material selection is often bound to specific minimum requirements. These parameters can be mechanical properties, manufacturing technology, electrical properties, thermal stability, neutron cross-section and corrosion resistance. When possible, an alloy is selected to meet all the requirements in a single material. For example, in stainless steels, Cr is added to the alloy in order to provide great corrosion resistance at the cost of slightly inferior mechanical properties. In certain applications, though, this compromise cannot be reached (or the development of new material is still ongoing) and the available material of choice does not

meet the corrosion resistance requirements. In these cases, there are alternative ways to protect the component from corrosion. As the dissolution of a metal into water due to electrochemical corrosion occurs through the ionization of the metallic atoms into positively charged ions, the application of a negative electric bias onto the metal surface can help preventing this dissolution. This can be achieved either by using an electric power supply or by coupling the component to a sacrificial anode. The sacrificial anode will be consumed over time and will need to be replaced periodically. In both cases, the effect of this electric bias will translate into lower effective electrochemical potentials (see Figure 5-1), which can stabilize the metal in the solid phase or favour the formation of one of the solid oxide phases. This method is referred to as cathodic protection. Another method is the employment of inhibitors: chemicals that can slow down certain reactions occurring at the cathode or anode, or that can capture oxygen reducing the effective O-potential. Finally, the application of coatings is another way of protecting a component from the environment. Coatings can include paint, ceramic or metal coatings that stop the oxygen from reaching the bare surface of the component or oxidise themselves to form passivating oxide layers.

As mentioned in Chapter 2, coated claddings are one proposed short-term solution to accident tolerance. An example of a Cr coated cladding after oxidation at high temperature is displayed in Figure 5-6. A homogeneous scale of chromia (green) appears to have formed after 5 min exposure at 1200 °C in air.

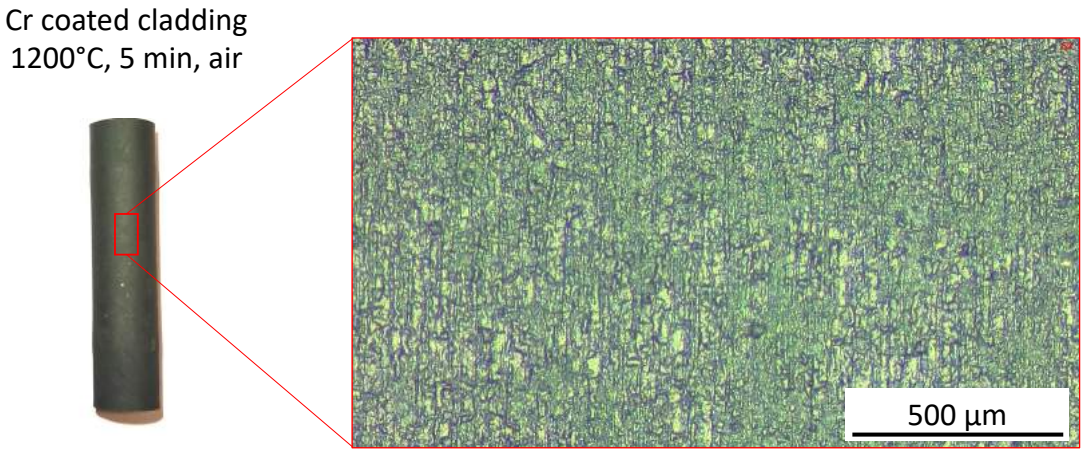

Figure 5-6: Cr coated Zr-cladding oxidised at 1200 °C for 5 min in air.

CHAPTER 6

PHYSICAL METALLURGY

6.1 THERMODYNAMICS AND DIFFUSIVE PHENOMENA

Thermodynamics makes it possible to calculate the stability of a phase or a mix of phases, and can be used to predict if a system is going to evolve towards a specific phase (or combination of phases) or if it is stable and no change is expected. At constant pressure and temperature, the energy of a system can be calculated through its *Gibbs free energy*: $G = H - TS$. Where H is the enthalpy, T is temperature, and S the entropy. Enthalpy can be calculated as: $H = E + PV$. E is the internal energy of the system, P is pressure, and V is volume. *Gibbs free energy* is not commonly used as an absolute value, but the difference in G ($\Delta G = G_A - G_B$) between two phases or between the initial and final state of a phase transformation is used to represent the driving force of such reaction or transformation. The phase with the lowest G at a specific temperature and composition is going to be the thermodynamically stable phase. If temperature and time allow for it, a system will always tend to reach the thermodynamic equilibrium and form the most stable phases. Unless specified otherwise, the reference for this section is [89].

The thermodynamic calculations can be performed across a range of temperatures and compositions and the stable phase or combination of phases can be plotted in a diagram. These plots are called phase diagrams and one example of a simple binary phase diagram for the Cr-Zr system is presented in Figure 6-1. This diagram is relevant to the case of Cr-coated Zr-claddings. Without any other information, it is possible to see that there is not much solubility of Cr and Zr in HCP-Zr (also referred to as α-Zr) and BCC-Cr, respectively, that an intermetallic phase (C15-Laves) with Cr_2Zr stoichiometry exists, and that any mixture of Cr and Zr will most likely tend to evolve towards an equilibrium between HCP-Zr and C15-Laves or BCC-Cr and C15-Laves. In a coated system, Zr and Cr are not mixed, but high temperature can promote diffusion, intermixing and the formation of a region characterized by a Cr-Zr mixture. Laves phases are generally brittle and the presence of a brittle layer at the coating-substrate interface could create some issues and affect the performance of the coating (i.e., spallation of the coating). Other relevant information that can be extracted from Figure 6-1, is that Zr has two different stable crystal structures, HCP at low temperature and BCC at high temperature. Zr is hence expected to undergo a phase transformation when the temperature of the system is changed through the transition temperature. BCC-Zr (or β-Zr) has a significantly higher solubility of Cr (up to around 5-6 at.% of Cr can dissolve in Zr without formation of new phases at a temperature of 1200 °C). Lowering the temperature from 1200 °C to below the transition temperature, will promote the formation of HCP-Zr and C15-Laves mixtures. Looking at even higher temperatures, the melting points of the system at different composition can be read. As often happens, the pure element has higher melting temperatures than the mixed system. The presence of a eutectic point found around 23 at.% Cr and ~1300 °C implies that liquid will form above this temperature for any mixture of Cr and Zr that falls between 0 and 66 at.% Cr. Because Cr-coatings are intended to work as accident tolerant fuels, and temperatures can in

the worst case reach above 1300 °C, it is important to keep in mind that the intermixing of Cr and Zr could lead to partial melting of the coating-substrate interface in case of a severe nuclear accident.

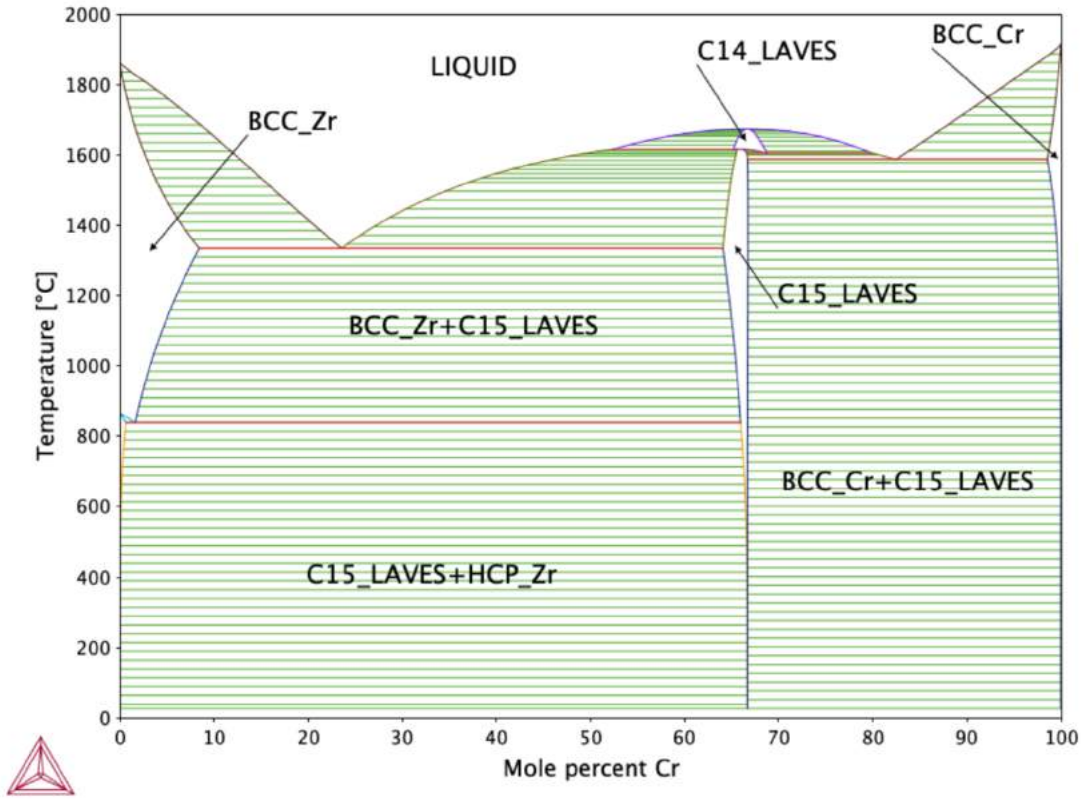

Figure 6-1: Zr-Cr binary phase diagram calculated using ThermoCalc.

A second family of ATF coatings studied in this work are PVD CrN coatings. A phase diagram for the Cr-N binary system is presented in Figure 6-2. This diagram shows that two different stable phases exist with stoichiometry Cr_2N and CrN, respectively. The two phases have different crystal structure, HCP and FCC. CrN coatings deposited with PVD can have a wide range of average chemical compositions, but as these two phases are the most stable ones, the deposited coating is expected to be composed of a mixture of Cr_2N and CrN. When adding additional elements to the system, for example Nb, the phase diagram becomes more complicated. One example of a ternary phase diagram calculated for the Cr-Nb-N system is plotted in Figure 6-3. Because this phase diagram has to include three elements, it becomes challenging to visualize it on paper, for this reason a cross-section at a specific temperature is often plotted instead, and Figure 6-3 is a cross-section at 400 °C. In this phase diagram there are various possible phases close to the 50 at.% N line: FCC-(Cr,Nb)N, HCP-Cr_2N, and Zeta-phase CrNbN. In particular, at the composition of 50 at.% N, 33.3 at.% Cr, and 16.6 at.% Nb, FCC-(Cr,Nb)N should be the only stable phase. The PVD process is usually performed at relatively low temperatures, and it is difficult to tell if the thermodynamic equilibrium will be reached. Metastable phases, or large amount of crystal defects can be present, and it is possible to have phases existing outside of their thermodynamic stability range. High

temperatures and irradiation can induce phase transformations, or nucleation of precipitate phases, changing the properties of the coating.

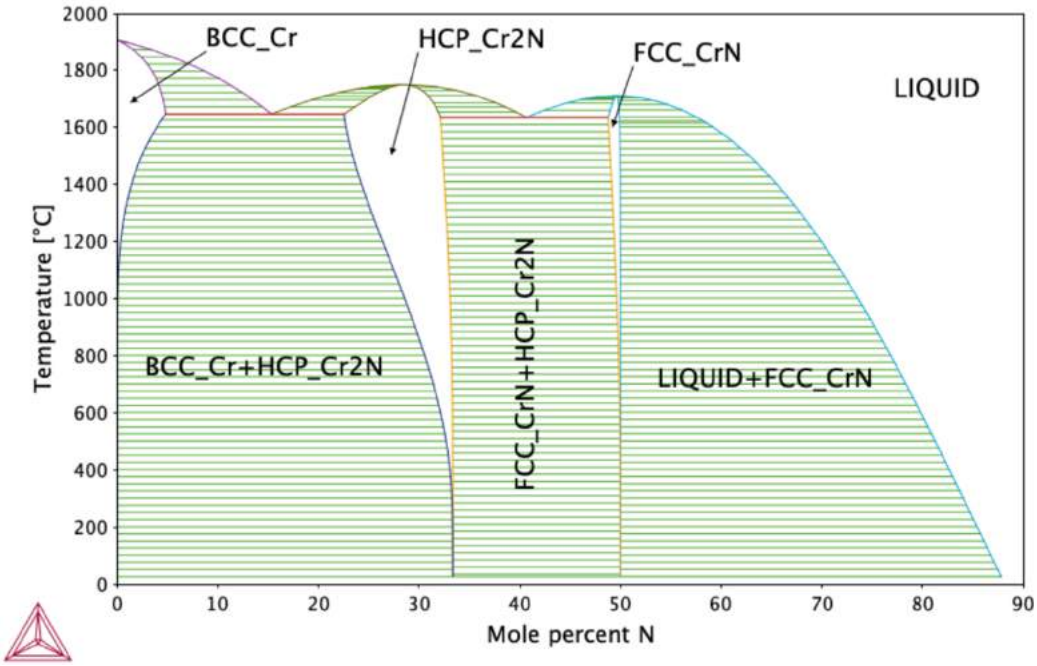

Figure 6-2: Cr-N binary phase diagram calculated using ThermoCalc.

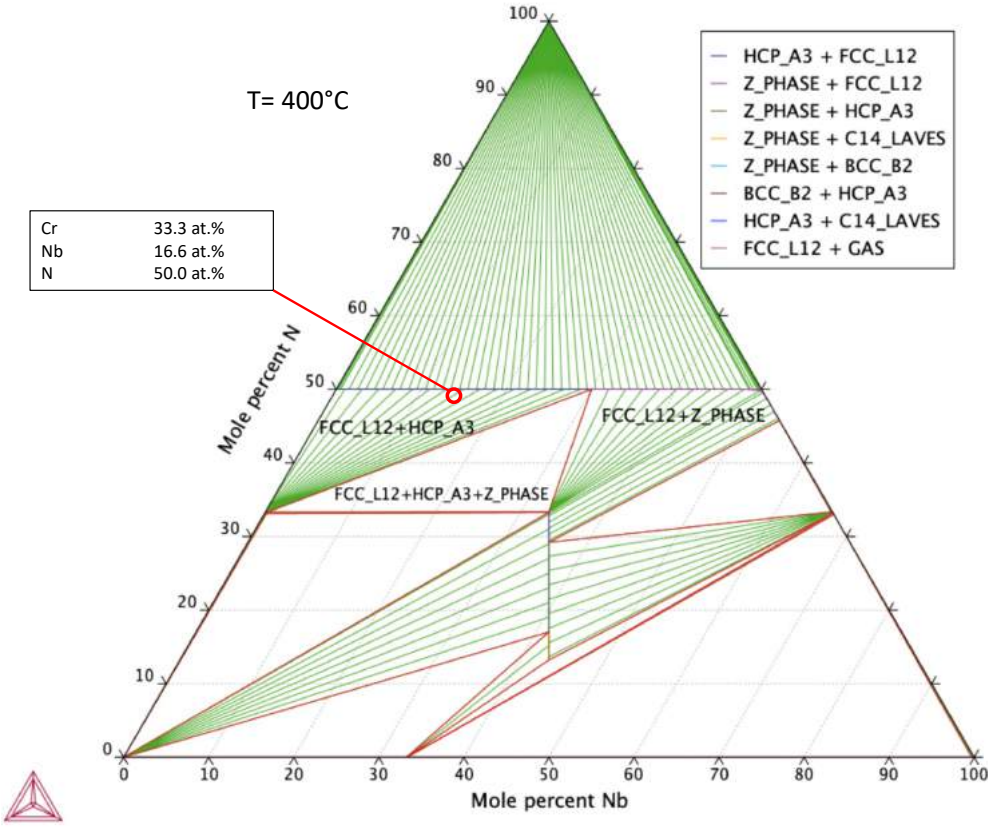

Figure 6-3:Cr-Nb-N ternary phase diagram calculated using ThermoCalc.

6.1.1 DIFFUSION COUPLES, PHASE NUCLEATION AND KIRKENDALL EFFECT

Thermodynamics provide information about stable arrangements at equilibrium, but to enable a transformation from a phase with higher G to a phase with low G, atoms have to move. Movement of atoms for phase transformation can be as short-range as a rearrangement inside the unit cell, or it can require long range diffusion from a region with a certain composition to another region with different composition. For this reason, phase transformations are divided between diffusionless transformations (rearrangement of atoms), and diffusional transformations (with atom migration). Most of the phase transformations occurring in the materials studied in this work are diffusional transformations. Diffusion is a transport phenomenon that is used to describe the movement of atoms in a crystal lattice. Atoms can either diffuse as substitutional atoms (moving from one atomic position to another), or as interstitial atoms (moving in the space between atomic positions). Interstitial diffusion is typical of atoms that are much smaller than the atoms making up the crystal lattice, and it is very fast when compared to substitutional diffusion. Substitutional diffusion is slower as it requires an atom occupying a position in the lattice to swap with another atom occupying a position in the lattice. The presence of vacancies in the crystal can assist this type of diffusion, as exchanging position with another atom in the lattice requires much more energy for an atom than it is for the same atom to simply move into an empty position in the crystal lattice. This description of diffusion is attributed to volume diffusion, and implies a continuous lattice in all directions. Single crystals are not very common in materials science. Real materials are composed of crystal domains arranged with different orientation which are called grains. Where grains meet (at grain boundaries) the lattice is more loose and atoms have more space to diffuse. In addition, interphase interfaces and free surfaces can also be found in materials. Grain boundaries, phase boundaries, and surfaces are considered high diffusivity paths and can become the predominant transport mechanism at lower temperatures, where volume substitutional diffusion tends to have very low rates. Diffusion is modelled as a flux of atoms per unit of surface. Diffusion of Sn (alloying element) in a Zr crystal can, for example, be written as in the Fick's Law reported in Equation 6.1 below:

$$J_{Sn} = -D_{Sn}^{Zr} \frac{\partial C_{Sn}}{\partial x} \tag{6.1}$$

J_{Sn} is the flux of Sn per unit surface per unit of time, D_{Sn}^{Zr} is the diffusion coefficient of Sn in the Zr lattice, and $\frac{\partial C_{Sn}}{\partial x}$ is the concentration gradient along the x direction. Even if the diffusion process is stochastic at the atomic level, at the macroscopic scale, atoms will tend to diffuse from regions of high concentration to regions of low concentration. Once the concentration of Sn is uniform everywhere, the net flux of Sn atoms diffusing will become zero. Sn atoms will still move around randomly, but being equally distributed, the flux in the various directions will cancel out. In the very simplified case of a diffusion couple (two pure materials welded adjacent to each other), the gradient is the maximum at the interface where the two pure materials face each other. Figure 6-4 displays a Cr-Zr diffusion couple. Diffusion of Cr in Zr is much faster than the diffusion of Zr in Cr [90–92], this means that the flux of Cr atoms leaving the Cr side will be much higher than the flux of Zr atom entering the Cr. This unbalance can be represented by a net flux of vacancies into the Cr lattice. This injection of vacancies has two effects, the vacancies can coalesce into pores on the Cr side, and the Cr-Zr interface will slowly move toward the Cr (as Cr gets slowly consumed). These two effects were first discovered in the 40s and are now

referred to as Kirkendall porosity and Kirkendall effect, respectively [93]. In addition to these effects, Cr and Zr can also form Cr_2Zr Laves phase, a stable intermetallic that, as mentioned earlier, is expected to develop at the Cr-Zr interface when diffusion starts mixing the two elements together. The formation of most new phases requires the creation of a new phase interface, which comes at an energy cost associated with surface tension.

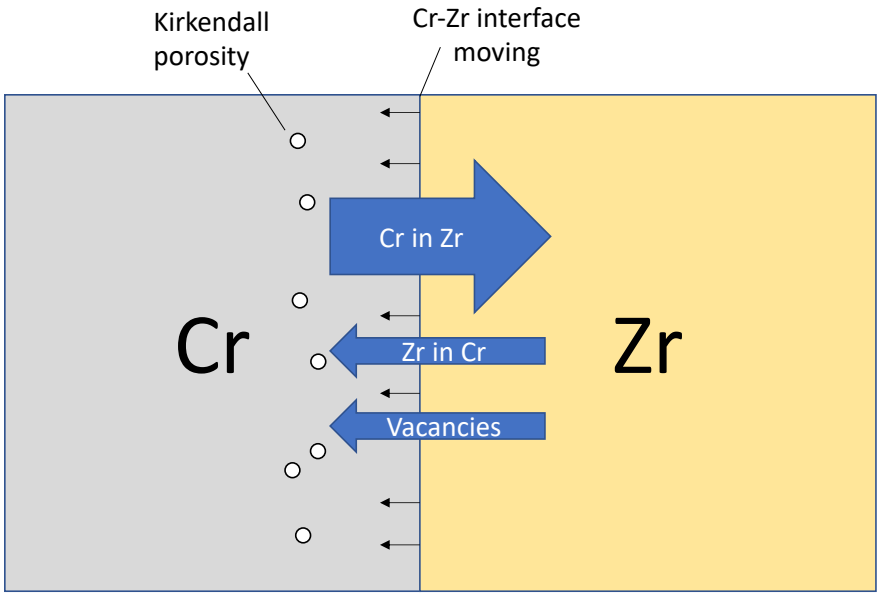

Figure 6-4:Schematic representation of Kirkendall porosity and Kirkendall effect for a Cr-Zr diffusion couple.

For this reason, before a phase can actually be stable and start growing, it has to go through an energy barrier linked to its nucleation. Nucleating a new phase inside a pre-existing crystal (homogeneous nucleation) requires a high energy, while nucleating at a defect, or interface (heterogeneous nucleation) can require less energy. In the case of a Cr-Zr diffusion couple, the Cr-Zr interface represents a great nucleation site, in particular grain boundary triple points where multiple Cr or Zr grains meet. Cr_2Zr is hence expected to nucleate at the interface in certain energetically advantageous places, and then grow along the Cr-Zr interface before starting to grow in thickness (see Figure 6-5). Once the Cr-Zr interface is fully coated with Cr_2Zr Laves phase, any diffusion flux from one material to the other will have to diffuse through the Laves phase as well, and the diffusion dynamics become more complex. The Cr side will see an interface with the Laves phase, the concentration gradients will hence be fixed at 33 at.% Zr and 66 at.% Cr, and the same will be for the Zr side. This will behave as two diffusion couples in series, with the important difference that if the flux of atoms leaving the Laves phase is higher, lower or equal to the flux of atoms entering the Laves, the intermetallic layer will respectively dissolve, grow, or stay constant while moving towards the Cr side as for the Kirkendall effect. Another complication is that diffusion in the Laves phase can be slower than in the other lattices, so in a sense this band of intermetallic can behave as a diffusion barrier and slow down diffusive intermixing in both directions. The system is overall relatively complex and various transformations are expected, in particular at elevated temperatures.

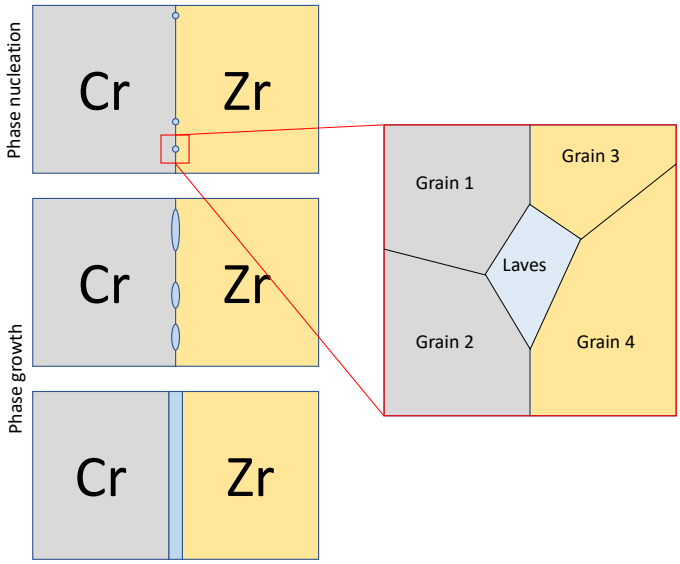

Figure 6-5: Nucleation and growth of the Cr_2Zr intermetallic Laves phase at the Cr-Zr interface.

Other factors worth keeping in mind are the interface characteristics. The presence or absence of a native oxide scale at the Cr-Zr interface can slow down the initial stages of interdiffusion, and the presence of defects, particles or intermixing of Cr-Zr can promote early nucleation of Laves phase.

6.1.2 Grain boundary migration, Ostwald ripening and thermal recrystallization

Free surfaces, interphase interfaces and grain boundaries are the main types of features important for the description of properties and behaviour of metallic materials. Depending on the system, different phenomena can affect the movement of such structures, but all of these interfaces have a surface tension, and this surface tension is often the principal cause governing their evolution. In the simple case of grain boundaries in a single-phase metal, the surface tension is the same for all grain boundaries. Imagining a triple point on a plane, where three boundaries meet, and assuming the triple point is somehow able to move, there will be no distinguishable difference among the three boundaries. The only possible equilibrium angles between each couple of boundaries is 120°. As each boundary pulls with the same strength, if the angles are different, the triple point will be pulled in the direction opposite to the largest angle until the stable arrangement of three 120° angles is reached. Assuming this is the stable configuration of a triple point, grains of different sizes and configurations will have different tendencies to grow, migrate or rearrange. An example of this is presented in Figure 6-6. As the angles at a triple point are somehow fixed, different arrangements of grains will produce boundaries with a curvature, curved boundaries will have a tendency to move in the direction of their concavity. This is a very simplified case, but it is helpful in understanding the dynamic nature of grain boundaries and consequently of grain microstructures. At the atomic level, the movement of a grain boundary implies short range diffusion (or rearrangement) of the atoms near the grain boundary. For this reason, the movement of a grain boundary is thermally activated and will reach the equilibrium configuration only if atomic movement is

allowed. At room temperature, the microstructure of most metals will be frozen in place and metastable configurations can exist.

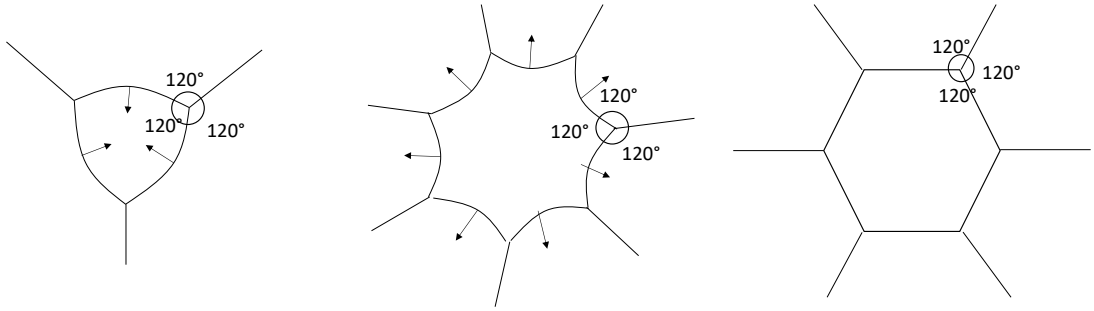

Figure 6-6: Schematic drawing representing different grain configurations and the consequent movement of grain boundaries (Reproduced from [89]).

One interesting phenomenon linked to surface tension is Ostwald ripening: large grains growing at the expense of smaller grains. Because the grain boundaries of small grains will have, on average, higher curvature than the grain boundaries of a larger grains, there is a tendency for small grains to become progressively smaller while larger grains grow. This phenomenon is used to explain and describe the formation of inhomogeneous grain size distributions and it is often seen in recrystallized materials.

This 2D model for grain boundary migration is based on capillary forces produced by surface tension and implies that the grain boundaries are free to move and are not constrained by their surroundings. In reality, surface tension is not the only driving force for grain growth (i.e. surface tension cannot explain stress driven movement of grain boundaries), and in a 3D polycrystalline material, grains and grain boundaries are constrained by surrounding grains. A better model for grain boundary kinetics is offered by disconnection-based models. Disconnections are line defects that exist at crystal interfaces characterized by a step hight combined with a dislocation (with its Burgers vector), which can be used as fundamental building block to model grain boundaries. Using disconnections it is possible to implement dislocation theory, crystallographic directions, and grain misorientation of each grain boundary to the description of grain boundary kinetics [94–97]. These models can explain the pinning effect of triple junctions (while still accounting for their potential movement), the emission and absorption of dislocation and other defects by grain boundaries, the effect of stresses onto the movement of grain boundaries, the formation of steps in the grain boundary, and many other phenomena. One limitation of this approach is the inability to model changes of grain boundary composition (i.e. when dealing with segregation of dopants at the grain boundary) or changes in the grain boundary structure at the atomic level. Molecular dynamics can be used to include these mechanisms but the large requirements of computing power limit its application to relatively small volume, or short simulated times [94].

Another important mechanism responsible for the rearrangement of grains and recrystallization is the relaxation of accumulated stresses or deformation in the material. Undeformed and stress-free grains have lower Gibbs free energy than deformed grains, hence it is possible to treat stress-free volumes as a thermodynamically stable phase that will nucleate and grow if allowed by temperature and time. In this sense, a highly work-hardened

material characterized by small grains and high dislocation density can transform into a relieved fully recrystallized microstructure if annealed for a certain amount of time.

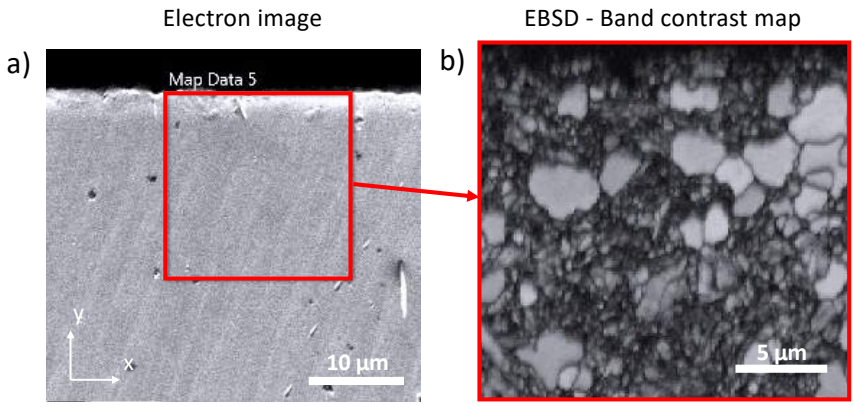

Figure 6-7: Cross-section SEM image (a), and EBSD band contrast map (b) of uncoated cladding. The cladding, made of Optimized ZIRLO alloy, is annealed to a partially recrystallized microstructure.

Optimized ZIRLO claddings are produced by extrusion and pilgering, and the high degree of plastic deformation induced by this manufacturing process is cyclically relieved by annealing steps that recrystallize the microstructure and allow for more plastic deformation to occur. At the end of the manufacturing, the cladding undergoes a heat treatment with the objective of obtaining a partially recrystallized microstructure characterized by the co-presence of larger grains in the 5 µm size range and smaller grains with a size of 1 µm or less. An example of such a microstructure is presented in Figure 6-7.

6.2 Deformation at low temperatures

Metals can undergo significant degrees of plastic strain when deformed under load. Once plastically deformed, metals are able to oppose stronger resistance to any further deformation. This ability is commonly associated with the concept of work-hardening.

Plastic deformation of metals is crucially correlated to dislocation movement. Deformation occurs when a number of crystalline planes shift in respect of the whole crystal to accommodate the macroscopic change in shape. In a theoretical defect-free crystal, this glide would have to be accomplished by moving an entire lattice plane in a single step, making this process requires extremely high energy. A certain density of dislocations, though, can always be found in metals as statistical defects and their presence allows the relative slide of different planes to be gradual and localized around the dislocation line, greatly reducing the energy barrier for deformation. For these reasons, dislocation movement, dislocation generation, and any mechanism that can influence either of these two phenomena, are at the basis for understanding plastic deformation and work-hardening in metals. The reference material for this section is [98–100].

6.2.1 Stages of strain hardening

As anticipated above, metals tend to increase their resistance to shear deformation along with the increase of strain undergone. This phenomenon of strain hardening is traditionally divided

into five stages and each stage is characterized by a predominant hardening mechanism. It is important to understand that not all stages realize themselves in every stress/strain curve and that this division in stages is more theoretical than practical (in most cases only one or two of these stages can be seen for a specific material). The description of these stages focuses on the dislocation aspect of deformation, nevertheless other mechanisms could be also active (localized shear, twinning and grain boundary sliding).

Stage I (Easy glide or laminar slip): Only a single slip system is active and the only strain hardening mechanism involved is inter-plane dislocation resistance that results in very little hardening. The stress/strain curve increases slowly and linearly. Stage I can be seen only in single crystals and cannot happen in a polycrystalline material where there will always be some grains oriented so that more than one slip system are active. This behaviour is typical of HCP single crystals where the only slip systems available are parallel to each other and cannot create intra-plane dislocation resistance. FCC metal single crystals can also present this behaviour when loaded along a crystal direction that creates high resolved shear stresses on a single slip system (no intra-plane dislocation resistance).

Stage II (Forest cutting and dislocation generation): Multiple slip systems are active, intra-plane dislocation resistance comes into play, many dislocations are generated and there is a rapid linear hardening. The differences compared with Stage I consist in the more intense resistance that dislocations moving on intersecting slip system face, in the large number of generated dislocations (dislocations as Franck-Read sources) and their subsequent accumulation around the slip obstacles. Altogether, this creates an increasing number of obstacles for dislocation movement. Polycrystalline high-melting-temperature FCC metals can show this specific behaviour when deformed at room temperature.

Stage III: Both inter-plane and intra-plane dislocation resistance are in play, multiple slip systems are active, many dislocations are generated and stored around slip obstacles, but the density of dislocations has reached a point where recombination and mutual annihilation of dislocations becomes consistent. Because a portion of the created dislocations are now annihilating each other, the stress/strain curve is now parabolic with a rapid decrease in work-hardening rate with increased strains. Additionally, being at higher loads, cross-slip is now active allowing screw dislocations to get free from obstacles by changing glide system/plane. Most metals exhibit only this behaviour followed by a short Stage IV, at this stage the differences between single crystals and polycrystals are very small.

Stage IV: The hardening rate is now low and constant (of the same order as for Stage I), during this phase the system is saturating with dislocations and their density grows very slowly. This stage is typical of very large strains and at the limit of maximum strain it can result in a flat stress/strain curve which corresponds to Stage V.

Stage V: The system is now saturated with dislocations, every additional dislocation created by the glide of moving dislocations balances out with another dislocation being adsorbed by a grain boundary or annihilated by an encounter with another dislocation. The material can accommodate some deformation but the hardening rate is zero.

A model stress-strain curve for each of these stages is reported in Figure 6-8.

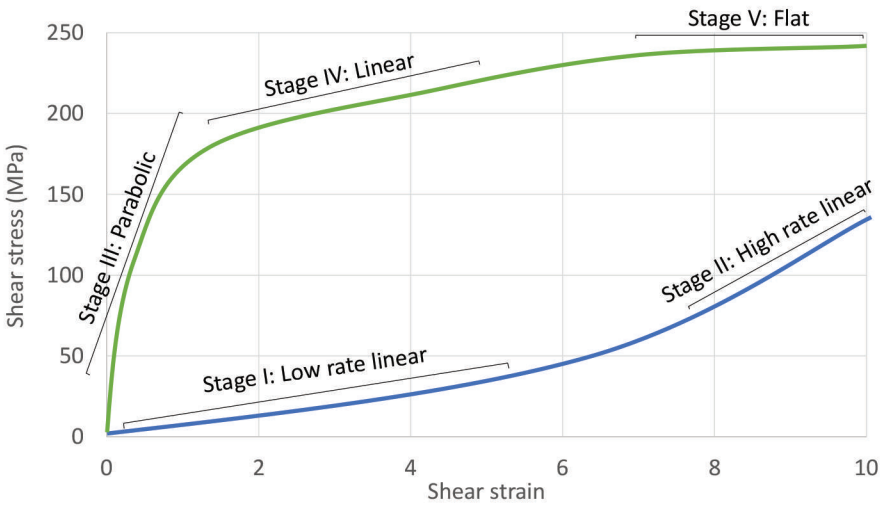

Figure 6-8: Schematic representation of model stress-strain curves associated with each stage of strain hardening.

6.2.2 MICROSTRUCTURE DEVELOPMENT

During plastic deformation, dislocations can rearrange in distinctive 2D or 3D structures able to influence the mechanical properties of the material. In order to get a 3D structure, intra-planar interactions and multiple active slip systems are fundamental. Dislocation climbing, dislocation cross slip and movement on intersecting glide planes are all necessary for the formation of these structures. Every specific alloy will develop a characteristic microstructure depending also on the way it is loaded. Nevertheless, materials can be generally divided between wavy glide materials able to produce 3D cell block structures and planar glide materials in which dislocations form 2D Taylor Lattice structures. The formation of these structures has to be associated with an overall decrease in the energy stored in the dislocations. This approach presumes the low energy dislocation structures hypothesis, which is used to explain why the dislocations should change their disposition and form the articulated structures mentioned before. In this model, uniformly distributed dislocations have an overall higher strain energy than a system where dislocation-rich walls separate regions of largely dislocation-free matrix. As a consequence, the system tends towards these structures in order to minimize the stored strain energy.

The cell block structures are the most common for polycrystalline materials and involve intra-planar dislocation interactions and multiple active slip systems. The dislocation boundaries emerge first as dislocation braids, then they grow by mutual trapping of gliding dislocations. The idea is that every single cell block has access to four or less active slips systems. Since five slip systems are necessary to get homologous deformation (Taylor model), each cell block will accumulate a certain degree of “rotation” or “tilt” along with the increased strain. This rotation and tilt can be either distributed uniformly in the matrix as single dislocations (high energy) or being accommodated by the formation of cell-block boundaries (low energy). In this way the overall ensemble of cell block structures will fulfil a homologous deformation even if every single cell block has less than the minimum amount of active slip systems required to do so. When a cell block boundary is accommodating rotation or tilt, it is called a geometrically necessary boundary. Other dislocation wall-like structures can form alongside the cell-block

boundaries but are mostly associated with the trapping of moving dislocations. The final result is a hierarchical organization with thick cell-block boundaries enclosing the cell blocks and thinner dislocation boundaries further subdividing each block. The cell-block boundaries are orientated in correlation with the strain and are accommodating the rotation/tilt necessary for the overall homologous deformation. The thinner dislocation boundaries form by incidental trapping of moving dislocations, and hence they are called incidental dislocation boundaries. This behaviour is typical of FCC and BCC metals (including iron and potentially chromium). For very high degrees of deformation, the cell boundaries can accumulate enough rotation/tilt to become low-angle grain boundaries and subsequently high-angle grain boundaries, resulting in continuous dynamic recrystallization.

6.2.3 Microstructure and adhesion of cold spray coatings

The basic principle for CS coating formation is the transformation of the particle kinetic energy into extensive plastic deformation upon collision with the substrate. The extreme plastic deformation disrupts the thin native oxide layer present on the particle surface and exposes new bare surfaces to the elevated contact pressure that results into an intimate contact between clean surfaces. Plastic deformation is central in achieving good coating consolidation during CS deposition [101].

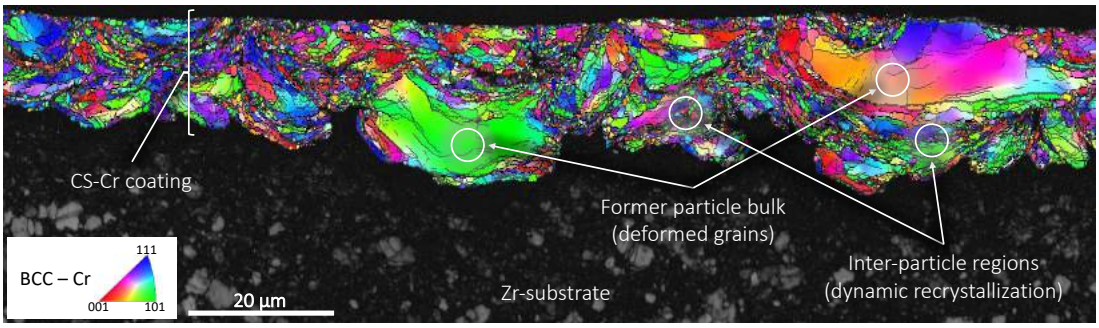

Figure 6-9: EBSD map of CS-Cr coated Zr-cladding (cross-section). Band contrast map is used for the Zr-substrate, IPF colours are plotted for the Cr coating.

The resulting microstructure of the coating is hence characterized by highly deformed grains and regions where dynamic recrystallization has taken place. Generally, the bulk of the former powder particles will be recognizable by the presence of larger, severely deformed grains elongated in the direction perpendicular to the coating growth direction, while the regions of particle-particle adhesion usually present smaller dynamically recrystallized grains. An example of such a microstructure is presented in Figure 6-9.

The main phenomena that are believed to affect adhesion in CS are plastic-flow localization and adiabatic shear instability. Plastic deformation always results in heat production, under normal conditions. The heat production rate is not high enough to generate a significant increase in temperature, so heat can dissipate, and the material deforms under isothermal conditions. In the case of CS, the duration of a particle collision event is usually shorter than a few hundred nanoseconds [102,103], and the heat generated by the plastic deformation has no time to dissipate. The temperature increases locally causing softening and annealing of the work-hardened material, resulting in a decrease of the stress needed to produce further plastic

deformation. As a consequence, if some regions end up being subjected to more plastic deformation than others, these regions will be softened more and will become more prone to accommodate further deformation, giving rise to plastic-flow localization. When plastic-flow localization occurs, shear and heat production become strongly localized in some regions while other parts of the material are subjected to little or no deformation. In CS deposition, the periphery of each particle is subjected to the highest degree of plastic deformation and heating. Here the temperature can rise significantly, and dynamic recrystallization is allowed to occur [104], while the bulk of the particle experiences little deformation [104,105], usually accommodated by the original grains of the sprayed particle. Figure 6-10a displays the different stress-strain curves for materials subjected to isothermal deformation, adiabatic deformation, and localized-adiabatic deformation. Additionally, a schematic of the different deformations resulting from adiabatic and localized-adiabatic conditions are shown in Figure 6-10 (b) and (c).

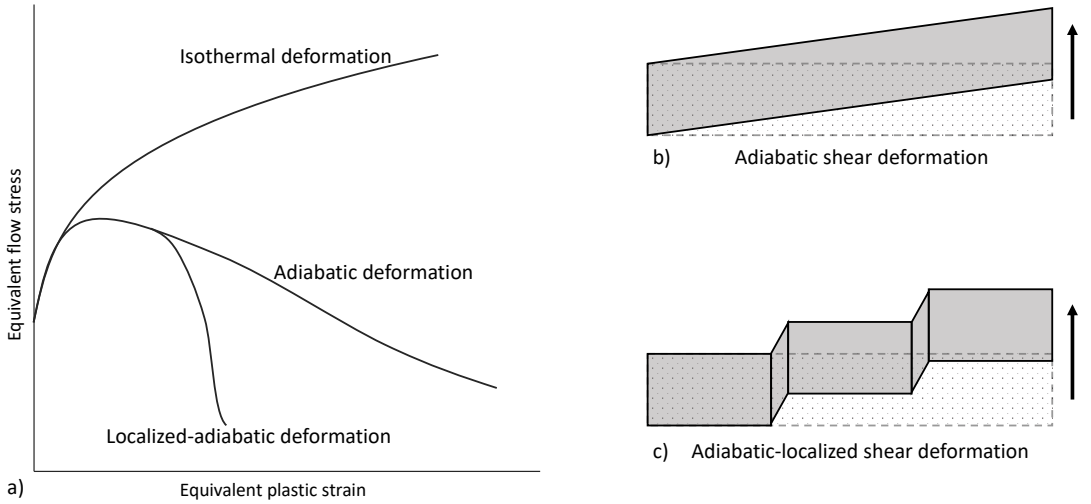

Figure 6-10: (a) Schematic stress-strain curves for isothermal, adiabatic and adiabatic-localized plastic deformation. (b) and (c) Comparison between adiabatic shear deformation and adiabatic-localized shear deformation, respectively. (Reproduced from [101]*).*

On top of the metallurgical bonding that forms when the bare metal surface of particle and substrate come into contact, two additional processes, one acting at the particle-size length-scale and the other at the nanometre length-scale, are commonly assumed to contribute to strong adhesion. At the particle-size length-scale, the substrate is commonly reported to significantly deform wrapping around the incoming particles, resulting in mechanical interlocking between particles and substrate (See Figure 6-11). In this topological arrangement, the particles are geometrically locked into place. At the nanometre scale, instead, the concept of interfacial instability is often used. Interfacial instabilities can arise when two fluids flow at different velocities parallel to their shared interface and can result in the formation of interfacial nano-scale roll-ups and vortices. Overall, these mechanisms seem to play a role in the adhesion of CS coatings and depending on the properties of the different coating/substrate systems, one mechanism can be predominant over the other.

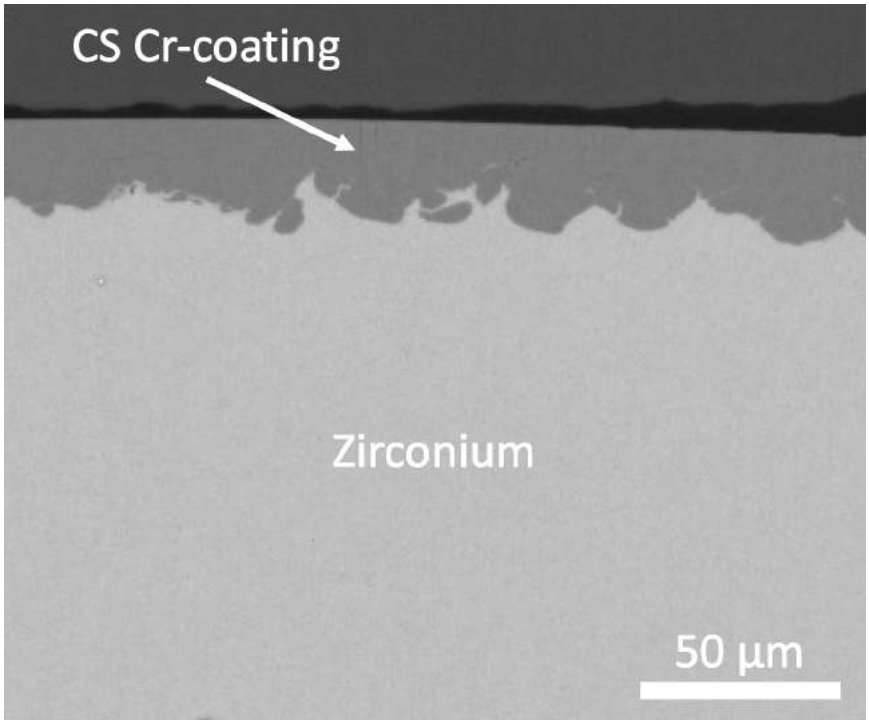

Figure 6-11: Cross-sectional SEM image of cold spray Cr-coating on a Zr-alloy substrate.

CHAPTER 7

EXPERIMENTAL PROCEDURES

7.1 MATERIALS

The focus of this work is on coated cladding tubes for accident tolerant fuels. A list of the analysed coated claddings can be found in Table 7-1. Two main groups of coatings can be identified: CS Cr coatings and PVD nitride coatings. CS Cr coatings were identified as a promising candidate for PWRs, and a first prototype of the coating 50 µm thick was employed to study the effects of CS on the microstructure of the substrate. A thinner version of the same coating was then selected for corrosion studies in autoclave and for simulated accident conditions. In parallel to the work conducted on the CS Cr, a range of PVD nitride coatings were subjected to preliminary autoclave corrosion tests in both PWR and BWR conditions. Among these, CrN and TiN were selected as model materials to show the different challenges offered by PWR and BWR water chemistries. On a second round of autoclave corrosion testing in BWR water chemistry, CrN/NbN superlattice (SL) coatings demonstrated exceptionally good performance. To follow up on this finding and investigate the role of the superlattice structure, a nanolayered (NL) CrN/NbN coating having the same average composition but thicker alternating layers was developed and tested in a third round of BWR autoclave corrosion testing. An image of a portion of as-fabricated CS-Cr coated cladding is presented in Figure 7-1.

Figure 7-1: Photo of as-fabricated Cr-coated Optimized ZIRLO™ cladding sample (200 mm in length, 9 mm in diameter, wall thickness 0.6 mm).

The CS Cr coatings were obtained by deposition of pure Cr feedstock powder sieved to a size smaller than 44 µm. The cladding tubes used as substrate for the coating were made of Optimized ZIRLO® (OPZ) alloy (nominal composition 0.8-1.2 wt.% Nb, 0.6-0.79 wt.% Sn, 0.09-0.13 wt.% Fe, 0.09-0.16 wt.% O, balance Zr). The achieved particle velocity during deposition was 1200 m/s (+/- 50 m/s). The PVD coatings were obtained by arc-PVD and MS-PVD onto HiFi® alloy cladding tubes (1.50 wt.% Sn, 0.40 wt.% Fe, 0.10 wt.% Cr, 0.08 wt.% Ni, and balance Zr). The PWR exposure was performed at Sandvik Materials Technology (now Alleima) in a static, closed loop, steam autoclave at 415 °C and 220 bar for a total of 90 days in PWR water chemistry. Pictures of the static autoclave setup are presented in Figure 7-2. The test temperature for static steam autoclave according to ASTM is 400 °C [27], but a temperature of 415 °C was chosen to exert more intense corrosion to the specimens. The first round of BWR autoclave exposure was performed at Studsvik in a once-through circuit, water autoclave at 360 °C and 220 bar for a total of 60 days in BWR water chemistry. The second and third rounds of BWR autoclave corrosion testing were performed by Toshiba Energy Systems & Solutions Corporation Japan in a once-through circuit, water autoclave at 300 °C and 100 bar for a total of 10 days and 60 days.

Table 7-1: List of analysed samples.

Coating	Details	Thickness*	Conditions	Exposure details	
Cr	CS, OPZ	50 µm	As-fabricated	-	*Paper I*
Cr	CS, OPZ	20 µm	As-fabricated	-	*Paper II, Paper III*
Cr	CS, OPZ	20 µm	Autoclave exposed (PWR)	220 bar, 415°C, 90 days, <45 ppb O	*Paper II, Paper III*
Cr	CS, OPZ	20 µm	Simulated LOCA	1200°C, 1 bar flowing steam, up to 40 min	*Paper III*
CrN	Arc-PVD, HiFi	5 µm	As-fabricated	-	*Paper IV*
CrN	Arc-PVD, HiFi	5 µm	Autoclave exposed (PWR)	220 bar, 415°C, 90 days, <45 ppb O	*Paper IV*
CrN	Arc-PVD, HiFi	5 µm	Autoclave exposed (BWR)	220 bar, 360°C, 60 days, 8 ppm O	*Paper IV*
TiN	Arc-PVD, HiFi	5 µm	As-fabricated	-	*Paper IV*
TiN	Arc-PVD, HiFi	5 µm	Autoclave exposed (PWR)	220 bar, 415°C, 90 days, <45 ppb O	*Paper IV*
TiN	Arc-PVD, HiFi	5 µm	Autoclave exposed (BWR)	220 bar, 360°C, 60 days, 8 ppm O	*Paper IV*
CrN/NbN SL	MS-PVD, HiFi	5 µm	As-fabricated	-	*Paper V*
CrN/NbN SL	MS-PVD, HiFi	5 µm	Autoclave exposed (BWR)	100 bar, 300°C, 10 and 60 days, 8 ppm O	*Paper V*
CrN/NbN NL	MS-PVD, HiFi	5 µm	As-fabricated	-	*Paper V*
CrN/NbN NL	MS-PVD, HiFi	5 µm	Autoclave exposed (BWR)	100 bar, 300°C, 10 and 60 days, 8 ppm O	*Paper V*

*Coating thickness refers to the as-fabricated coating, after exposure the thickness of the residual coating could be different.

Table 7-2: List of samples tested by Westinghouse in BWR autoclave

Coating composition	*Deposition technique*	Expected oxide	Survived BWR autoclave	Notes
Cr	CS	Cr_2O_3	x	Dissolution
Cr	arc-PVD	Cr_2O_3	x	Dissolution
CrN	arc-PVD	Cr_2O_3	x	Dissolution
CrN-Cr	arc-PVD	Cr_2O_3	x	Dissolution
Cr2N	arc-PVD	Cr_2O_3	x	Dissolution
CrWN	arc-PVD	Cr_2O_3	x	Dissolution
CrAlN	arc-PVD	Cr_2O_3/Al_2O_3	x	Dissolution
CrN/NbN SL	MS-PVD	Cr_2O_3*	v	Passivation
CrN/TiN SL	MS-PVD	Cr_2O_3/TiO_2	x	Spallation
TiN	arc-PVD	TiO_2	x	Spallation
TiAlN	arc-PVD	TiO_2/Al_2O_3	x	Spallation
TiN/CrN (2 layers)	arc-PVD	Cr_2O_3/TiO_2	x	Spallation
TiN/TiAlN (8 layers)	arc-PVD	TiO_2/Al_2O_3	x	Spallation

**Nb is also expected to contribute to the oxide composition*

Beside durations and temperatures, the main difference between the two water chemistries is that in the BWR autoclave exposure the oxygen content was monitored and kept constant at 8 ppm, while in PWR autoclave the oxygen content was kept below 45 ppb.

Figure 7-2: The PWR autoclave setup at Sandvik: the autoclave (left), the top without cover (centre), the inside (right).

Beyond the coatings listed in Table 7-1 which were the subject of detailed analysis and were the main object of the studies presented in the Appended Papers, a wide range of coatings was

tested by Westinghouse Sweden in PWR autoclave and BWR autoclave in association with this work. A summary of the screening correlated to BWR design is presented in Table 7-2. No data is presented for most of these samples, as most of the coatings listed failed to protect the Zr-substrate. It is nonetheless relevant to show that what is presented in this work results from a larger effort aimed at identifying possible candidate materials for ATF in BWR power plants. Additional information regarding the failure mode characteristic of the chromia-forming coatings will be presented in Chapter 8.

7.2 Characterization techniques

7.2.1 Choice of advanced materials analysis methods

The objective of this work is to identify, track, and understand chemical and microstructural changes occurring at the nano- and microscale. In the study of corrosion, for example, visual inspection and weight gain measurements can provide some insights on what is happening to the material, but it is very difficult to extract precise information about the corrosion mechanisms or failure dynamics. It might be evident that one coating works very well and another does not, but, to understand the reasons behind this, high resolution microscopy and chemical analysis are often required. Electron microscopy makes it possible to record high-resolution images, coupled with chemical and crystallographic information. All this information together is a powerful tool for phase identification, and it is crucial in studying corrosion. Knowing what oxide phase is growing on the oxidised surface can allow for better prediction of the oxidation dynamics and mechanisms. Grain structure, recrystallization, grain growth and plastic deformation in metallic materials can be studied through etching of polished cross-sections and hardness measurements, but these methods are somehow limited. Electron backscattered diffraction techniques make an entirely new world of crystallographic information readily available and visually accessible. Many properties of materials are modelled on physics- or chemistry-based theories that often invoke mechanisms occurring only at the atomic scale. It is possible to set up experiments that can verify such models and hypotheses, but sometimes a material does not behave as it is supposed to and finding the reasons behind these deviations is often difficult. It is well known, for example, that the segregation of certain alloying elements or impurities in precipitates, at grain boundaries or at phase interfaces can drastically change the mechanical, chemical, and electrical properties of materials. Atom probe tomography has been instrumental in this work to explain the adhesion properties of coatings and the nature of the chemical reactions occurring in autoclave, where the relatively low temperature does not allow for long range diffusion and the consequent formation of large features that could be accessible with other techniques.

7.2.2 Scanning electron microscopy

Scanning electron microscopy is one of the most widely used imaging techniques in science. SEM can be used on almost any material. It allows to obtain both topographic and chemical information from the samples and modern instruments have achieved nanometre resolution. It is flexible and can be used on bulk sample surface, cross-sections, particles, films, etc., with very little or no sample preparation. References for this section are [106,107].

The generic functioning of an SEM is schematically shown in Figure 7-3. In an SEM, electrons are extracted from an electron source by the use of strong electric fields (and heat in the case of thermionic guns). The two main types of electron guns are thermionic guns (not used in modern SEMs) and field emission guns (FEGs). The extracted electrons are accelerated towards the anode by an electric field, the achieved energy of the obtained electron beam ranges usually between 2 keV and 30 keV, although voltages as low as 0.1 kV can be used. Electromagnetic lenses are used to converge the beam into a fine probe, in this sense the SEM is a demagnifying instrument and the electron probe is the projection of the electron source reduced in size. The e-beam is then let through the condenser aperture which determines the convergence angle of the probe. Scanning coils are used to deflect the beam path allowing to scan the probe on the surface of the sample. When the electron probe hits the sample surface, different interaction phenomena between electrons and matter will take place and different types of signals will be emitted from the sample surface. The typical signals produced in the electron-matter interaction volumes are Auger electrons (AEs), secondary electrons (SEs), back scattered electrons (BSEs) and characteristic X-rays. The signals will be collected by different detectors and associated with the position of the e-beam. The e-beam will then be moved to the next region by the scanning coils and the process will be repeated. As displayed in Figure 7-3, each signal can originate from a pear-shaped region called the interaction volume. The primary factors determining size and shape of the interaction volume are the probe size and the beam energy. Larger probes will shower a wider portion of the sample surface, and the higher the energy of the electrons in the e-beam the deeper the electrons will be able to penetrate into the material. Additionally, different signals travel different distances through the sample before being reabsorbed, hence any signal produced at a distance from the surface longer than its mean free path will not be able to leave the sample and will not be detected, this determines the escape depth of each type of signal. All these effects are also influenced by material composition which can greatly affect the escape depth and the size of the interaction volume.

SEs, generated when the incident beam excites outer shell electrons of the specimen atoms, have energies below 50 eV and can be easily reabsorbed by the sample. They have a shallow escape depth, which makes this signal very localized around the area immediately underneath the electron probe (a few nanometres under the surface). SEs are usually detected by an Everhart-Thornley detector, and more recent instruments are also equipped with an InLens detector. This signal provides important topographic information, has a high spatial resolution and can be used to produce images based on morphological contrast. BSEs are electrons from the primary beam that have been scattered by the interaction with the atomic cores of the sample and have been deflected backwards. These electrons have significantly higher energies than SEs and have larger escape depth. For this reason, this signal has lower spatial resolution. BSEs are collected by a BSE detector and can provide elemental information in the form of Z-contrast (atomic number contrast). The local average atomic number is the main factor determining the likelihood of elastic scattering interaction that results in the emission of BSEs. Elements with higher Z will result in brighter BSE images. When the electron beam interacts with the sample atoms, an electron from an atom core shell can be ejected from the atom. When this happens, an electron from a higher energy level will quickly make the transition downwards to fill the vacancy. In most cases, this transition will be accompanied by an emitted photon (X-ray) whose energy matches the energy gap between the upper and lower level. In other cases, the energy released by the downward transition is given to one of the outer

electrons instead of to a photon. This electron (i.e, AE) is then ejected from the atom with an energy equal to the energy lost by the electron which made the downward transition minus the binding energy of the electron that is ejected from the atom. AEs have very low energy and can travel only a few atomic layers, they need ultra-high vacuum to travel undisturbed, and they cannot be collected in a standard SEM. X-rays can typically travel very far into materials, so they can reach the surface even when produced deep underneath the sample surface causing lower spatial resolution than any electron signal. These characteristic X-rays are collected by an energy dispersive spectroscopy (EDS) detector and they are used to extract qualitative and quantitative chemical and compositional information about the specimen.

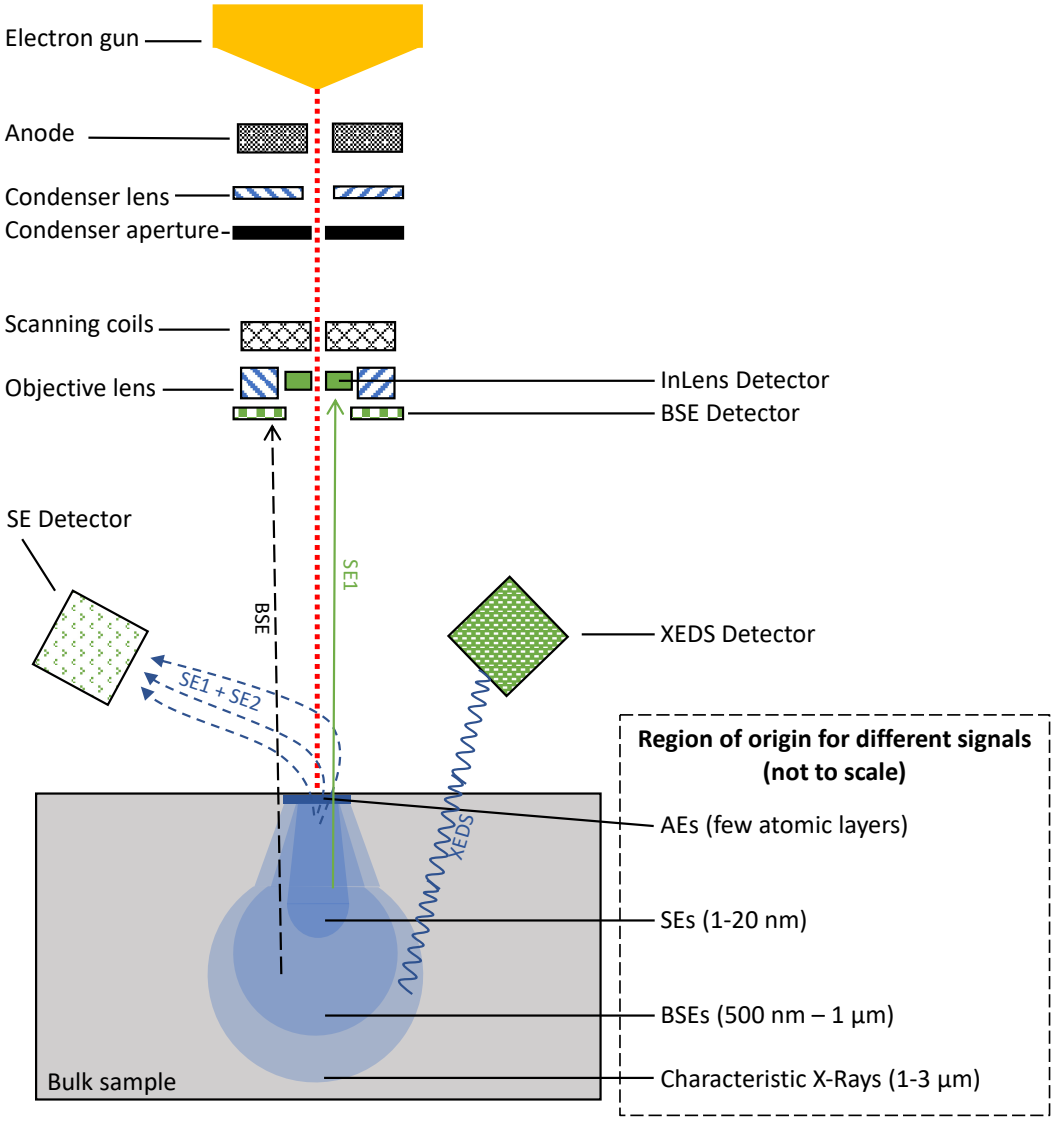

Figure 7-3: Schematic diagram of SEM. Instrument, e-beam/sample interactions and the origin of the different signals.

Experimental details:

In this work, SEM based techniques were used on all analysed samples to get an overview of the surface and cross-sections of coated claddings with the objective of identify potential features to investigate further with more advanced techniques. The microstructure and coating-substrate interface morphology could be preliminary appreciated with SEM imaging. This family of instruments was also widely employed to verify the overall quality and density of coatings, and the absence of porosities or cracks. EDS is a very powerful elemental analysis technique and it was instrumental in obtaining chemical information about the progression of oxidation early on. Micron-scale chemical segregation or phase formation can be easily captured with SEM-EDS and allows to build an idea of what phenomena that are occurring during coating deposition, autoclave exposure or under simulated accident conditions. A low-speed saw was used to cut the received cladding tubes into rings 5 mm in height. For cross-section imaging, the rings were embedded in conductive bakelite, ground and polished with SiC-paper and diamond particle suspensions. To image the outer surface of the claddings, the obtained ring was cut into two halves along the radial direction and glued onto a stub with silver paint so the outer surface faces upwards. For SEM imaging the selected accelerating voltage ranged generally between 5 kV and 15 kV. The accelerating voltage used to optimize the EDS signal was often ranging between 12 kV and 15 kV. Lower acceleration voltages would not excite properly K-lines from Cr, Fe or Ni. The main problem for EDS quantification is the overlap between Cr L-lines and O K-lines. It is possible to map O and see a qualitative distribution of it, but precise quantification of O in Cr rich phases would always come with an overestimation of the O content. In this work, an FEI Quanta 200 FEG Environmental SEM (ESEM) and a JEOL 7800F Prime SEM were used to capture images of the coated claddings and to perform EDS mapping of the same areas.

7.2.3 Electron backscattered diffraction and transmission Kikuchi diffraction

Electron backscattered diffraction (EBSD) and transmission Kikuchi diffraction (TKD) are both SEM based techniques where the scattered electrons emitted by the sample are used to investigate the type and orientation of the specimen crystal structure. These techniques provide a powerful way to read the microstructure of the material. The main limitation of EBSD and TKD is the sample preparation: in order to be able to collect the signal, the surface quality needs to be extremely high, which can be challenging to achieve for some materials. References for this section are [108].

When an electron beam interacts with matter, some of the electrons originated from the primary beam will be scattered. Scattering occurs through elastic and inelastic events and a single electron can be scattered many times. Under the flux of primary electrons, scattered electrons are constantly generated in the interaction volume and are emitted in all directions. To leave the sample, these electrons have to move through the crystal lattice, being originated from the entirety of the interaction volume and emitted in all directions, some of them will be travelling at an angle to a lattice plane that meets Bragg's law and will be scattered following this law. If the last scattering event of an electron before leaving the sample fulfils the Bragg condition, this scattering event will create a deficient region (where the electron should have gone otherwise) and an excess region (where the electron has been scattered towards) in the incoherently scattered electron distribution (originally uniform). When many of these events

are added together an excess line and a deficient line will appear in the incoherently scattered electron distribution; these lines are called Kikuchi lines and a pair of Kikuchi lines produces a Kikuchi band. Being produced by Bragg diffraction, the position of these bands is strictly associated with the orientation of the crystal lattice and influenced by the crystalline structure and the lattice plane distance. When this signal is collected from a bulk sample the technique is called EBSD, and when these patterns are obtained in transmission from a thin sample the technique is referred to as TKD. A schematic for EBSD and TKD setups is reported in Figure 7-4. In EBSD the sample is typically tilted to 70° to maximise the amount of signal hitting the detector. On the other hand, but for the same reason, in TKD the sample is usually tilted to -20°. The Kikuchi patterns from each scanned point are collected by an EBSD detector and automatically indexed by a computer system via comparison with a database. The crystallographic data can then be analysed and used to produce band contrast maps, orientation maps, pole figures and more advanced analysis of grain deformation, strain, etc.

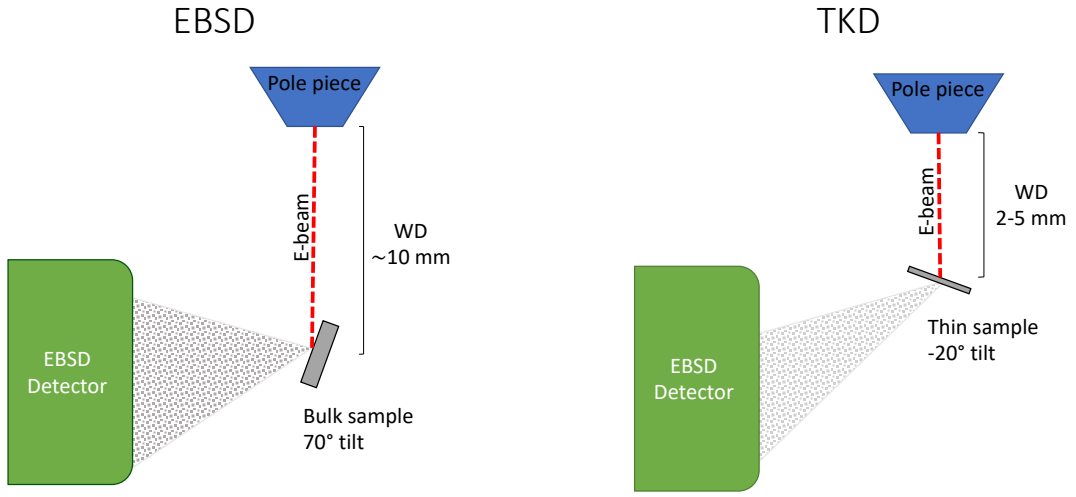

Figure 7-4: Schematic of EBSD sample/detector geometry (left). Schematic of TKD sample/detector geometry (right).

Experimental details:

EBSD and TKD were employed to study the grain structure of coatings and substrates before and after autoclave corrosion testing or exposure to LOCA conditions. To access this information, EBSD was performed on polished cross-sections and TKD was utilized on TEM lamellas. The EBSD polished cross-sections were obtained with a broad ion beam (BIB) milling system. A portion of a ring had to be cut and mounted with the axial direction perpendicular to the BIB beam, a silicon mask was applied on the cross-section to reduce curtaining and achieve the best surface quality. Once mounted, the samples were milled for 10 h at 6 kV beam acceleration voltage, and the obtained samples were then analysed directly with EBSD without further surface preparation. TKD lamellae were prepared with FIB/SEM, see Section 7.3. EBSD and TKD mapping were performed on a TESCAN GAIA3 equipped with an Oxford-NordlysNano detector. Post processing of the obtained data was conducted with AZtek 5.0 and HKL Channel 5 software from Oxford Instruments.

7.2.4 TRANSMISSION ELECTRON MICROSCOPY

Transmission electron microscopy is an extremely powerful microstructural characterization technique. TEM can be used to perform high spatial resolution imaging and to obtain crystallographic and chemical information from the sample. The technique works in transmission, which means the specimen needs to be electron transparent, typically a lamella between 20 nm and 200 nm in thickness. TEM can achieve atomic resolution, which makes this technique well suited for all advanced materials characterization needs. The main limitations of this technique lie in the need of a thin sample, which requires long and delicate sample preparation, and in the beam sensitivity of some materials, that makes it challenging to analyse certain samples without damaging them. In addition, there are some intrinsic limitations associated with the 2D representation of 3D objects. For example, any TEM based chemical measurement of small particles is prone to have contribution from the matrix. References for this section are [109,110].

Overview

A schematic of the instrument setup is presented in Figure 7-5. Different TEM instruments can have different setups but a TEM column can generally be divided into three sections: the illuminating system, the image forming system, and the projection and image recording system. In the illuminating system electrons are extracted from the electron gun and subsequently accelerated through the application of high voltage (typically 100–300 kV) between the gun and an anode to form the primary e-beam. A first strong condenser lens (C1) collects the emitted electrons from a large solid angle down to a demagnified image of the source. By controlling the strength of C1 and the C1 aperture it is possible to control the electron beam current. One or two additional condenser lenses (C2 and C3) follow C1. C2 projects the beam onto the specimen and controls the illumination area. The C2 aperture is used to tune the convergence angle of the beam. With only C2 and the C2 aperture it would not be possible to control the illumination area and the convergence angle independently, to solve this, modern instruments have a third set of condenser lens and condenser aperture (C3 and C3 aperture). The image system is made out of objective lenses and the objective aperture. The objective lens determines the final resolution of the instrument, and it is responsible for creating both the image of the sample (in the image plane) and the diffraction pattern (in the back focal plane). The specimen is usually inserted between a first and a second part of the objective lens. The selected area diffraction aperture (SAD aperture) is used to select a specific region of the sample from which to get electron diffraction. The projection lens magnifies the image or the diffraction pattern onto a fluorescent screen or a CCD camera, part of the projection and image recording system. If the instrument has the possibility to work in scanning transmission electron microscopy (STEM) mode, scanning coils will be placed between the illumination system and the image forming system. In this case, an annular dark field (ADF) detector and a high angle annular dark field (HAADF) detector will be present in the image recording system. For elemental analysis, an XEDS detector can be present in close proximity of the specimen and a set of filters, electron prisms and energy selecting slits can be used to perform electron energy loss spectroscopy (EELS) and energy filtered TEM (EFTEM).

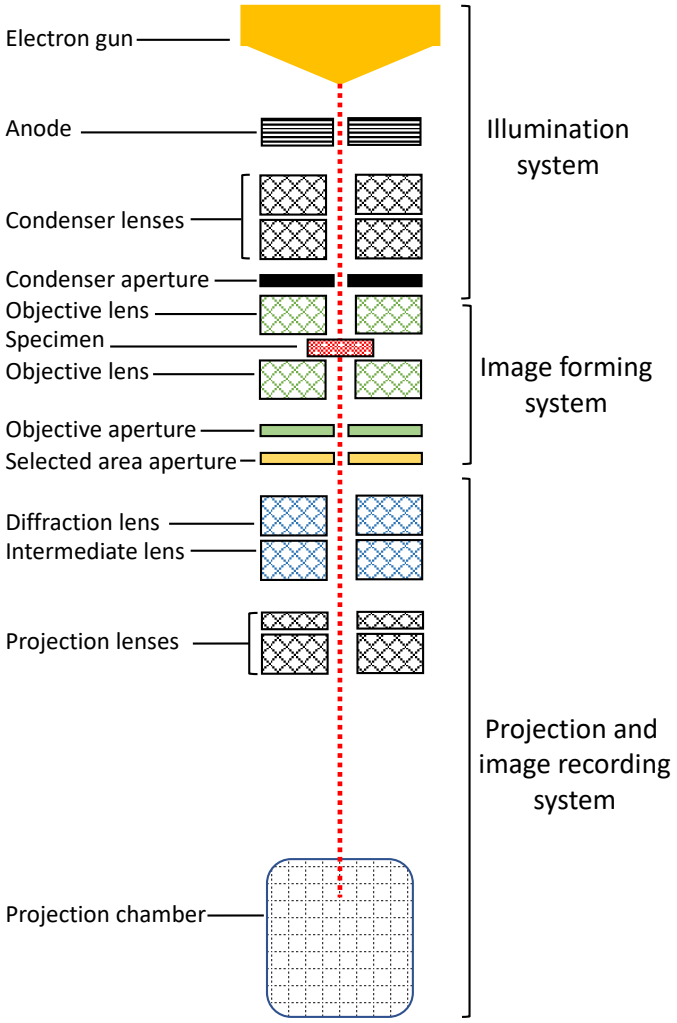

Figure 7-5: Schematic of a TEM column. The illumination system, the image forming system, and the projection and image recording system are schematically shown.

TEM mode and STEM mode

In TEM mode the electron beam is parallel and illuminates the specimen uniformly. The electrons move through the specimen and can be un-scattered, elastically scattered or inelastically scattered. Selecting only the un-scattered electrons a bright field (BF) image of the sample is obtained, and this imaging mode provides thickness and diffraction contrast. When the elastically scattered electrons are selected to form the image, the result is a dark field (DF) image of the sample. DF imaging provides diffraction contrast. In order to select the un-scattered or elastically scattered electrons, the objective aperture is inserted in the back focal plane and only a specific region of the diffraction pattern is let pass. Conventional TEM imaging can be performed using either signal. By contrast, high resolution TEM (HRTEM) imaging is achieved using a large objective aperture (or no objective aperture) and provides phase contrast at atomic resolution. In HRTEM the contrast is produced by the interference of the direct beam and the diffracted beams. The inelastically scattered electrons can be used for EELS or EFTEM. Characteristic X-rays can be collected with an XEDS detector to obtain chemical information from the illuminated region of the specimen. In STEM mode the beam is converged

into the smallest probe possible for the instrument and this probe is scanned on the sample surface. The signal is collected from each point and is integrated in a process conceptually similar to SEM. A smaller probe, and a thin sample, leads to a smaller interaction volume, and this significantly increases the XEDS signal resolution. STEM imaging is achieved by collecting the transmitted electrons for each pixel. The BF-STEM collects the un-scattered transmitted electrons and gives mass-thickness contrast and diffraction contrast. ADF imaging collects electrons scattered between 10 and 50 mrad angle, these electrons include Bragg diffracted electrons and inelastically scattered electrons. HAADF imaging is performed by collecting the electrons scattered at angles higher than 50 mrad. At these high angles electrons diffracted at the Bragg condition are excluded from the signal and only inelastically scattered electrons remain. Figure 7-6 is used to graphically explain the differences between TEM and STEM modes of operation.

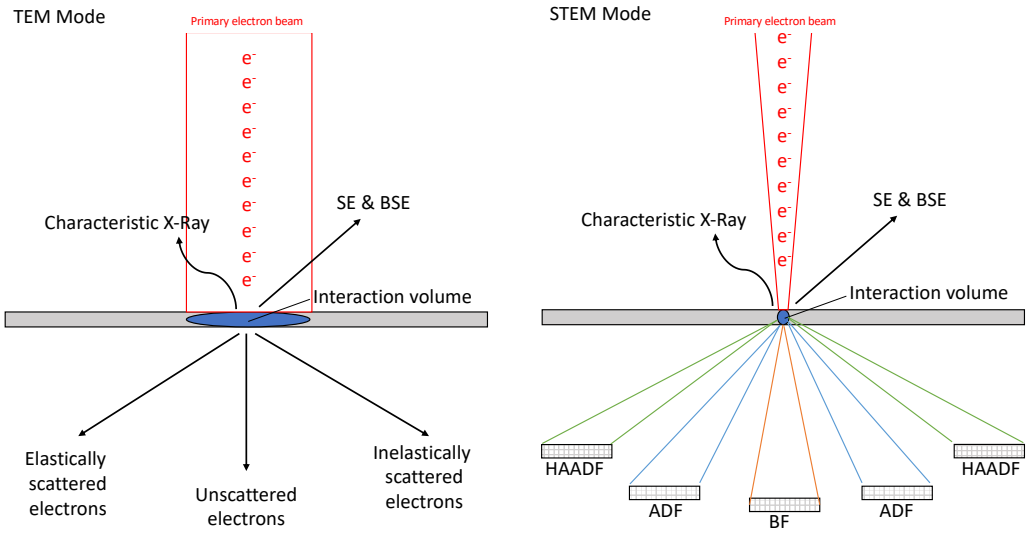

Figure 7-6: Schematic representation of the origin of the different signals used respectively in TEM mode and STEM mode.

Experimental details:

TEM imaging was a crucial technique employed to link the micron scale phenomena to the atomic scale studied with HRTEM and APT. TEM allowed to identify and characterize portions of very thin oxide scales found on autoclave tested materials where the oxide thickness usually ranged between 50 and 300 nm. In SEM, such a thin oxide scale is visible but very little detail can be extracted about its morphology, chemistry or grain structure. With BF-TEM it was possible to image these smaller details while keeping a sense of scale and position on the sample. STEM-EDS was widely used to study the chemistry of very small features that would not be resolved with SEM-EDS. HRTEM was employed to study the crystallinity of the intermixed bonding region found at the Cr-Zr interface of as-fabricated CS-Cr coated Zr-cladding. Sample preparation for TEM based techniques was performed on a FIB/SEM, see Section 7.3. An FEI Tecnai T20 equipped with a LaB_6 electron gun was used in this work to collect BF-TEM images, SADPs and some DF-images. An FEI Titan 80-300 equipped with a FEG electron gun and a Cs corrector on the condenser lens was used to perform HRTEM, STEM and STEM-EDS.

7.2.5 ATOM PROBE TOMOGRAPHY

Overview

Atom probe tomography is the technique that provides the highest resolution for chemical analysis, allowing to study chemical changes down to nearly atomic scale. It allows to reconstruct the data in 3D making it possible to study small details from all perspectives without having to deal with any of the artefacts induced by projecting a 3D object onto a 2D image.

In APT, atoms from needle-shaped specimen are field evaporated in form of positive ions. These ions are then detected and their mass and position in the sample are identified. The collected data is finally rebuilt into a 3D reconstruction that provides extremely detailed information of chemical variations in the investigated sample. In order to create the condition for field evaporation to happen, the needle-shaped specimen is kept in an ultra-high vacuum chamber at cryogenic temperatures (30–70 K) while a high positive direct current (DC) voltage is applied between the specimen and a counter electrode. At this point, a voltage pulse or laser pulse is used to ionize the atoms at the surface of the sample. The ions are then accelerated by the electric field and detected by a 2D position sensitive detector. The time-of-flight for the ions is obtained by measuring how much time passes between the voltage/laser pulse and the detection-event; this time-of-flight allows to extract the mass-to-charge ratio of the ion. As only the atoms at the very surface of the tip are evaporating, one by one, models for calculating the ion trajectory are used to trace backward the ion path to its point of origin. In this way, it is possible to reconstruct the specimen, atom by atom, inside a 3D virtual space. A crude schematic illustration of the instrument setup is shown in Figure 7-7. This technique has been historically utilized predominantly for studies of metallic materials, but the development of laser-APT has opened up the possibility to analyse many non-conductive materials. APT is a powerful characterization technique especially for the study of atom clustering in a matrix, solute segregation at grain boundaries or phase interfaces, phase transformations, and nanoscale materials chemistry in general. The main limitations of APT are the small size of the analysed volumes per specimen, the high mechanical stresses applied on the specimen by the electrical field during the analysis, and the significant role of the operator in handling the data reconstruction process. References for this section are [111–113].

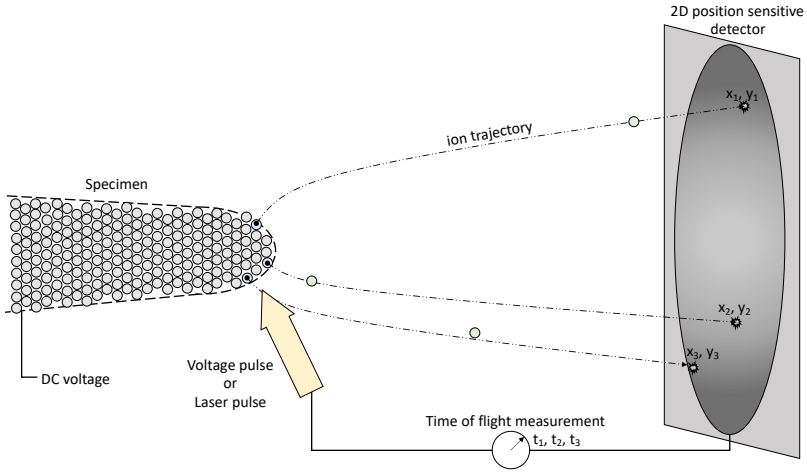

Figure 7-7: Schematic of APT working principle.

Field evaporation

The field evaporation process is at the core of APT. To bring the specimen atoms close to the evaporation energy barrier a strong DC voltage is applied. The sharp needle-shape of the specimen further increases the electric field locally experienced by the atoms at the tip of the needle. Assuming the edge of the sample to be a hemisphere with a radius *R*, a voltage *V* and field factor k_f, the electric field at the tip of the sample can be calculated using the following equation:

$$F = \frac{V}{k_f R} \tag{4.1}$$

This field, together with the temperature at which the specimen is kept, determines the coordinates of the atoms onto the field axis and temperature axis of the diagram presented in Figure 7-8. From Equation 4.1 it is clear that the smaller the radius, the higher the field strength will be locally. During the analysis, the specimen will be slowly consumed, the radius *R* will grow, and the DC voltage V will be increased to compensate for this. The penetration depth of the electric field in the sample is extremely shallow (less than a single atomic layer for metals). This ensures that only the atoms at the very surface of the needle will be exposed to high enough electric fields to be brought close to their evaporation barrier. To push the surface atoms beyond the energy barrier and get them to ionize, extra energy is provided to the system either with a field pulse or a thermal pulse in the form of a DC voltage pulse or a laser pulse, respectively, as shown in Figure 7-8. Field evaporation is a thermally activated process and the most important experimental parameters that affect this phenomenon are: specimen temperature, voltage or laser pulse frequency, voltage pulse fraction or laser pulse energy, and evaporation rate (the fraction of the pulses resulting in a detection event).

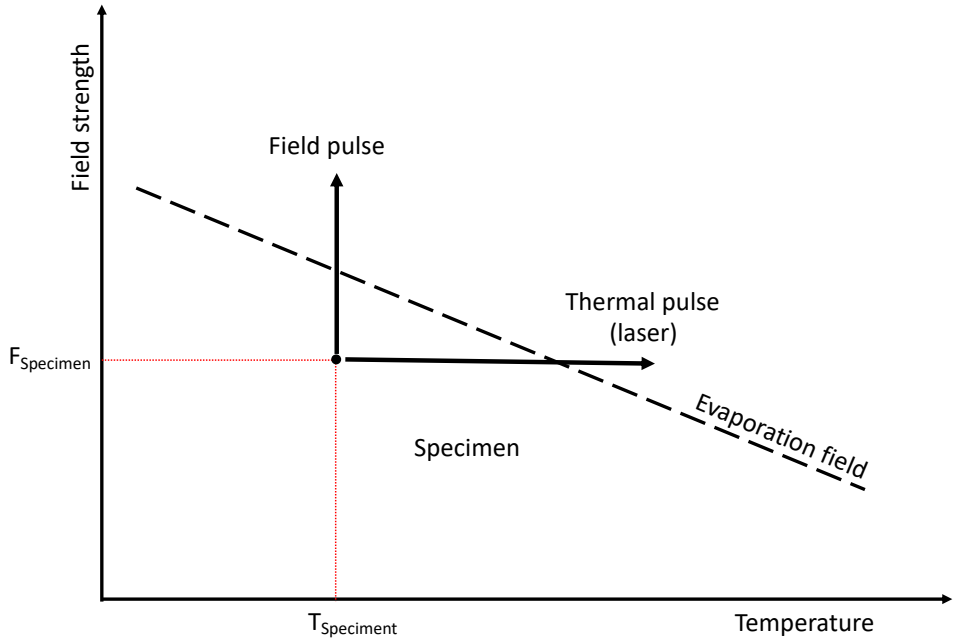

Figure 7-8: Temperature vs Field strength graph, schematic explanation of the role of the voltage/laser pulses.

Data analysis and reconstruction

During the analysis, the x-y position on the detector, the time-of-flight, the voltage applied to the specimen at the time of the event and the other run parameters are saved as data for each single ion. A common analysis can consist of millions of ions and this data needs to be reconstructed before the information about the microchemistry of the sample can be accessed. The atoms that get ionized at the surface of the needle have velocity equal to zero, they are charged and surrounded by a strong electric field, hence they accelerate towards the detector. The distance (l) between the specimen and the detector is known and together with the time-of-flight (t_{flight}) it is possible to deduce the mass-to-charge ratio (m/n) of the ion (see Equation 4-2).

$$\frac{m}{n} = 2eV\left(\frac{t_{flight}}{l}\right)^2 \tag{4.2}$$

The mass-to-charge ratio is used for the identification of the ions, and two examples of mass spectra are shown in Figure 7-9. The peaks are then ranged and assigned to a specific element or molecule (in the case of complex ions). This chemical information is then going to be associated with the positional data in order to create the final 3D reconstruction.

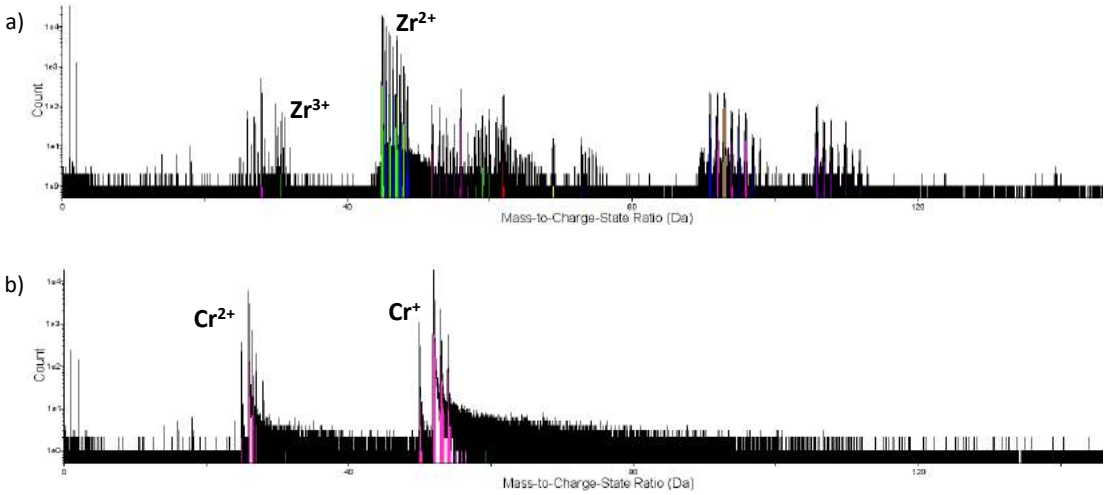

Figure 7-9: Example of mass spectra resulting from analysis of a Zr-alloy (a) and pure Cr (b).

The hit coordinates of each ion are used to determine the original position of the atom on the sample surface. The trajectory of the ions is determined by the geometry of the electric field in which they travel and by which they are accelerated. There are different models to determine the ion trajectory and the accuracy of this process can be affected by the material, phases involved in the evaporation process, shape of the tip, etc. Hence, the reconstruction parameters are extremely important for the final geometry of the reconstructed data. Once the final reconstruction is obtained, important information can be extracted using different visualization and quantification tools. One of the most common ways used to display concentration profiles in 3D involves the use of isosurfaces and proxigrams. An isosurface is any surface where the concentration of a selected element (or group of elements) remains

constant at a set value. By tuning the selected concentration value, it is possible to identify and isolate microstructural features such as precipitates, grain boundaries or phase boundaries. When the desired isosurface/feature is identified, a proxigram (proximity histogram) can be used to analyse the local atomic neighbourhood adjacent to the isosurface. Each ion is associated with its shortest distance from the isosurface. Using this proxigram algorithm, which is independent of the surface geometry, it is possible to generate histograms displaying the concentration of atoms in a series of shells increasingly further away from the selected isosurface. What is obtained in practice is a plot of the chemical composition across and away from the isosurface [114,115]. An example of how isosurfaces work is displayed in Figure 7-10. In order to construct a proxigram, the software divides the dataset into a 3D grid, then it calculates the composition of each voxel, using a delocalization algorithm to smooth the concentration field.

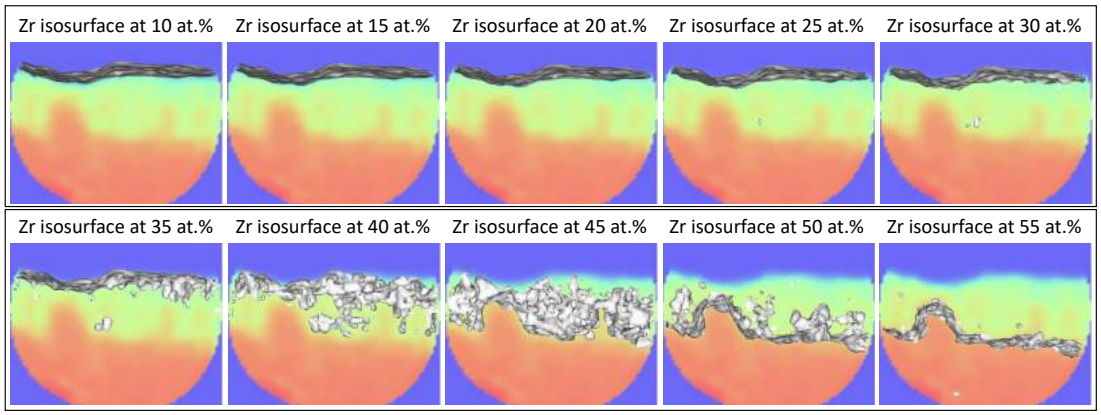

Figure 7-10: Example of isosurfaces calculated at different concentration of Zr at the Cr-Zr interface of an as-fabricated CS-Cr coated Zr-cladding.

Experimental details

Proxigrams were generally calculated starting from an iso-surface, using 0.5 nm steps, 1 nm^3 voxel size and 3x3x1.5 nm^3 delocalization distance.

A LEAP 3000X HR from Imago Scientific Instruments was used to collect the APT data presented in this work about CS-Cr coated material. All samples were run in laser mode with 200 kHz laser pulse frequency, at 50–70 K specimen temperature, 0.3 nJ laser pulse energy and 0.20 % evaporation rate. A LEAP 4000X HR from CAMECA was instead employed for the analysis performed on CrN/NbN SL coated claddings. For these runs, a temperature of 40 K, a laser pulse energy of 70 pJ, and an evaporation rate of 0.50 % were selected. CAMECA IVAS 3.6.14 software was used for data reconstruction and data evaluation. APT was used to study the chemistry of the Cr/Zr interface in the as-fabricated CS-Cr coated OPZ claddings, to investigate the evolution of the Cr/Zr interface after autoclave exposure and to characterize the oxide formed on the surface of the CS-Cr coating during the autoclave corrosion test. In the case of CrN/NbN coatings, APT was used to study the nanolayered structure of the coating and the interface with the substrate before and after autoclave testing.

7.3 Site specific specimen preparation in FIB/SEM

A focused ion beam (FIB) instrument is conceptually similar to an SEM with the important difference of using an ion instead of an electron beam. FIB can be used for imaging but in this work the main application of this technique was as milling tool for *in situ* sample preparation. The FIB/SEM setup used to prepare all the samples analysed with APT and TEM is displayed in Figure 7-11. This instrument is equipped with an electron column mounted vertically and a Ga-ion column mounted at an angle of 52° with respect to the vertical axis (see Figure 7-11a). A gas injection system (GIS) and a micromanipulator (OmniProbe) are also available and can be used together with the two columns to do in situ work. The SEM is mainly used for imaging, but together with the GIS, the SEM can be also used to deposit metallic Pt on the surface of the sample (electron-deposition).

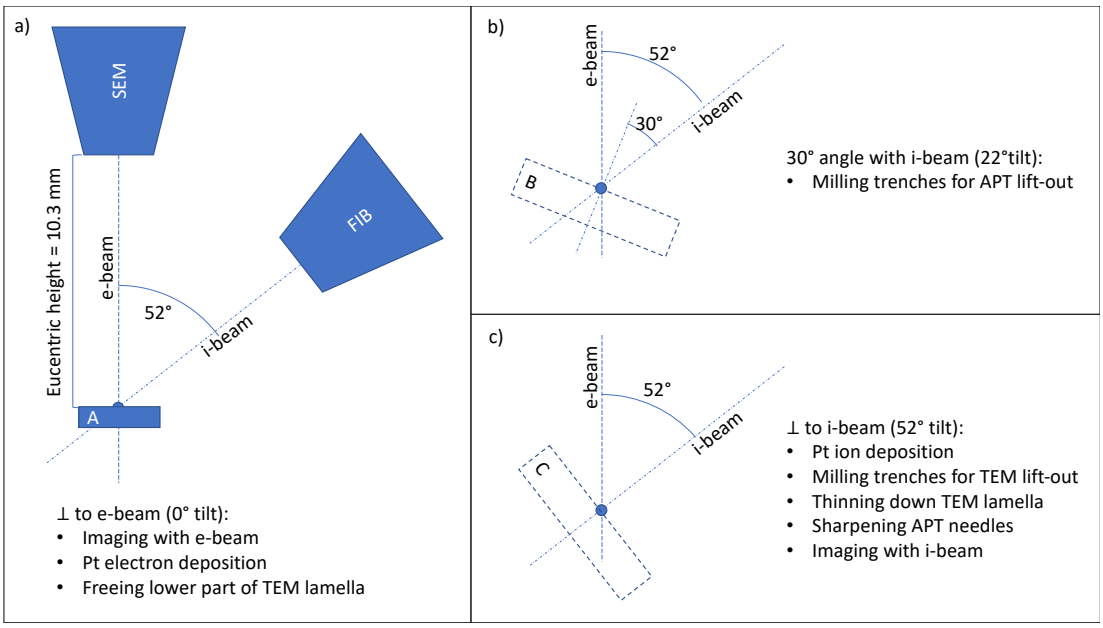

Figure 7-11: Schematic explanation of the FIB/SEM geometry and how the sample is tilted at the different stages of the specimen preparation procedure.

The FIB has imaging capabilities, but it is mainly used to deposit metallic Pt together with the GIS or as a milling tool to create wedges, trenches and other structures at the surface of the sample. The OmniProbe is used to extract a small portion of material from the sample to make it possible to prepare TEM lamellae and APT tips. The stage can be tilted at different angles to orient the sample normal towards the electron or the ion beam, and different angles allow to do different type of milling and Pt deposition as shown in Figure 7-11b and c. In this work, well-known procedures for FIB/SEM *in situ* sample preparation were implemented to lift-out portions of material to be analysed in APT and TEM [116–119].

Site specific specimen preparation with FIB/SEM for APT

The steps involved in the standard lift-out procedure for APT are presented in Figure 7-12. A thin layer of Pt is deposited on the region of interest with electron-deposition (0° tilt), this step ensures that the desired region is visible and recognisable when using the FIB imaging. The sample is tilted to 52° and additional Pt is deposited with ion-deposition on top of the Pt

obtained with electron-deposition, since ion-deposition provides better yield and allows to deposit thicknesses up to one micron. At this point the sample is tilted at 22°, which creates an angle of 30° between the sample surface normal and the ion beam. The FIB is used to mill a trench on one side of the platinum strip, the sample is rotated 180° and a second trench is milled on the other side of the strip. The resulting wedge is then set free at one of the two ends. The sample is moved back to 0° tilt, the OmniProbe is inserted inside the analysis chamber and is put into contact with the wedge. Ion-deposition of Pt is used to weld the OmniProbe onto the free end of the wedge, ion milling is used to free the other end of the sample and the volume of interest is extracted from the sample. Once the lift-out is obtained, the far end of the wedge is put in proximity of a pre-made Si-post (on a wafer with multiple posts). It is then welded onto the Si-post with some Pt and then the wedge is cut with the Ga-beam to separate the welded portion from the rest of the lift-out (see Figure 7-12d and e). This last sequence is repeated until the entire lift-out is made into small portions welded onto Si-posts. The final step of sample preparation for APT is the sharpening. At this stage, the sample is tilted to 52° and annular FIB milling is used to reduce the size of the sample down to a sharp needle, as can be seen in Figure 7-12f (i-v).

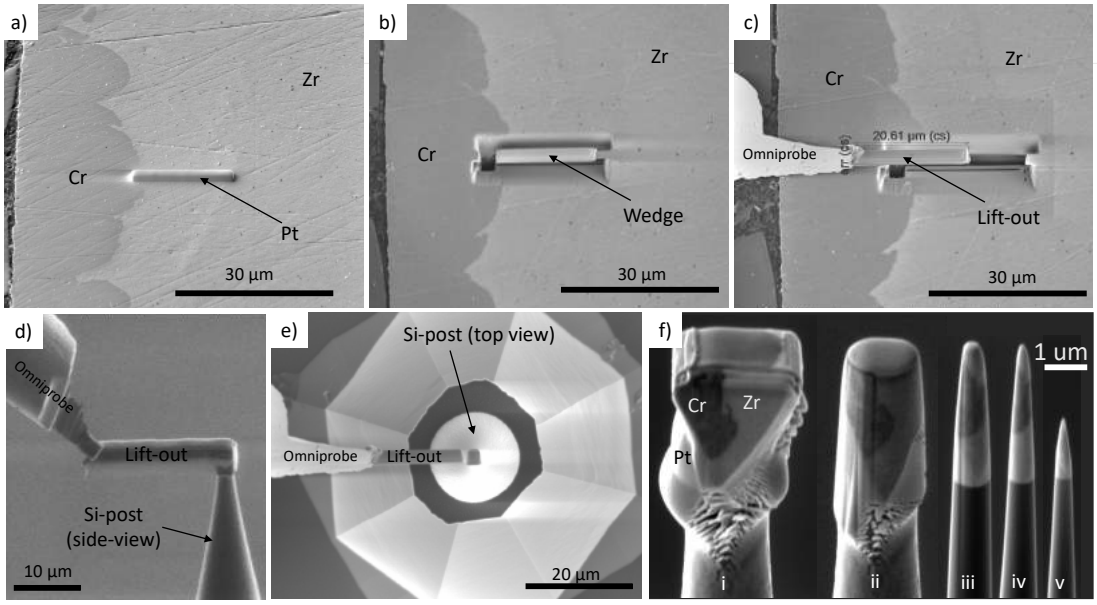

Figure 7-12: In situ lift out procedure for APT: example of steps involved ((a) to (e)). Sharpening of a tip for APT ((f) from I to v).

Site specific specimen preparation with FIB/SEM for TEM and TKD

The procedure for TEM sample preparation has many similarities with the one adopted for APT and it is displayed in Figure 7-13. The region of interest is marked with Pt. The sample is tilted to 52° and this time the milling is done perpendicularly to the surface normal in order to create a lift-out with parallel faces in the shape of a thick lamella. The sample is then tilted to a small angle (between 0° and 7°) and the lift-out is set free with an undercut that leaves only a small portion of material joining the lift-out to the bulk sample. The sample is tilted back to 0°, the OmniProbe is inserted and welded on the lift-out, the thick lamella is set free from the bulk sample, then extracted and mounted onto a Cu half-grid. At this point the sample is tilted to

52° (plus/minus a few degrees), the lamella is thinned and polished down to a thickness of around 50–200 nm using FIB milling.

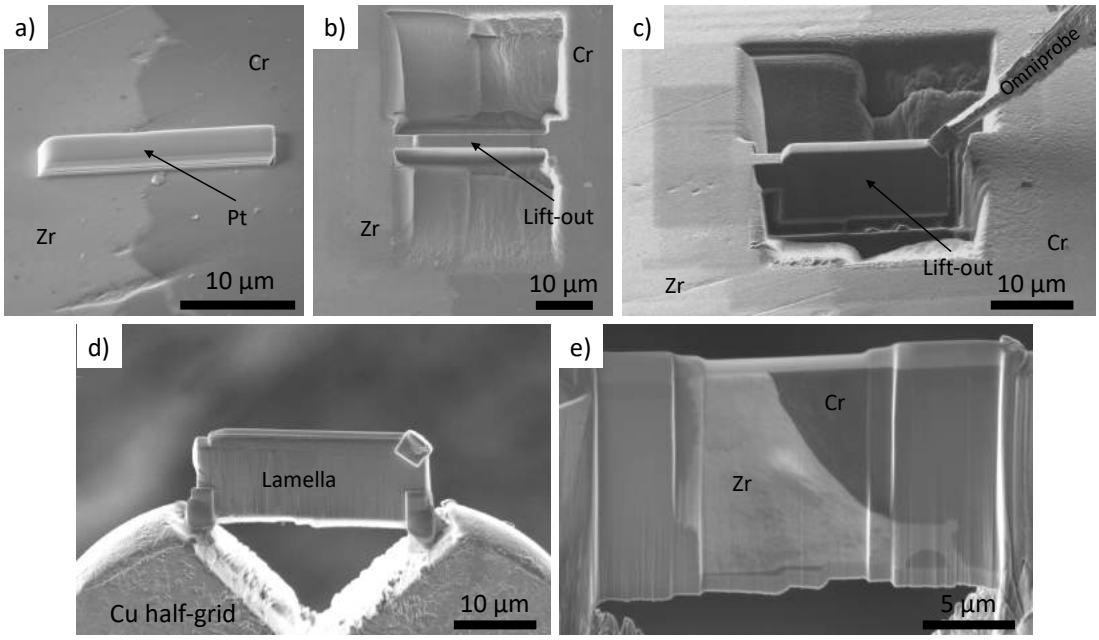

Figure 7-13: In situ lift out procedure for TEM: example of steps involved ((a) to (e)).

CHAPTER 8

SUMMARY OF THE RESULTS

In this section, highlights of the work contained in the appended papers are presented. The experimental results are divided between PWR and BWR application and linked to the research questions presented in Chapter 1.

Question 1
Do ATF coatings offer improved high-temperature steam oxidation under accident conditions?

Question 2
Is chromia stable in LWR operating environments?

Question 3
To what degree do coating and cladding interact during coating deposition, in reactor operation and under accident conditions?

8.1 COLD SPRAY CR PERFORMANCE FOR PWR

8.1.1 AS-FABRICATED CS CR COATINGS ON ZR CLADDINGS

This section deals with results contained in Paper I. The effects of cold spray deposition on the Zr-substrate are relevant for answering *Question 3,* while understanding the adhesion of CS coatings can be relevant in answering *Question 1.*

Understanding adhesion of cold spray coatings

Cold spray coatings have shown very good adhesion properties. Shedding light on the nature of the strong bond between CS-Cr coatings and the Optimized ZIRLO substrate will help to model the behaviour of this system in operation and under accident conditions. Additionally, it could provide important insights into the phenomena that take place during formation of CS coatings. In Figure 8-1a, an SEM overview of the coated cladding cross-section is presented. From this image it is possible to appreciate the significant roughness of the Cr/Zr interface. The interface is much rougher than the original ZIRLO surface. As shown in Figure 8-2b, both the substrate and the coating particles have experienced heavy plastic deformation. The Zr in particular, being the softer of the two metals, has accommodated the Cr particles by wrapping around them and filling all gaps. The result is an interface with a complex shape, where coating and substrate are mechanically interlocked to each other. The convoluted interface represents both a strong advantage and a disadvantage of CS. To the benefits belongs the fact that such a complex geometry makes it difficult for an external load to pull directly onto the interface. This means that even for a weak interfacial bond, the coating would still be stuck, and its spallation would not be easy. The drawback, though, is that such a high degree of roughness inevitably reduces the control over the coating thickness. Although a few micrometres of coating would provide the desired protection, because of the roughness of the interface, more

material is needed to cover the entire surface. In applications where material costs are a limiting factor, this drawback can be significant. It can also influence the neutron economy, as Cr has a higher cross-section for thermal neutrons than Zr.

During coating deposition, both the coating particles and the substrate are subjected to deformation that causes fracturing of the native oxide scale, then the gas jet flushes away the oxide debris. The result is an intimate contact between two bare metallic surfaces, as displayed in Figure 8-2c and Figure 8-2d. This type of interface is very common for CS coatings and is often referred to as metallurgical bonding. The challenge of studying the metallurgical bonding lies in its very small size (nanometre range). Due to the extremely localized heating and shear deformation that produces the bonding, there is no evidence of diffusion or chemical intermixing in the ranges of magnification that can be explored with techniques such as SEM. Even with conventional TEM imaging, the Cr/Zr interface appears to be a sharp and plain line dividing the coating from the substrate. To access this information, near atomic resolution is needed and HR-TEM or APT are required.

Figure 8-2 contains the 3D reconstruction of data obtained from an APT analysis of the very interface between Cr and Zr. From this data, a 20 nm thick intermixed bonding region (IBR) emerges and knowledge about the kinetic and thermal history of this region is obtained. From Figure 8-2a and Figure 8-2b it is clear that between a region of pure Cr and a region of pure Zr there is a layer where Cr and Zr are mixed.

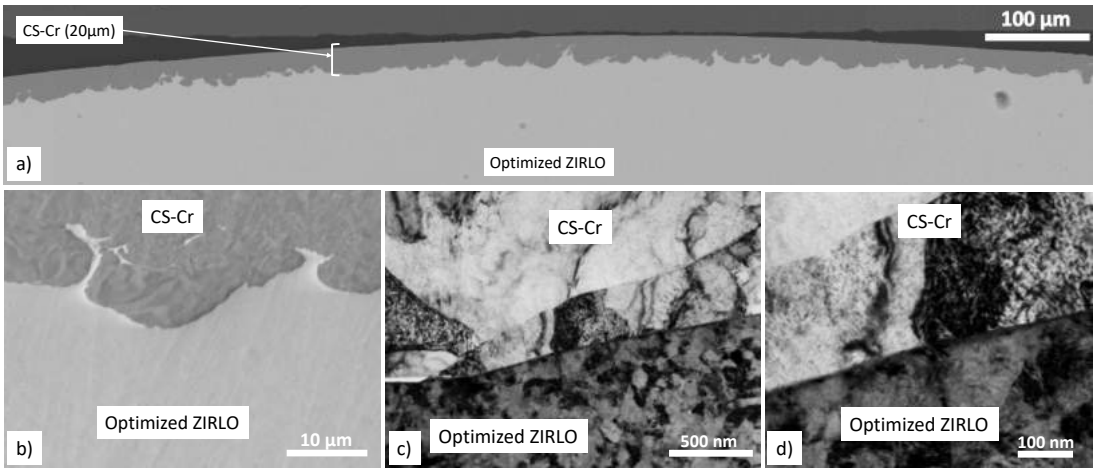

Figure 8-1: Electron microscopy of as-fabricated CS-Cr coated Optimized ZIRLO claddings. (a) Low and (b) high magnification cross-section SEM images. (c) and (d) BF-TEM of Cr/Zr interface.

The average composition of the IBR is approximately 60 at.% Zr, 30 at.% Cr and 10 at.% O as can be extracted from Figure 8-2. The Cr/Zr ratio and the presence of oxygen suggest that the zirconium former surface is the main component of the IBR. The layer contains also traces of Sn, Nb, Fe and C (see Figure 8-2e). Sn, Nb and Fe are alloying elements coming from the Optimized ZIRLO substrate while the carbon could be an impurity potentially originating from grease residues on the former zirconium cladding surface. To have a better view over this layer, a rectangular region of interest is extracted, Figure 8-2c. Here, two things can be observed: the composition of the layer is not uniform and C atoms are mostly concentrated inside Zr-carbide particles. The inhomogeneity of the IBR can be interpreted both as the initial stages of phase separation or as the result of interfacial fluid instabilities. In fact, the composition of the layer

falls into a two-phase region where α-Zr and Cr_2Zr (Laves phase) are the thermodynamically stable phases. The system, if given the chance, would separate these two phases and the differentiation in Zr-rich regions and Cr-rich regions could be interpreted as the first stage of phase separation. On the other hand, as mentioned in Chapter 3, the highly localized plastic deformation that can affect the particle peripheries and substrate surface, can cause the materials to behave locally like a fluid. When two fluids move at different velocities parallel to their interface, surface instabilities can emerge and develop into whirls at the interface. These whirls could then be quenched in place potentially resulting in the inhomogeneities visible in Figure 8-2c.

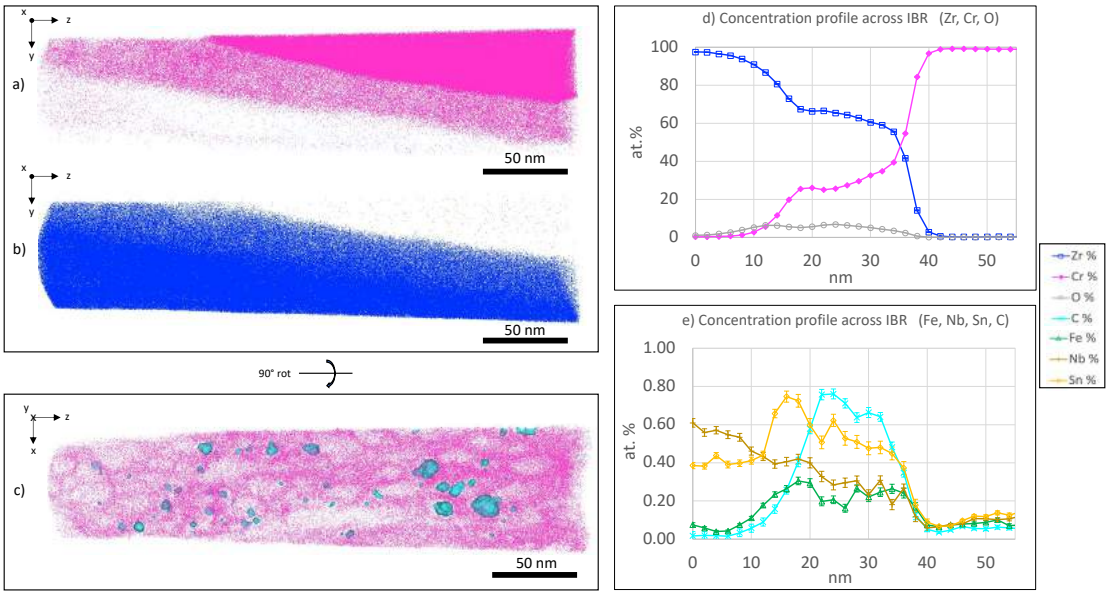

Figure 8-2: 3D reconstruction of APT data from the CS Cr-coating/Optimized ZIRLO™ interface and the area around. In (a) the distribution of Cr atoms (pink, 30 % of the atoms are shown) is displayed, in (b) the distribution of Zr atoms (blue, 30 % of the atoms are shown) can be seen. (c) An image of a 15 nm thick slice containing the intermixed bonding region (rotated 90°) is presented, here the Cr atoms are in pink and the light-blue particles (isosurfaces at 4 at.% C) represent high concentration of C. (d) Concentration profiles across the intermixed bonding region found at the CS Cr-coating/Optimized ZIRLO™ interface.

High-Strain deformation induced microstructures

The properties of the zirconium cladding tubes are strictly regulated. The main advantage of coated zirconium as ATF solution is that very little modification of the existing material and design is required. Nevertheless, the deposition process can have some effects on the substrate and it is important to verify the extent of such modifications. CS coating formation is based on plastic deformation. The EBSD map presented in Figure 8-3a, and the TEM images shown in Figure 8-1c and Figure 8-2d, allow us to investigate the resulting microstructure of the substrate. The EBSD map shows that the grain structure of the substrate is mostly unaffected by the coating, but some effects start to become visible 10 µm or less form the interface with the coating. The microstructure of unaffected Optimized ZIRLO claddings is characterized by a mixture of fine, sub-micron grains and larger grains (see bottom region of Figure 8-3a) while 10 µm from the coating, only the sub-micron grains are visible. Moving even closer to the coating interface, down to 1–2 µm distance from the coating, the signal from the

band contrast map almost disappears. This thin, dark band represents a nanocrystalline layer formed in the Zr-substrate near the interface with the coating. In Figure 8-2c, the nanocrystalline structure of the Zr can be appreciated more clearly. The size of the Zr grains in the region adjacent to the interface is around 50–100 nm. Interestingly, the grains around the interface appear to be coarser in the Cr than in the Zr. This can probably be explained by the difference in hardness between the two metals and the different degrees of strain the two materials consequently were subjected to. The formation of this layer has to be attributed to a dynamic recrystallization phenomenon. At high strains, the large number of dislocations created during plastic deformation start accumulating in dislocation arrays and dislocation walls, evolving eventually into grain boundaries. Through this process, the rotation and tilt introduced into the crystalline lattice by the deformation are accommodated in low energy dislocation structures. With further deformation, these structures can evolve into grain boundaries, finally resulting in fine grains. The same process takes place on the Cr-side, but due to the lower degree of accumulated plastic deformation, the final microstructure of the Cr seems closer to a cell-block structure. In these microstructures, larger regions of material are delimited by thick cell-block boundaries and then further subdivided into cells by thinner dislocation boundaries. The rotation and tilt are usually stored in the cell-block boundaries that work as geometrically necessary boundaries, while the thinner dislocation boundaries emerge mostly as low energy dislocation structures.

8.1.2 CS-Cr coating in PWR autoclave

This section contains a summary of the results and conclusions gathered in Paper II. The results obtained from the autoclave corrosion test performed in PWR water chemistry are used to answer *Question 2*. Coating-cladding interaction during autoclave is also studied to answer *Question 3*.

Evolution of the coating-substrate system under operating conditions

To study the behaviour of the coated cladding and the evolution of the coating/substrate system during operation, the material was exposed to PWR water chemistry in an autoclave at 415 °C for 90 days. The temperature was chosen to be higher than the normal operation temperature in order to speed up all the thermally activated processes and simulate the equivalence of much longer times at reactor temperature. Given the presence of a nanocrystalline layer at the Cr/Zr interface, if anywhere, thermal recrystallization was expected to occur in such a layer. The microstructure of coating and substrate, before and after autoclave exposure, are compared in Figure 8-3. The first thing that can be noticed is that the Zr-substrate has experienced significant recrystallization, especially further away from the coating. However, recrystallization in Optimized ZIRLO is not expected for the operating temperature. The partially recrystallized microstructure typical of this alloy is prone to recrystallization but the threshold temperature for this to happen is usually not reached during operation. The use of a higher temperature for the autoclave testing has activated the recrystallization process, but this result should not be deemed too relevant for the actual performance of the alloy in the reactor. Still, this information can be used for comparison with what happens near the interface with the Cr. In the region close to the coating, almost no recrystallization takes place: the nanocrystalline layer seems to have disappeared, but the existing grains are still far below the micron-size range. One possible explanation is that the

initial absence of large grains in this region does not create the condition necessary to activate Ostwald ripening. In Ostwald ripening, large grains grow at the expense of smaller grains, but without large grains in the 10 µm region from the coating, there is more competition between grains of similar size possibly resulting in less overall recrystallization. Another explanation could be pinning of the grain boundaries by secondary phases. Their presence could slow down grain growth and recrystallization.

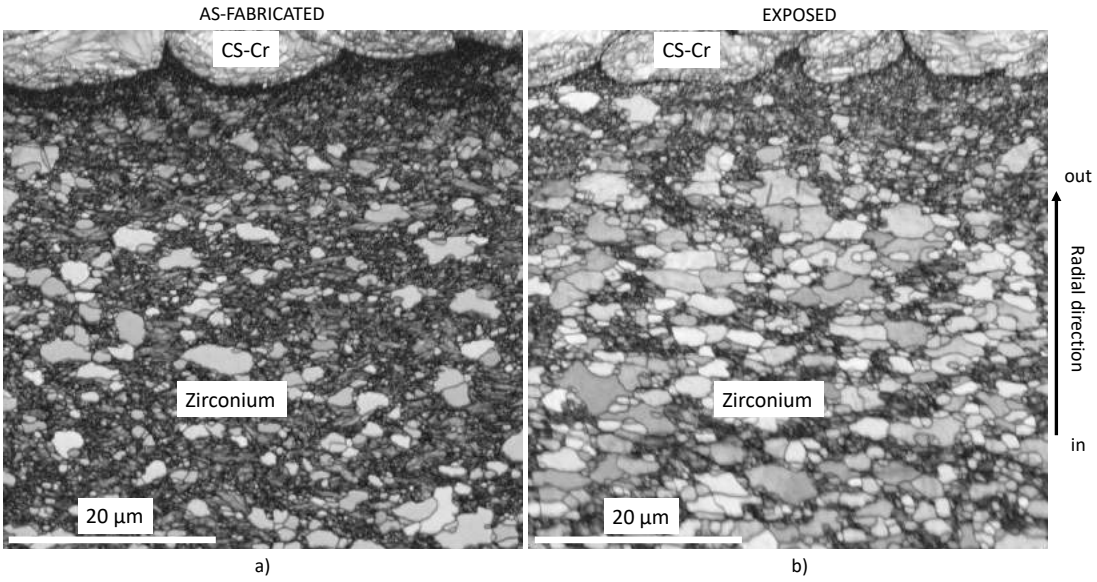

Figure 8-3: EBSD maps of as-fabricated (a) and autoclave exposed (b) CS-Cr coated Optimized ZIRLO cladding cross-sections (map size 50x50 µm²).

Assuming the proximity to the coating to be a factor, diffusion of Cr from the coating into the substrate grain boundaries with subsequent nucleation of Cr-rich phases between grains could result in less recrystallization in the region close to the coating. With this scope, APT was used to explore the interfacial region. Figure 8-4 displays two examples of the main findings. In Figure 8-4 a, a 50x40 nm^2 particle of Cr_2Zr Laves phase is found at the Cr/Zr interface. The chemical composition of this region is around 60 at.% Cr and 30 at.% Zr, the opposite of the IBR composition measured in the as-fabricated sample. The O content in the Cr_2Zr Laves phase is close to zero, and the oxygen previously contained in the IBR has now migrated to the Zr-substrate. Overall, the IBR seems to evolve under autoclave exposure and the system appears to move toward thermodynamic equilibrium. The composition and thickness of the IBR after autoclave varies substantially from place to place. Generally, it can be said that there is some degree of chemical evolution happening and that the presence of Cr_2Zr nuclei distributed along the interface is the most relevant phenomenon. In fact, the nucleation step of a new phase is the main limiting factor in the precipitation of secondary phases from a solid solution. Hence, if the Laves phase can nucleate already under operating conditions, when given the chance at higher temperature, the Cr_2Zr will start to grow right away. It is still important to underline that the autoclave temperature was higher than the operating temperature. This difference might have triggered phenomena that would not have happened under normal conditions. Only in-reactor testing over long periods can provide definitive results. The second interesting information provided by the APT investigation is the presence of a Zr-Cr-Fe phase found precipitating at Zr grain boundaries in the substrate adjacent to the Cr/Zr interface in a band a

few hundred nanometres thick. The composition of this phase (48 at.% Cr, 44 at.% Zr and 8 at.% Fe), despite small fluctuations, is quite consistent across different regions of the same APT run and across different runs obtained from different regions of the interface. This would suggest that such a phase is nucleating consistently where the right conditions are created. Cr was already found diffusing into the substrate along grain boundaries for similar distances in the as-fabricated material. Hence, it is not too surprising to find it in this phase. Optimized ZIRLO contains small amounts of Fe as alloying element but most of it is usually contained in SPPs. Nevertheless, Fe is a fast diffusor in Zr, and it is reasonable to imagine it diffusing and forming energetically favourable phases. The presence of this phase could be one of the factors preventing thermal recrystallization of the substrate region near the interface with Cr.

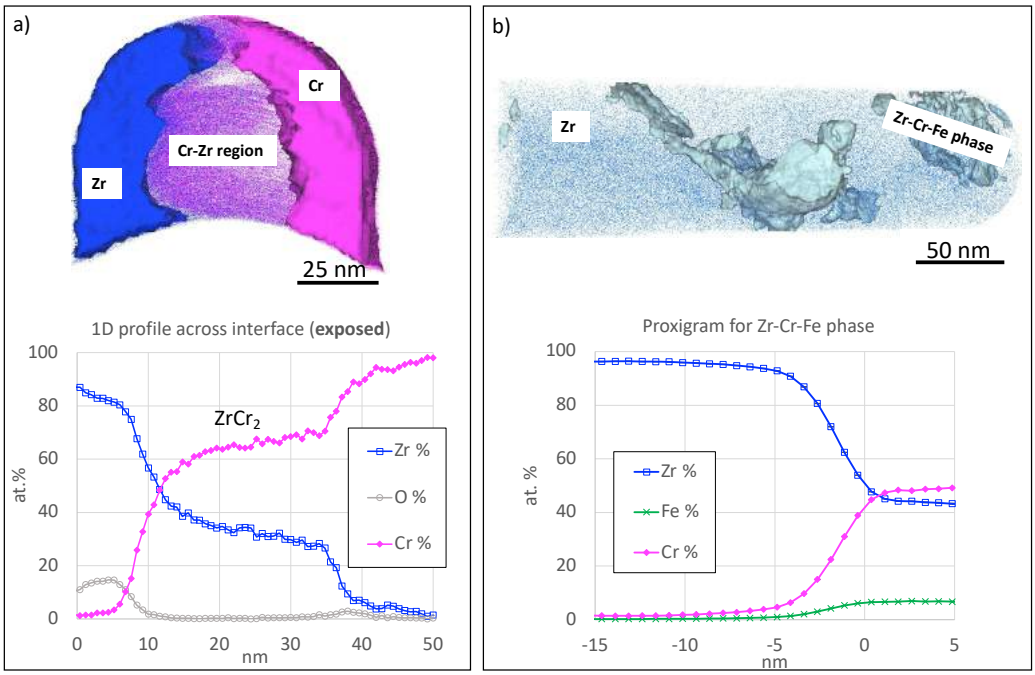

Figure 8-4: (a) 3D reconstruction of APT data from the Cr/Zr interface of CS Cr-coated Optimized ZIRLO claddings exposed to autoclave (top). Cr atoms in pink, Zr atoms in blue. The blue surface represents the Zr-substrate, the pink surface represents the Cr-coating. 1D composition profile across Cr/Zr interface of autoclave exposed material (bottom). (b) 3D reconstruction of APT data from the Zr-substrate exposed to autoclave, 100–200 nm distance from the Cr/Zr interface (top). Zr atoms in blue (only 1 % shown). Light blue surface encloses a Zr-Cr-Fe phase (isosurface set at Fe+Cr content of 35 at.%). Proxigram across Zr-Cr-Fe phase isosurface (bottom).

Corrosion protection under operating conditions

The main aim of the ATF concept is to provide better performance than that of traditional materials when exposed to accident conditions. Yet, it is crucial for the accident tolerant material to be able to perform as well, if not better, as the traditional Zr claddings when subjected to normal operating conditions. As introduced in Chapter 2, oxidation of Zr cladding is one of the factors limiting fuel rod life and any improvement on this front is considered an additional advantage of the application of CS-Cr coatings. To examine the oxidation protection offered by the Cr coating, cross-sectional TEM imaging and APT were employed (see Figure 8-5). From the TEM imaging it is possible to measure the thickness of the oxide scale formed on the surface of the coating during autoclave exposure. This oxide appears to be 50–100 nm

thick and compact. The presence of small voids along the oxide/coating interface seems to suggest an outward growth of the oxide. The APT data provides information about the chemical composition of this oxide scale (close to 60 at.% O, 40 at.% Cr) which suggests that the oxide is chromia (Cr_2O_3), as oxygen is often slightly underestimated using APT. In the TEM images, small particles can be found further away from the surface of the coating. In APT data, these particles appear to be chromia particles. However, the occurrence of internal oxidation seems unlikely and these oxide particles have probably been embedded in the material during the process of surface grinding and polishing that is performed after the coating deposition. Overall, considering that 1 µm thick oxide can be found on ZIRLO after only 10 days of autoclave exposure at 360 °C [120], the development of a 100 nm thick chromia scale after 90 days at 415 °C can be definitively considered a significant improvement.

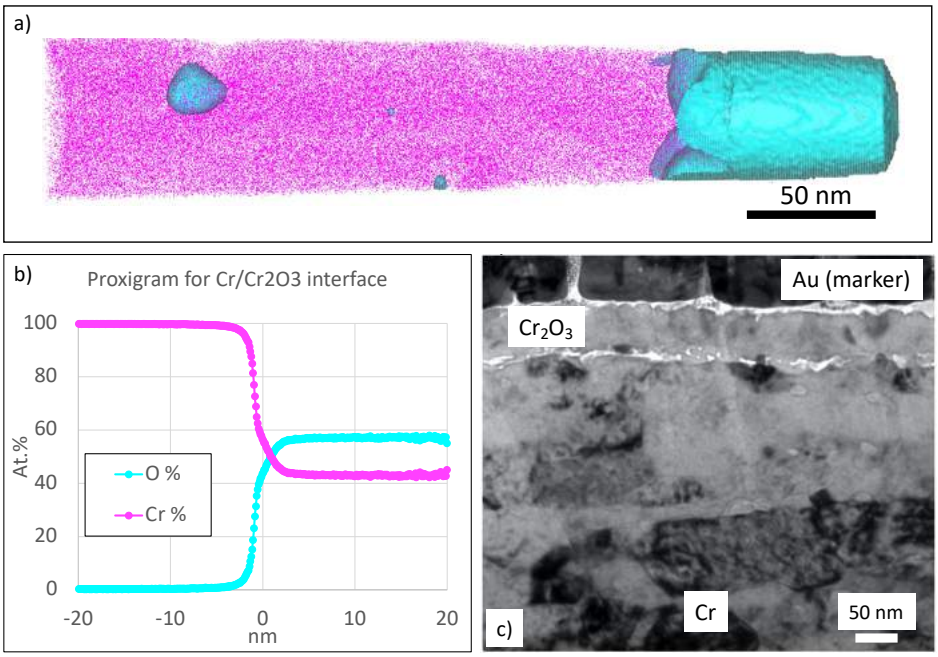

Figure 8-5: (a) 3D reconstruction of APT data from the CS Cr-coating outer surface after autoclave exposure. Cr atoms in pink (30% of the atoms are shown), the light-blue surfaces represent chromium oxide (isosurfaces at 20 at.% O). (b) Proxigram displaying the composition profile across the Cr/Cr_2O_3 interface. (c) BF-TEM image of Cr_2O_3/Cr interface at the cladding outer surface after autoclave exposure.

8.1.3 CS-Cr COATED CLADDING UNDER SIMULATED LOSS-OF-COOLANT ACCIDENT CONDITIONS

The following section summarizes the results presented in Paper III. Studying the performance of CS-Cr coatings in simulated accident environment is crucial in answering *Question 1*. *Question 3* is also answered, and the interaction between the coating and the substrate during exposure at high temperature is studied in depth.

Oxidation protection and accident tolerance

As anticipated multiple times in this work, the main improvement that ATF coatings must provide is better performance under accident conditions. The main undesired reaction when accident strikes is the exothermal oxidation of Zr provoked by the interaction with steam at

very high temperature. When this happens, Zr starts its transformation into ZrO_2, H_2 is produced, the cladding mechanical properties are compromised, and cladding failure becomes almost inevitable with the potential risk of losing the coolable geometry of fuel assemblies and the core. Delaying the reaction between hot steam and Zr-claddings is crucial, and this is the main objective of the Cr-coating. In order to test the ability of CS-Cr coatings to protect the substrate cladding, steam corrosion tests performed at 1200 °C, at 1 atm in flowing steam, for 3 min, 20 min, and 40 min were conducted on small portions of coated cladding tubes. The overall results of this set of tests are shown in Figure 8-6. The most important takeaway is that the CS-Cr coating is able to withstand the oxidation testing conditions with little signs of early failure for up to 40 min. A compact and stable scale of chromia grows progressively following a parabolic growth rate as displayed in Figure 8-6 a. In the early stages of oxide formation, the scale seems to follow an outward growth mechanism, while between 3 min and 20 min the mechanism transitions to a mixed inward-outward growth. Once this second stage is reached, the growth rate starts decreasing with the thickness of the oxide layer and a slower oxidation rate is achieved. When compared with the oxidation of the uncoated inner wall of the cladding tube presented in Figure 8-6 b, the difference between the oxidation of the coating and the oxidation of the base material becomes obvious: after 40 min the Cr has developed a 8 µm thick, dense scale of chromia, while the inner wall presents 80 – 100 µm of ZrO_2 plus 100 – 120 µm of oxygen saturated α-Zr.

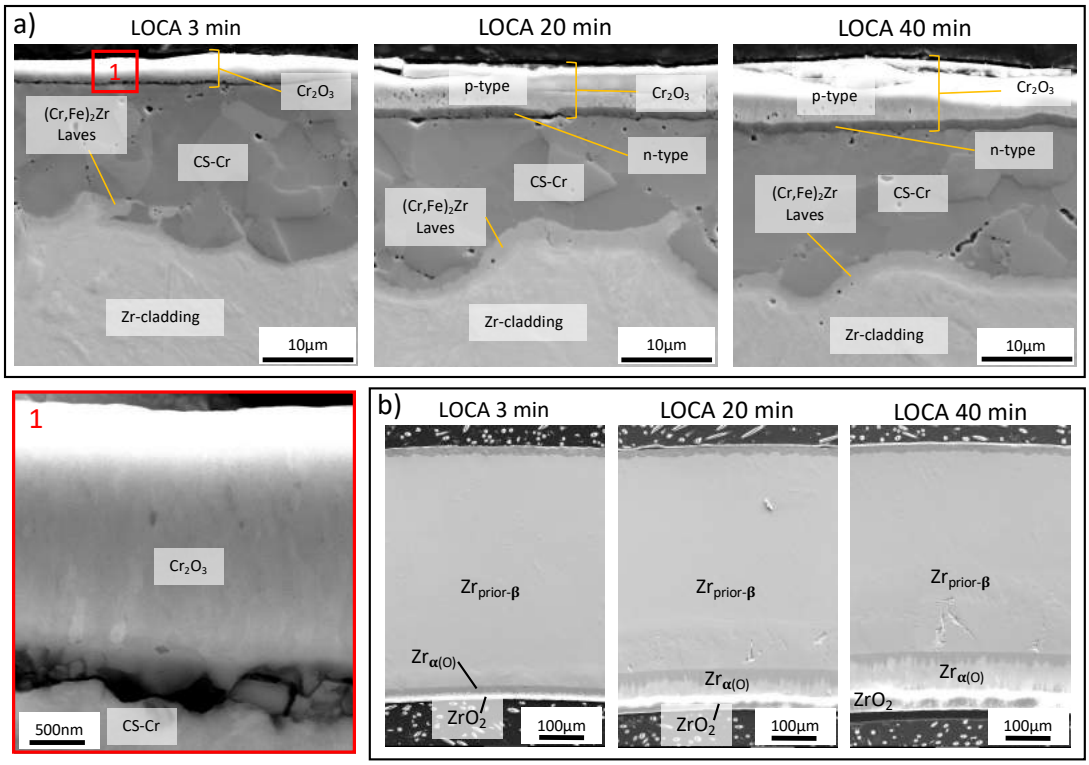

Figure 8-6: SEM cross-section imaging of cold spray Cr-coated Optimized ZIRLO cladding tubes exposed to loss-of-coolant-accident condition (1200 °C in steam) for 3 min, 20 min and 40 min, respectively. (a) Detail of the outer cladding wall, Cr-coated, after exposure. Due to the different electronic properties, n-type and p-type chromia present different contrast in electron microscopy. Box 1 offers a magnified view of the oxide scale and the oxide/metal interface after 3 min of exposure. (b) Overview of the full cladding cross-section: the uncoated inner wall of the cladding is shown and the degree of oxidation suffered by the bare Zr-alloy is visible.

Beyond the oxidation of the outer surface of the coating, a few additional phenomena can be observed in the CS-Cr after the high-temperature oxidation test: full recrystallization of the coating, development of some porosities, and the reaction/interdiffusion with the Zr-substrate. The recrystallization of the Cr coating can be appreciated by comparing Figure 8-1 b and Figure 8-6 a, but a better representation of this phenomenon is shown in Figure 8-7. Here, EBSD maps (inverse pole figures - IPF) for the Cr coating and the Laves phase found at the Cr-Zr interface are plotted for as-fabricated samples and for samples exposed to autoclave testing and high-temperature corrosion testing. Looking at the IPFs for Cr, the severely deformed microstructure of the as-fabricated coating appears immediately, some small signs of recrystallization can be seen already after autoclave exposure, but the most significant changes can be observed after 3 min at 1200 °C. The coating undergoes full recrystallization after 3 min at 1200 °C, large grains (5–10 µm in size) appear, no strain or rotation of the crystal can be observed inside these grains in the bulk, and basically no further grain growth can be observed for samples exposed for 20 min and 40 min. The coating thickness decreases significantly after 20 min and 40 min. This has to do with the progressive oxidation of the coating plus the dissolution of Cr into the Laves phase and the Zr-substrate. For the samples exposed to high temperature, the higher thickness of the Laves phase layer developed at the Cr-Zr interface allowed it to be mapped with EBSD. This phase presents grains in the 1 µm range that generally stretch across the entire thickness of the Laves layer. No significant evolution of the microstructure of this phase is observed over the different exposure times. The coating interaction with the substrate deserves its own section and it is discussed next.

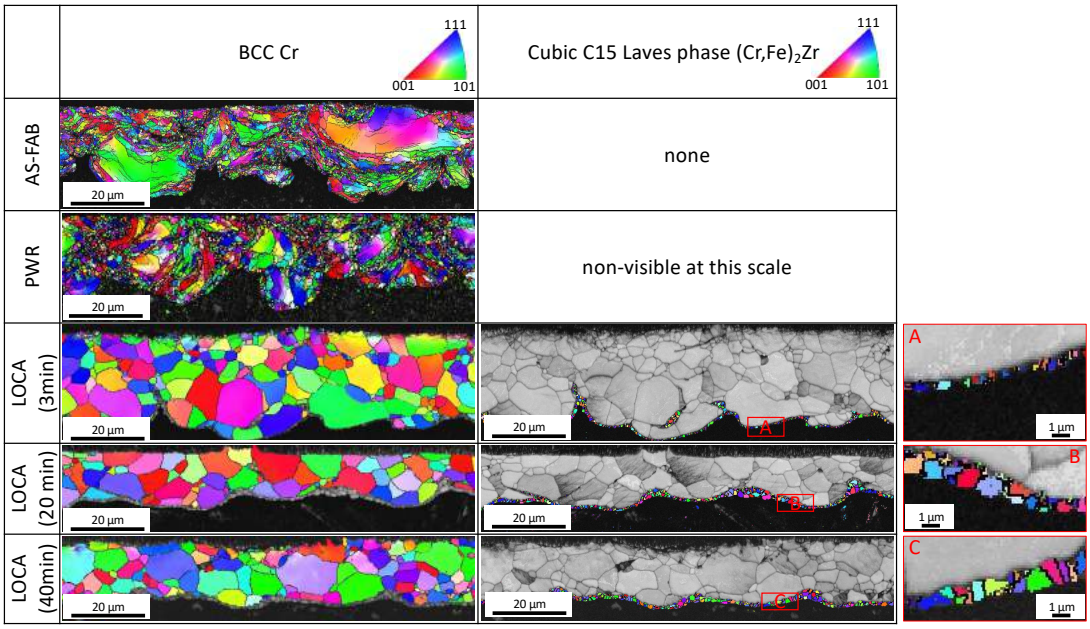

Figure 8-7: EBSD cross-section maps of cold spray Cr-coated Optimized ZIRLO cladding tubes as-fabricated, exposed to PWR autoclave, and exposed to loss-of-coolant-accident condition (1200 °C in steam) for 3 min, 20 min and 40 min (Cr-coating is on top and Zr-substrate at the bottom). Left column: Band contrast map + IPFz maps for BCC Cr. Right column: Band contrast masp + IPFz maps for cubic C15 Laves phase $(Cr,Fe)_2Zr$. Box A, B and C show a higher magnification portion of the cubic C15 Laves phase $(Cr,Fe)_2Zr$ IPFz maps presented in the right column.

Coating-cladding interaction during exposure to high-temperature

The Cr-Zr interface of a coated cladding behaves as a diffusion couple with the formation of an intermetallic component at the interface and reciprocal interdiffusion. As visible in Figure 8-6, Figure 8-7, and Figure 8-8, the $(Cr,Fe)_2Zr$ Laves phase starts growing immediately after 3 minutes exposure and reaches a thickness of around 1-2 µm after 40 min. Its thickness is homogeneous across the cross-section and its microstructure is characterized by gains 1 µm in size that can stretch across the entire layer. Through the collection and identification of DPs, this phase was identified as a cubic, C15-type Laves phase. Using STEM EDS it was possible to measure the chemical composition as 64 at.% Cr, 1–2 at.% Fe and around 33 at.% Zr. Some impurity Fe can be found in the coating, but the vast majority of the Fe is most likely coming from the Zr-substrate. Optimized ZIRLO contains small amounts of Fe (0.09 – 0.13 wt.%) contained mostly inside Fe-rich SPPs distributed in the Zr matrix. The Fe enrichment of the intermetallic layer at the Cr-Zr interface must be linked to a loss of Fe from the SPPs. Beyond the interface, Cr is found diffusing into the substrate for up to 300 µm (at 1200 °C after 40 min). At this temperature the solubility of Cr in Zr is around 5 at.%, this value is measured adjacent to the Laves-Zr interface, but the Cr content progressively decreases further away from the coating, following a diffusion profile. This Cr alloying is responsible for the formation of the Cr-rich precipitates visible in Figure 8-8 a; when the samples are cooled, the Cr solubility in the Zr drops and Cr-rich particles will form. On the other side of the Cr-Zr interface, no Zr is present in the Cr bulk, but Zr-rich particles can be found nucleating and growing quite consistently along the grain boundaries of the recrystallized Cr coating. These particles are shown in Figure 8-8 b and both the chemical analysis and the electron diffraction have confirmed this phase to be ZrO_2. The presence of ZrO_2 particles along the Cr grain boundaries implies that Zr manages to diffuse along these paths of high diffusivity and meet O atoms diffusing all the way from the outer surface of the oxidized coating. These ZrO_2 particles are expected to grow for longer exposure times, until a continuous network of ZrO_2 is formed across the remaining unoxidized Cr coating. Once this network has formed, the coating is no longer protective and O is allowed to diffuse from the outer oxide to the Zr substrate, as reported in literature [27].

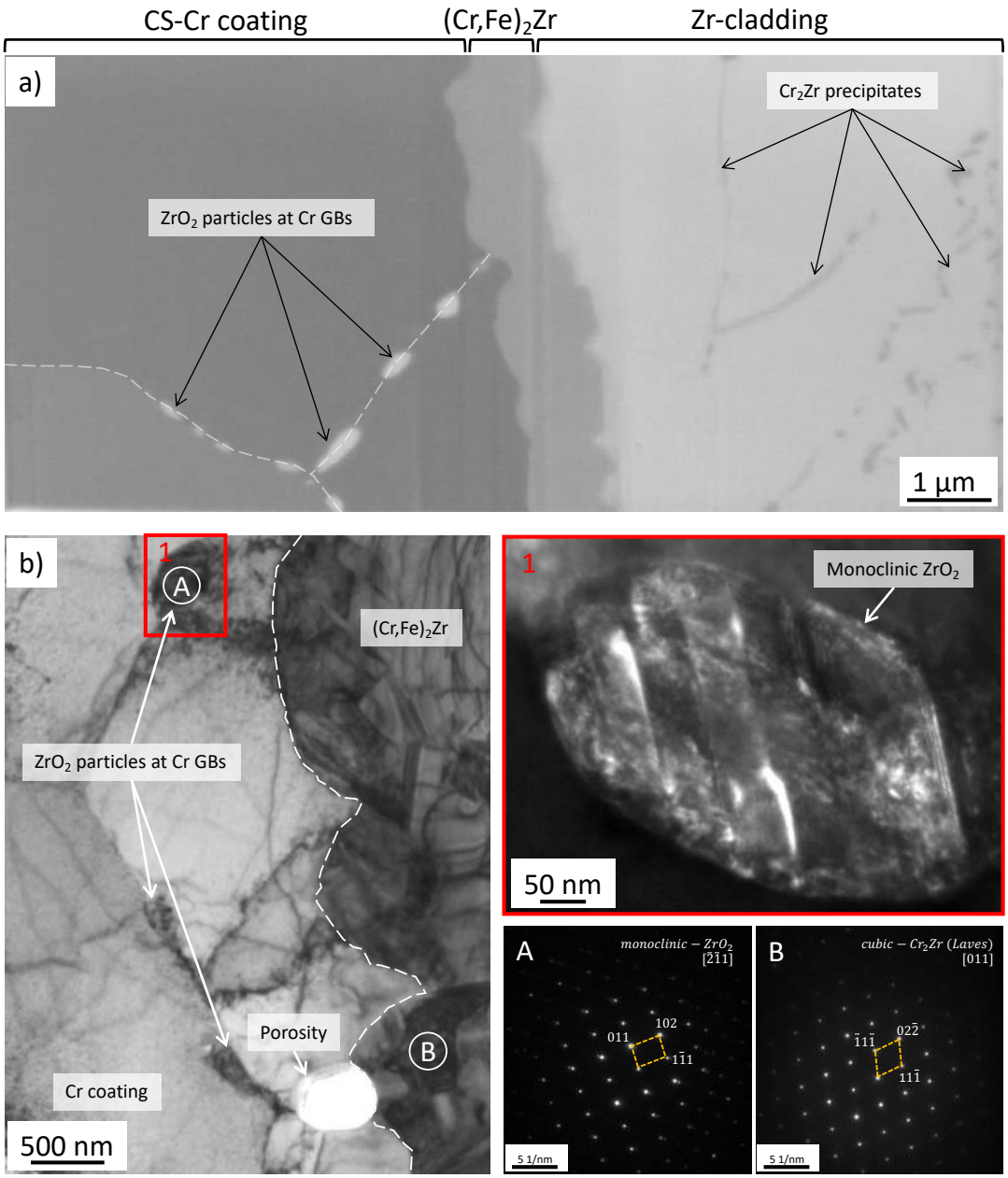

Figure 8-8: Cold spray Cr-coated Optimized ZIRLO cladding tubes exposed to loss-of-coolant-accident condition (1200 °C in steam) for 40 min. a) SEM image of FIB cross-section of the interface region between Cr-coating and Zr-substrate. (The white dashed line indicates the grain boundaries of the recrystallized Cr.) b) BF-TEM image of the interface between $(Cr,Fe)_2Zr$ and the Cr-coating after 40 min in LOCA conditions. Box 1: Detail of monoclinic ZrO_2 particle found at a Cr grain boundary. Selected area diffraction Pattern A and Pattern B are, respectively, collected from a ZrO_2 particle and a $(Cr,Fe)_2Zr$ grain. (The white dashed line indicates the phase interface between Cr and $(Cr,Fe)_2Zr$.)

8.2 PWR vs BWR: STABILITY OF CHROMIA

The most salient results and conclusions drawn from Paper IV are presented in this section. The experiments presented here focus mostly on answering *Question 2*, and show that pure chromia is suited for PWR operating environment but is dissolved in BWR water chemistry.

An ATF coating has to improve the resistance to accident conditions, but it must survive operating conditions as well. Assuming an accident can strike at any random moment in the lifetime of a coated fuel assembly, the coating has to be able to perform as intended throughout the entire life cycle of the tube. Additionally, as the industry tries to employ new materials, combining enhanced accident tolerance and superior performance during normal operation seems to be a better commercial case. In order to improve performance under nominal operating conditions, the coating needs to survive such conditions. As anticipated in Chapter 5, depending on oxygen concentration, temperature, pressure and concentration of dissolved ionic species in the water, chromia can become thermodynamically unstable and favour formation of soluble phases. This process is highly undesired, as the progressive dissolution of Cr-containing species into the coolant implies the continuous depletion of a chromia-forming coating. In PWRs, the oxygen concentration in the cooling water is very low (usually modelled as <45 ppb of O_2 in autoclave water), which protects the chromia from further oxidation. But the same cannot be said about BWRs. In BWRs the activity of oxygen is much higher and can reach values equivalent to 8 ppm of dissolved oxygen. Looking at Figure 5-3a (Pourbaix diagram calculated at 300 °C, 10 MPa, 10^{-6} mol/kg of dissolved species), it is clear how increasing the concentration of oxygen in the water (hence moving towards the top water line), one exits the field of Cr_2O_3-stability and enters a region of $HCrO_4^-$-stability. $HCrO_4^-$ is soluble, which means that any chromia forming coating will progressively oxidise and dissolve into the corroding environment. One experimental example of the different challenges offered by PWR and BWR to materials is presented in Figure 8-9. CrN is a potentially interesting coating, it is a chromia former and it has very high hardness. Elevated hardness is considered important for BWRs as the issue of debris fretting during operation is much more prevalent for this reactor design and represent an important issue that could benefit from material renewal [121].

In PWR autoclaves, CrN seems to be protective, some oxidation occurs on the outer surface, with some additional penetration of O into the nitride coating. When exposed to BWR autoclave conditions instead, no coating is left to be found after the test, and a 2 µm thick layer of ZrO_2 has grown on the surface of the Zr-substrate. From this simple experiment it is difficult to know the precise sequence of phase formation and dissolution that brings the coating to behave differently in the two tested environments, but it is reasonable to assume that the stability of chromia would be necessary for this coating to effectively passivate. A proposed mechanism for the oxidation of CrN in PWR and BWR is presented in Figure 8-10. In PWR, oxygen starts entering the CrN coating forming Cr(O, N), the degree of substitution of N by O is expected to be higher close to the outer surface and progressively decrease moving inwards, towards the bulk of the coating. Beyond a certain level of O substitution in the Cr(O, N) lattice, Cr_2O_3 is expected to nucleate and start to grow into a passivating layer. As Cr_2O_3 is stable in PWR water chemistry, this layer will build up to the point where diffusion through the oxide will be limiting for further oxidation to occur.

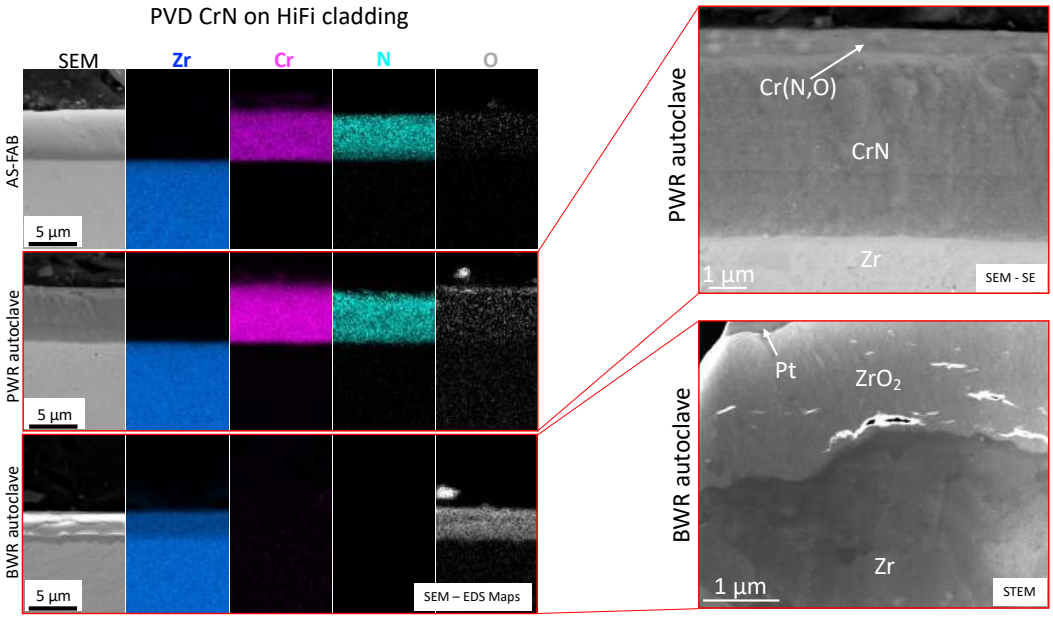

Figure 8-9: SEM cross-section imaging and EDS mapping. CrN coating on HiFi® cladding: as fabricated, after PWR autoclave exposure, and after BWR autoclave exposure (left). SEM and STEM cross-sectional images of the outer surface of the coated claddings after auto-clave exposure. SEM image of CrN-coated cladding after PWR autoclave exposure (top-right); STEM image of CrN-coated cladding after BWR autoclave exposure (bottom-right).

In BWR, Cr_2O_3 is not thermodynamically stable. Oxygen will penetrate into the CrN lattice forming Cr(O, N), but any further oxidation of the oxynitride will ultimately result in soluble products, which will dissolve in the autoclave water. Ultimately, the entire coating will have gone through this process and the bare surface of the Zr-cladding will become unprotected, allowing for the formation of ZrO_2. Because this mechanism is driven by the absence of any solid product of the oxidation reaction of Cr, it is reasonable to expect any other chromia-forming coatings to behave in a comparable way.

As can be appreciated in Table 7-2, most of the coatings that were expected to form chromia dissolved during BWR exposure. The other large family of coatings presented in Table 7-2 is represented by coatings based on TiN or TiAlN. These coatings managed to form a stable TiO_2 scale in BWR autoclave but failed to protect the Zr-substrate. Spallation was often observed and oxidation of the coating/substrate interface was widely present across most of the analysed cross-sections.

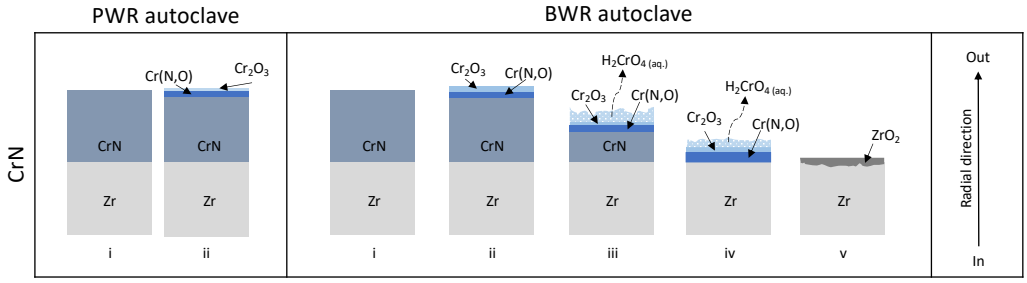

Figure 8-10: Schematic of the proposed corrosion mechanisms for CrN in PWR autoclave and BWR autoclave environments.

8.3 PVD NITRIDES IN BWR

Some of the results contained in Paper V are presented in the following section. The results presented here are linked to *Question 2*, and explore the effects of Nb in the formation of a stable Cr-rich oxide in BWR simulated environment.

The dissolution of chromia-forming coatings in BWR environment made it challenging to find a suitable coating for this reactor type. As displayed in Table 7-2, a wide range of coatings were tested and all but the CrN/NbN superlattice coating failed either by dissolving into the water or by forming unprotective oxide scales and spalling away. Another superlattice coating composed of CrN and TiN was tested but spallation of the formed oxide was observed. The concept of superlattice describes a solid where two different crystal structures are repeated in alternating layers to achieve an artificial periodicity. A superlattice is usually described by the forming phases and by the thickness of the layers (in nm or number of unit cells) [122]. The superlattice coating studied in this work is a nanolayered structure where alternating layers of CrN and NbN are stacked on top of each other along the deposition direction. This layered structure is surely relevant for the performance of the coating, but it is important to keep in mind that the CrN/TiN superlattice did not survive the BWR simulated environment, which suggests that Nb is playing the most important role in the overall behaviour of the CrN/NbN superlattice coating.

8.3.1 EFFECT OF NB ON THE STABILITY OF CR-RICH OXIDES IN BWR OPERATING CONDITIONS

An overview of the CrN/NbN SL coated cladding before and after BWR autoclave exposure is presented in Figure 8-11. From the SEM cross-section of the as-fabricated coating it is impossible to discern the layered structure of the SL and the coating appears as a single homogeneous phase. The average composition of the as-fabricated coating measured with SEM-EDS is around 33 at.% Cr, 17 at.% Nb, and 50 at.% N, representing a (Cr, Nb)N with a Cr:Nb ratio of 2:1. After 60 days in autoclave, it is possible to distinguish that a thin layer of oxide has developed on the outer surface of the coating, but no other difference can be noticed in the bulk of the coating. BF-TEM images allow us to access the superlattice structure and the alternating layers of the as-fabricated sample are clearly visible in Figure 8-11. The coating is characterized by columnar grains elongated in the coating deposition direction, typical of MS-PVD coatings. The layers are clearly defined in most of the visible cross-section, but darker regions, possibly linked to an accumulation of defects, present less defined layers. Looking at the oxide in BF-TEM, it is possible to see two structures, a denser oxide band close to the outer surface, and a less dense oxide characterised by a layered morphology that extends towards the interface with the unoxidized coating. The outer band is probably the main protective oxide, and it appears to be outward growing or re-precipitation from the water, but it does not maintain the morphology of the original coating. The inner band seems instead to be an oxidation front moving towards the bulk of the coating and oxidizing the material layer by layer. The characteristics of this oxide are further confirmed by the STEM image shown in Figure 8-12, and here the larger grains found at the outer surface are more clearly visible. The layered inner oxide seems to present alternating regions where the nanolayers are clearly visible and denser domains where the layers cannot be seen.

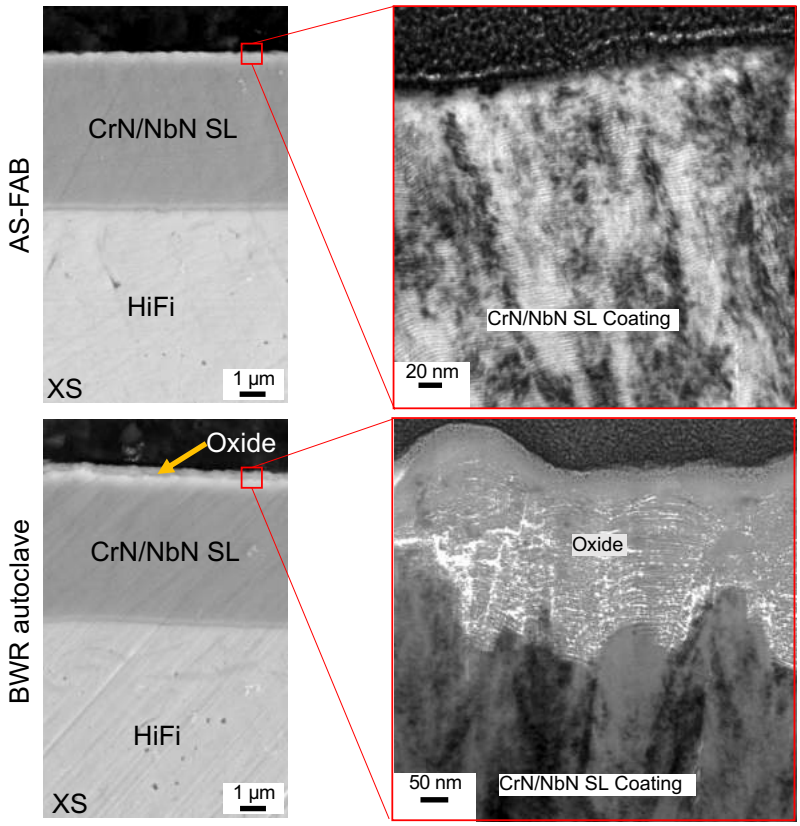

Figure 8-11: SEM images of as-fabricated and autoclaved (BWR) CrN/NbN superlattice coating on HiFi cladding substrate (left). BF-TEM images of the same samples from the region of interest close to the outer surface of the coated cladding (right).

The larger oxide grains at the outer part of the oxide appear to be rich in Nb and Ni, as shown by the STEM-EDS map collected for the same region (see Figure 8-12), and some Cr is still measured in these crystallites. The layered oxide underneath shows a similar composition, but Cr is the predominant metallic element, while Nb and Ni are measured in lower concentrations. Small portions of oxide where some residual N is still present can be found. Overall, the oxygen content measured from SEM-EDS is around 55–60 at.%, with 25–30 at.% Cr, 8–15 at.% Nb, and 4–8 at.% Ni. Traces of Al are also present.

It appears that a Nb-rich oxide phase, potentially less soluble in the BWR water environment, is protecting a Cr-rich oxide below. The formation of a stable Nb-rich oxide ($NbCrO_4$ or a $CrNb_2O_4$ spinel) decreases the oxygen potential that reaches the inner oxide layer, making the inner chromia-like oxide thermodynamically stable. This mechanism is very common in steels and Ni-alloys and allows one to benefit from the chromia as a diffusion barrier to slow down oxidation even in environments where the chromia would not be able to survive. Once these two bands have formed, the oxidation will slowly progress through the layers of the superlattice coating. The importance of the superlattice is difficult to quantify properly, but looking accurately at the oxide-coating interface visible in Figure 8-12, one could conclude that the nanolayers are forcing the oxidation to progress downwards through defects and grain boundaries in the form of oxide protrusions growing into the coating. Once the oxidation front manages to gain ground, it starts oxidising the superlattice layers from the sides, along the CrN-NbN interfaces. One additional hint at the effects of the superlattice layers on the

oxidation mechanics, is the presence of small regions of the oxide scale where N is still present, meaning that O did not fully oxidize these regions and had to travel around them. Ni and Al are not present in the as-fabricated coating and originate from the autoclave water (possibly from the sample holder used to hang the specimens inside the autoclave). The presence of these contaminations represents relatively well the chemical environment found in a real reactor. Most of the tubing and the core vessel are made of stainless steel and dissolution of Fe, Ni, Al and other elements from the steel into the water occurs constantly. These species can redeposit onto the fuel rod as so-called crud and it is very common to observe this phenomenon in LWRs.

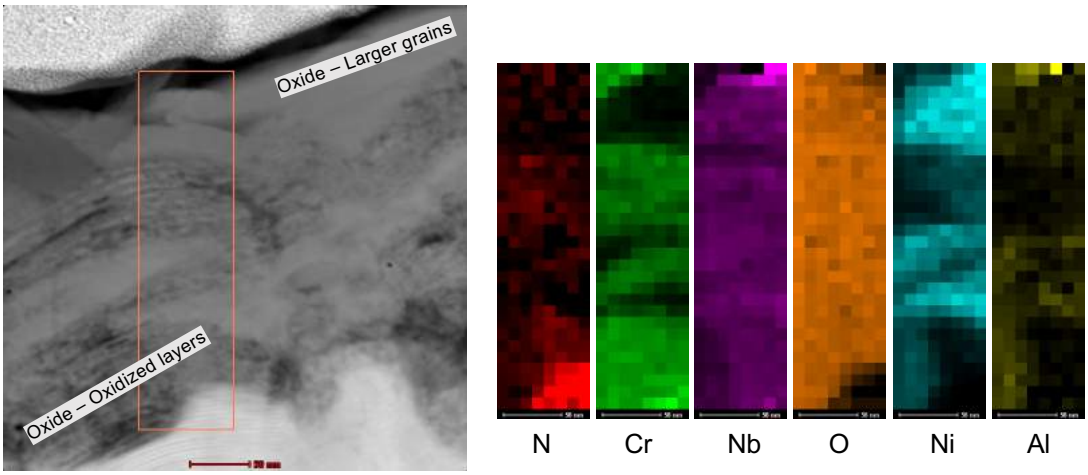

Figure 8-12: STEM-EDS mapping of the oxide scale formed on the surface of the CrN/NbN superlattice coating after 60 days exposure to BWR simulated environment in autoclave.

The superlattice layered structure is not affected by the exposure. As it is shown in the bottom part of the STEM image presented in Figure 8-12, the nanolayers are still visible after exposure. The nanometric thickness of the layers produces certain challenges in capturing the actual chemical composition of each layer using electron microscopy. When working with a lamella it is always possible that the thin layers are slightly tilted with respect to the electron beam, and therefore the signal collected from one of the layers has contributions from material in the other layers. APT can to some extent help to solve this problem, and a 3D reconstruction of the layers measured in the bulk of the as-fabricated coating is displayed in Figure 8-13. Once the reconstruction is obtained, it is possible to select cylindrical volumes perpendicular to the layers and calculate 1D concentration profiles to determine the composition of the different phases. One such composition profile is presented in the lower section of Figure 8-13. From this profile it appears like Layer A (Nb-rich) has a composition of 34 at.% Nb, 16 at.% Cr and 50 at.% N, while Layer B (Cr-rich) has a composition of 60 at.% Cr, 10 at.% Nb, and 30 at.% N. Layer A is compatible with a (Nb, Cr)N chemistry, while Layer B seems closer to a $(Cr, Nb)_2N$ structure. The thickness of the different layers is very similar and uniform across the APT run, but it could be argued that Layer A (Nb-rich) tends to be slightly thicker. As it is visible in the BF-TEM image of the as-fabricated coating reported in Figure 8-11, there are darker areas that could have a different composition and account for this discrepancy.

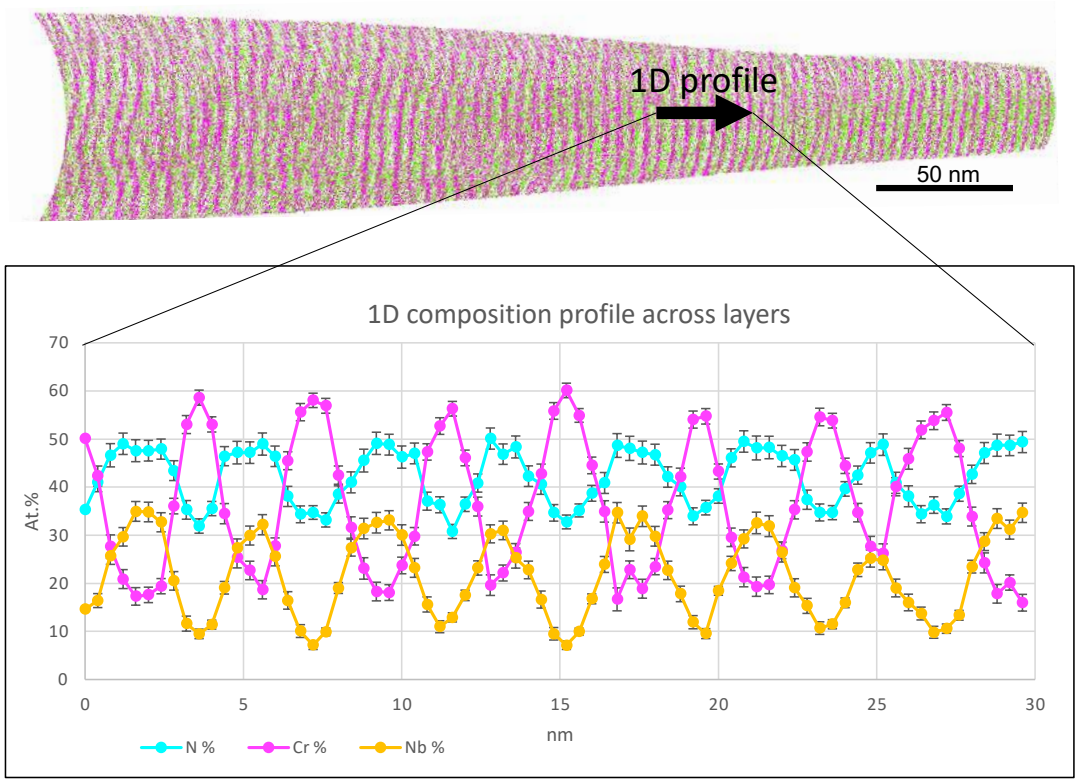

Figure 8-13: APT reconstruction of as-fabricated CrN/NbN superlattice coating material (top, pink is CrN ions, green is NbN ions). 1D concentration profile along a direction perpendicular to the layers (bottom).

CHAPTER 9

CONCLUSIONS

The general conclusion that can be drawn for this work is that coated claddings is a very promising concept and it could allow the nuclear industry to develop and deploy safer and better performing materials without the need to drastically change the design of the fuel assemblies. This will potentially make LWRs safer and more competitive, helping to reduce the emissions of greenhouse gasses and close the gap between a fossil fuel society and one based on renewable sources. More testing and research are needed before these materials can be used in commercial power plants, but the prospects of this technology are bright, and it is reasonable to see coated cladding entering commercial use in the next few years. Extensive in-reactor tests and integral LOCA testing are currently being performed in many facilities around the world, which represent the last steps before the licensing of new nuclear components can be accomplished.

CS-Cr coatings offer clear improvements to the resistance to high-temperature steam corrosion of uncoated Zr-claddings, answering *Question 1.* As an answer to *Question 2,* chromia appears to be stable and effective at passivating the surface of the CS-Cr coating in PWR simulated operating conditions and it is expected to allow CS-Cr coatings to survive under operating conditions for the entire duration of the fuel rod lifetime. However, chromia did not have the required stability in BWR simulated operating conditions. In regards to *Question* 3, the effects of cold spray deposition on the substrate are limited and little interaction occurs between the coating and the substrate during deposition or while at operating temperature. More significant mixing and dissolution of the Cr into the Zr can be seen at 1200 °C, but these processes do not hinder the effectiveness of the coating at this temperature. More specific results and conclusions regarding PWRs and the studies performed on CS-Cr coated claddings are listed below.

CS-Cr coatings offer effective protection under simulated LOCA conditions:

- After 40 min at 1200 °C in flowing steam, an 8 µm thick chromia scale had formed on the outer surface of the Cr-coating. No significant spallation of the oxide scale could be observed. The substrate was effectively protected from oxidation.
- During exposure to high temperatures, Cr and Zr react forming a $(Cr, Fe)_2Zr$ Laves phase layer at the Cr-Zr interface. This layer reaches a maximum of 1.5–1.7 µm in thickness and seems to have a role in slowing down the dissolution of the Cr coating into the Zr alloy.
- The microstructure of the coating, initially severely deformed, is fully recrystallized after the first 3 min of exposure. The obtained microstructure is characterized by large equiaxed grains 5–15 µm in size.
- ZrO_2 particles are found at the grain boundaries of the recrystallized Cr.

CS-Cr coatings offer good oxidation protection in PWR autoclave corrosion test:

- A passivating, 100 nm thick chromia scale forms on the surface of the coated cladding, representing a significant improvement compared to traditional (uncoated) materials.
- Small changes in chemistry and microstructure of the interfacial region take place during autoclave exposure, but neither the nucleation of Laves phase nor the formation of the Zr-Cr-Fe phase can be considered detrimental to the performance.

Cold spray deposition does not modify the substrate properties:

- The formation of a 1–2 µm thick nanocrystalline layer on the Zr side of the Cr-Zr interface is reported, but deemed too thin to modify the properties of the Zr cladding.
- The strong adhesion of the coating seems to originate from mechanical interlocking and from the presence of a 10–20 nm thick intermixed bonding region.

CS-Cr coated cladding performs better than the traditional Optimized ZIRLO cladding and the outlook of this ATF material is very promising.

Finding a coating able to withstand the more oxidizing environment of a BWR during operation has been challenging. In the attempt to answer *Question* 2, it was demonstrated that coatings oxidizing into pure chromia are not suitable for BWR application. After extensive screening, nanolayered CrN/NbN MS-PVD coatings have emerged as potential candidates. The MS-PVD technique does not produce any modification of the substrate, and little interaction between the CrN-NbN coatings and the substrate could be observed, answering *Question 3*. Testing CrN-NbN coatings under simulated accident conditions will be necessary to address *Question 1* regarding this coating design. A detailed description of the most relevant conclusions obtained on this regard are presented as follows:

BWR environment is significantly more oxidizing than PWR environment:

- CrN and TiN performed well in the simulated PWR environment, offering improved oxidation resistance of the cladding under simulated PWR operating conditions.
- In the BWR autoclave corrosion test, CrN was fully dissolved during the 60 days of exposure, and a 2 µm thick layer of ZrO_2 was found on the surface of the cladding.
- The TiN coating oxidized entirely into TiO_2. The formed oxide film was porous, and oxygen managed to reach the substrate, causing oxidation of the substrate.

CrN/NbN superlattice coatings offer good corrosion protection in BWR autoclave:

- After 60 days of BWR autoclave exposure, a 150–200 nm thick, passivating oxide scale has formed on the outer surface of the CrN/NbN coating.
- This oxide is rich in Cr and Nb. Nb seems to be concentrated in the outer layer of the oxide while Cr is more prevalent in the inner oxide.
- No oxidation of the substrate was observed, but 30–50 nm of ZrN were measured at the coating-substrate interface after autoclave exposure.
- The superlattice morphology may play a role in slowing down the oxidation kinetics.

Most of the research questions posed in this work were answered. A summary of the research steps needed to close the gap between research and industrial application is proposed in the next chapter.

CHAPTER 10

FUTURE WORK

The development in ATF is progressing fast, and many universities and companies are currently working on different solutions ranging from the complete substitution of Zr alloys to a variety of coated Zr-claddings. In regard to the coated cladding ATF concept, the main areas where further investigation is needed are:

- Cr-coated Zr-claddings for PWRs
    - In-reactor studies, to understand the effect of irradiation
    - Integral and semi-integral LOCA tests with pre-oxidation
- Coated Zr-claddings for BWRs
    - Identification of a suitable coating
        - ⇒ CrN/NbN SL works well but there is room for optimization
    - Study of material performance under accident conditions
    - In-reactors studies, to study the effect of irradiation

Cr-coated Zr-claddings for PWRs

In the case of PWRs, Cr-coated Zr-claddings is the main design being considered. The natural steps forward for this material are irradiation studies and in-reactor testing. To further examine the interaction of Cr-coatings with the core environment, cladding tubes need to be tested in running reactors. Many additional effects come into play in a real nuclear reactor, such as irradiation or chemical changes in the water, that no simulated environment can reproduce. Irradiation creep, and thermal creep are both important phenomena which can affect the adhesion and the performance of coatings. Hence it will be relevant to test these stresses as well as to guarantee that Cr-coatings will be able to perform throughout the whole life-cycle of a cladding. Obtaining and handling irradiated materials is very challenging due to the added complication of radioactivity and rarity of active test reactors. During an accidental scenario, temperature and steam atmosphere are not the only important parameters. For example, the pre-oxidation of the coating during the operation prior to the accident could play a role in the protection offered to the Zr cladding. For the long-term use of Cr-coatings, studies of the irradiation effects on metallic Cr are crucial. Progressive irradiation induced embrittlement or swelling of the Cr could cause spallation of the coating or modify the way the coating responds to thermal shocks or creep and deformation. These phenomena need to be understood and tested before CS-Cr coatings (or Cr coatings in general) can be used in commercial applications in nuclear reactors.

Coated Zr-claddings for BWRs

When coming to BWRs, the pursuit of a suitable coating is still ongoing, but CrN/NbN coatings are very promising. BWRs have a much higher oxygen content in the cooling water than PWRs, which makes it more challenging for materials to endure. Several versions of CrN/NbN coatings, including advanced superlattice coatings, have been tested, but more characterization is needed to fully understand the role of Nb and of the nanolayered morphology in this system. Once an optimized version of these coatings is identified, the

selected material will need to cover all the steps Cr-coatings have been going through. Samples exposed to simulated accident environment, irradiation and in-reactor conditions will be characterized and compared to the as-fabricated samples in search of interdiffusion between coating and substrate, nucleation and growth of new phases, insights into the oxidation mechanism, and the effects of irradiation. Of great importance are high-temperature studies, since nitride coatings exposed to temperatures above 1000 °C can start decomposing into metal and N_2-gas, threatening the effectiveness of this family of material under accident conditions. Moreover, understanding the effects of N-ingress into the Zr-substrate at operating temperature and, if it is detrimental in any way, how to slow down or stop this phenomenon are necessary steps before these new materials can be considered for a real in-reactor application.

ACKNOWLEDGMENTS

The work presented in this thesis would have not been possible without the amazingly supportive environment we have at the Division of Microstructure Physics. Pointing out people would literally be unfair, since everyone in our division is always ready to invest time and energy in helping a colleague. I hope I was (or will be) able to give back at least as much as I received. I also want to acknowledge our small and beautiful community of atom probers. Here, a friendly and pleasant working environment is combined with decades of accumulated knowledge and experience to create the best place to learn how to do science.

I am really thankful to my supervisor Mattias Thuvander for being a fantastic person and a great manager, as I have always received reasoned feedbacks and thoughtful guidance. I am grateful to Krystyna Stiller and Hans-Olof Andrén for their priceless help in paper writing and conceptualization, and to Mohammad Sattari for the support with all queries related to electron microscopy. Throughout my studies I have received the highest quality supervision. This has been fundamental in helping me develop both as a researcher and as a person, but it does not come for granted, and it is fruit of the great passion and remarkable dedication that my supervisor and co-supervisors have.

Thanks to all CMAL staff for bearing with all the questions and lunch interruptions. Despite the amount of issues researchers and instruments have, they have always been patient and helpful. I am grateful to Torben Boll from Karlsruhe Institute of Technology and to the Karlsruhe Nano Micro Facility for granting us access to an atom probe in the time of need.

My thanks go also to Westinghouse Electric Sweden, particularly to Denise Adorno Lopes, Antoine Claisse and Jonathan Wright for being great industrial partners to work with. Beyond providing samples and materials, the regular interactions and valuable discussions were crucial in developing and steering the direction of my work. The same goes for the community around the SAFETY project, of which my work is only a small part. The scientific discussions held at our biannual meetings have always been very stimulating, and have allowed me to put my research into context and to see the relevance of my work first-hand.

BIBLIOGRAPHY

[1] International Atomic Energy Agency, IAEA Nuclear Power Reactor in the World, (2022).

[2] W.D. Magwood, H. Paillere, Looking ahead at reactor development, Progress in Nuclear Energy. 102 (2018) 58–67. https://doi.org/10.1016/j.pnucene.2017.07.001.

[3] International Energy Agency, Nuclear Power in a Clean Energy System, OECD, 2019. https://doi.org/10.1787/fc5f4b7e-en.

[4] World Nuclear Association, World Nuclear Performance Report 2020, 2020.

[5] R.B. Rebak, Current materials in light water reactors. Why do we need a materials renewal?, in: Accident Tolerant Materials for Light Water Reactor Fuels, Elsevier, 2020: pp. 15–41. https://doi.org/10.1016/B978-0-12-817503-3.00002-X.

[6] K.A. Terrani, Accident tolerant fuel cladding development: Promise, status, and challenges, Journal of Nuclear Materials. 501 (2018) 13–30. https://doi.org/10.1016/j.jnucmat.2017.12.043.

[7] M.G. Fontana, R.W. Staehle, Advances in Corrosion Science and Technology, Springer US, Boston, MA, 1972. https://doi.org/10.1007/978-1-4615-8255-7.

[8] J.P. Foster, H.K. Yueh, R.J. Comstock, M. Limback, B. Kammenzind, S.W. Dean, ZIRLO™ Cladding Improvement, J ASTM Int. 5 (2008) 101188. https://doi.org/10.1520/JAI101188.

[9] IAEA, TECDOC-709: Fuel failure in normal operation of water reactors: experience, mechanisms and management, 1993.

[10] Z. Karoutas, J. Brown, A. Atwood, L. Hallstadius, E. Lahoda, S. Ray, J. Bradfute, The maturing of nuclear fuel: Past to Accident Tolerant Fuel, Progress in Nuclear Energy. 102 (2018) 68–78. https://doi.org/10.1016/j.pnucene.2017.07.016.

[11] C. Vitanza, Discussion on experimental methods to derive LOCA safety limits, International Atomic Energy Agency (IAEA), 2002.

[12] Z. Hozer, A. Griger, L. Matus, L. Vasaros, M. Horvath, Effect of hydrogen content on the embrittlement of ZR alloys, International Atomic Energy Agency (IAEA), 2002.

[13] Yu.K. Bibilashvili, N.B. Sokolov, L.N. Andreeva-Andrievskaya, V.Yu. Tonkov, A. V Salatov, A.M. Morosov, V.P. Smirnov, Thermomechanical properties of zirconium-based alloys oxidized claddings in LOCA simulation conditions, International Atomic Energy Agency (IAEA), 2002.

[14] A.T. Motta, A. Couet, R.J. Comstock, Corrosion of Zirconium Alloys Used for Nuclear Fuel Cladding, (2015). https://doi.org/10.1146/annurev-matsci-070214-020951.

[15] R.B. Adamson, C.E. Coleman, M. Griffiths, Irradiation creep and growth of zirconium alloys: A critical review, Journal of Nuclear Materials. 521 (2019) 167–244. https://doi.org/10.1016/J.JNUCMAT.2019.04.021.

[16] D. Terentyev, A. Zinovev, T. Khvan, J.H. You, N. Van Steenberge, E.E. Zhurkin, Irradiation embrittlement in pure chromium and chromium-tungsten alloy in a view of their potential application for fusion plasma facing components, Journal of Nuclear Materials. 554 (2021) 153086. https://doi.org/10.1016/j.jnucmat.2021.153086.

[17] L.J. Ott, K.R. Robb, D. Wang, Preliminary assessment of accident-tolerant fuels on LWR performance during normal operation and under DB and BDB accident conditions, Journal of Nuclear Materials. 448 (2014) 520–533. https://doi.org/10.1016/j.jnucmat.2013.09.052.

[18] R.B. Rebak, Worldwide development of accident tolerant fuels, areas of study, claddings, and fuels, in: Accident Tolerant Materials for Light Water Reactor Fuels, Elsevier, 2020: pp. 43–62. https://doi.org/10.1016/b978-0-12-817503-3.00003-1.

[19] R.B. Rebak, Accident-tolerant fuels cladding concept: coatings for zirconium alloys, in: Accident Tolerant Materials for Light Water Reactor Fuels, Elsevier, 2020: pp. 63–81. https://doi.org/10.1016/b978-0-12-817503-3.00004-3.

[20] J.C. Brachet, M. le Saux, M. le Flem, S. Urvoy, E. Rouesne, T. Guilbert, C. Cobac, F. Lahogue, J. Rousselot, M. Tupin, P. Billaud, C. Hossepied, F. Schuster, F. Lomello, A. Billard, G. Velisa, E. Monsifrot, J. Bischoff, A. Ambard, On-going studies at CEA on chromium coated zirconium based nuclear fuel claddings for enhanced Accident Tolerant LWRs Fuel, in: TopFuel, 2015: pp. 31–38.

[21] J. Bischoff, C. Delafoy, C. Vauglin, P. Barberis, C. Roubeyrie, D. Perche, D. Duthoo, F. Schuster, J.C. Brachet, E.W. Schweitzer, K. Nimishakavi, AREVA NP's enhanced accident-tolerant fuel developments: Focus on Cr-coated M5 cladding, Nuclear Engineering and Technology. 50 (2018) 223–228. https://doi.org/10.1016/j.net.2017.12.004.

[22] B. Maier, H. Yeom, G. Johnson, T. Dabney, J. Walters, P. Xu, J. Romero, H. Shah, K. Sridharan, Development of cold spray chromium coatings for improved accident tolerant zirconium-alloy cladding, Journal of Nuclear Materials. 519 (2019) 247–254. https://doi.org/10.1016/j.jnucmat.2019.03.039.

[23] J. Bischoff, C. Delafoy, N. Chaari, C. Vauglin, K. Buchanan, P. Barberis, E. Monsifrot, J.-C.B. F. Schuster, K. Nimishakavi, Cr coated cladding Development At Framatome, in: TopFuel, 2018: pp. 1–7.

[24] B. Maier, H. Yeom, G. Johnson, T. Dabney, J. Walters, J. Romero, H. Shah, P. Xu, K. Sridharan, Development of Cold Spray Coatings for Accident-Tolerant Fuel Cladding in Light Water Reactors, JOM. 70 (2018) 198–202. https://doi.org/10.1007/s11837-017-2643-9.

[25] H. Yeom, B.R. Maier, G. Johnson, K. Sridharan, Cold Spray Coatings for Accident Tolerant Zr-Alloy Cladding in Light Water Reactors, in: Trans Am Nucl Soc, 2018: pp. 1576–1579. https://www.researchgate.net/publication/325812110.

[26] R. V. Umretiya, B. Elward, D. Lee, M. Anderson, R.B. Rebak, J. V. Rojas, Mechanical and chemical properties of PVD and cold spray Cr-coatings on Zircaloy-4, Journal of Nuclear Materials. 541 (2020) 152420. https://doi.org/10.1016/j.jnucmat.2020.152420.

[27] J.-C. Brachet, E. Rouesne, J. Ribis, T. Guilbert, S. Urvoy, G. Nony, C. Toffolon-Masclet, M. le Saux, N. Chaabane, H. Palancher, A. David, J. Bischoff, J. Augereau, E. Pouillier, High temperature steam oxidation of chromium-coated zirconium-based alloys: Kinetics and process, Corros Sci. 167 (2020) 108537. https://doi.org/10.1016/j.corsci.2020.108537.

[28] H. Yeom, B. Maier, G. Johnson, T. Dabney, M. Lenling, K. Sridharan, High temperature oxidation and microstructural evolution of cold spray chromium coatings on Zircaloy-4 in steam environments, Journal of Nuclear Materials. 526 (2019) 151737. https://doi.org/10.1016/j.jnucmat.2019.151737.

[29] J. Hazan, A. Gauthier, E. Pouillier, K. Shirvan, Semi-integral LOCA test of cold-spray chromium coated zircaloy-4 accident tolerant fuel cladding, Journal of Nuclear Materials. 550 (2021) 152940. https://doi.org/10.1016/j.jnucmat.2021.152940.

[30] S. Tuzi, K. Göransson, S.M.H. Rahman, S.G. Eriksson, F. Liu, M. Thuvander, K. Stiller, Oxide evolution on Alloy X-750 in simulated BWR environment, Journal of Nuclear Materials. 482 (2016) 19–27. https://doi.org/10.1016/j.jnucmat.2016.09.026.

[31] S. Tuzi, H. Lai, K. Göransson, M. Thuvander, K. Stiller, Corrosion of pre-oxidized nickel alloy X-750 in simulated BWR environment, Journal of Nuclear Materials. 486 (2017) 350–360. https://doi.org/10.1016/j.jnucmat.2017.01.051.

[32] L. Tan, T. Chen, B.A. Pint, Steam oxidation behavior of Ni-base superalloys 690, 725 and X-750 at 600 and 650 °C, Corros Sci. 157 (2019) 487–497. https://doi.org/10.1016/j.corsci.2019.06.014.

[33] A.P. Alkhimov, A.N. Papyrin, U. Vyazemskogo, V.F. Kosarev, N.I. Nesterovich, M.M. Shushpanov, United States Patent - Gas-dynamic spraying method for applying a coating, 1994.

[34] V.K. Champagne, The cold spray materials deposition process, Woodhead Publishing Limited, 2007. https://doi.org/10.1533/9781845693787.

[35] P. Cavaliere, Cold-Spray Coatings: Recent Trends and Future perspectives, Springer, 2017. https://doi.org/10.1007/978-3-319-67183-3.

[36] Y. Xu, I.M. Hutchings, Cold spray deposition of thermoplastic powder, Surf Coat Technol. 201 (2006) 3044–3050. https://doi.org/10.1016/j.surfcoat.2006.06.016.

[37] Y. Ichikawa, R. Tokoro, M. Tanno, K. Ogawa, Elucidation of cold-spray deposition mechanism by auger electron spectroscopic evaluation of bonding interface oxide film, Acta Mater. 164 (2019) 39–49. https://doi.org/10.1016/j.actamat.2018.09.041.

[38] X.T. Luo, Y. Ge, Y. Xie, Y. Wei, R. Huang, N. Ma, C.S. Ramachandran, C.J. Li, Dynamic evolution of oxide scale on the surfaces of feed stock particles from cracking and segmenting to peel-off while cold spraying copper powder having a high oxygen content, J Mater Sci Technol. 67 (2021) 105–115. https://doi.org/10.1016/j.jmst.2020.06.019.

[39] J. Karthikeyan, The advantages and disadvantages of the cold spray coating process, in: The Cold Spray Materials Deposition Process, Woodhead Publishing Limited, 2007: pp. 62–71. https://doi.org/10.1201/9781439824122.ch4.

[40] F.J. Brodmann, Cold spray process parameters: Powders, in: V.K.B.T.-T.C.S.M.D.P. Champagne (Ed.), The Cold Spray Materials Deposition Process: Fundamentals and Applications, Woodhead Publishing, 2007: pp. 105–116. https://doi.org/10.1533/9781845693787.2.105.

[41] X.J. Ning, J.H. Jang, H.J. Kim, The effects of powder properties on in-flight particle velocity and deposition process during low pressure cold spray process, Appl Surf Sci. 253 (2007) 7449–7455. https://doi.org/10.1016/j.apsusc.2007.03.031.

[42] Y. Deng, W. Chen, B. Li, C. Wang, T. Kuang, Y. Li, Physical vapor deposition technology for coated cutting tools: A review, Ceram Int. 46 (2020) 18373–18390. https://doi.org/10.1016/j.ceramint.2020.04.168.

[43] K. Yamamoto, S. Kujime, K. Takahara, Properties of nano-multilayered hard coatings deposited by a new hybrid coating process: Combined cathodic arc and unbalanced magnetron sputtering, Surf Coat Technol. 200 (2005) 435–439. https://doi.org/10.1016/j.surfcoat.2005.02.175.

[44] F. Sanchette, C. Ducros, T. Schmitt, P. Steyer, A. Billard, Nanostructured hard coatings deposited by cathodic arc deposition: From concepts to applications, Surf Coat Technol. 205 (2011) 5444–5453. https://doi.org/10.1016/j.surfcoat.2011.06.015.

[45] I.G. Brown, Cathodic arc deposition of films, Annual Review of Materials Science. 28 (1998) 243–269. https://doi.org/10.1146/annurev.matsci.28.1.243.

[46] K.D. Bouzakis, N. Michailidis, G. Skordaris, E. Bouzakis, D. Biermann, R. M'Saoubi, Cutting with coated tools: Coating technologies, characterization methods and performance optimization, CIRP Annals. 61 (2012) 703–723. https://doi.org/10.1016/j.cirp.2012.05.006.

[47] H. Schulz, H.J. Scheibe, P. Siemroth, B. Schultrich, Pulsed arc deposition of super-hard amorphous carbon films, Applied Physics A 2003 78:5. 78 (2003) 675–679. https://doi.org/10.1007/S00339-003-2280-8.

[48] Y. Qizheng, J. Li, X. Zhihui, P.D. Swift, Macroparticles in films deposited by steered cathodic arc, J Phys D Appl Phys. 29 (1996) 2025. https://doi.org/10.1088/0022-3727/29/7/041.

[49] E. Ertürk, H.J. Heuvel, H.G. Dederichs, Comparison of the steered arc and random arc techniques, Surf Coat Technol. 39–40 (1989) 455–464. https://doi.org/10.1016/S0257-8972(89)80007-6.

[50] K. Yamamoto, T. Sato, K. Takahara, K. Hanaguri, Properties of (Ti,Cr,Al)N coatings with high Al content deposited by new plasma enhanced arc-cathode, Surf Coat Technol. 174–175 (2003) 620–626. https://doi.org/10.1016/S0257-8972(03)00580-2.

[51] W.C. Lang, J.Q. Xiao, J. Gong, C. Sun, R.F. Huang, L.S. Wen, Study on cathode spot motion and macroparticles reduction in axisymmetric magnetic field-enhanced vacuum arc deposition, Vacuum. 84 (2010) 1111–1117. https://doi.org/10.1016/j.vacuum.2010.01.037.

[52] X. Zuo, R. Chen, D. Zhang, P. Ke, A. Wang, Movement of luminous group spots on target and size modification of micro-particles during cathodic vacuum arc deposition, Vacuum. 164 (2019) 381–389. https://doi.org/10.1016/j.vacuum.2019.03.048.

[53] J. Hu, X. Tian, H. Liu, C. Gong, Q. Tian, M. Wu, M. Li, Enhanced discharge and microstructure of the ta-C coatings by electromagnetically enhanced cathodic arc at argon atmosphere, Surf Coat Technol. 365 (2019) 227–236. https://doi.org/10.1016/j.surfcoat.2018.08.020.

[54] Y. Zhao, G. Lin, J. Xiao, W. Lang, C. Dong, J. Gong, C. Sun, Synthesis of titanium nitride thin films deposited by a new shielded arc ion plating, Appl Surf Sci. 257 (2011) 5694–5697. https://doi.org/10.1016/j.apsusc.2011.01.075.

[55] A. Anders, Approaches to rid cathodic arc plasmas of macro- and nanoparticles: a review, Surf Coat Technol. 120–121 (1999) 319–330. https://doi.org/10.1016/S0257-8972(99)00460-0.

[56] A.I. Ryabchikov, D.O. Sivin, A.I. Bumagina, Physical mechanisms of macroparticles number density decreasing on a substrate immersed in vacuum arc plasma at negative high-frequency short-pulsed biasing, Appl Surf Sci. 305 (2014) 487–491. https://doi.org/10.1016/j.apsusc.2014.03.120.

[57] J.M. Schneider, S. Rohde, W.D. Sproul, A. Matthews, Recent developments in plasma assisted physical vapour deposition, J Phys D Appl Phys. 33 (2000) R173. https://doi.org/10.1088/0022-3727/33/18/201.

[58] R.D. Arnell, P.J. Kelly, Recent advances in magnetron sputtering, Surf Coat Technol. 112 (1999) 170–176. https://doi.org/10.1016/S0257-8972(98)00749-X.

[59] J.W. Bradley, T. Welzel, Physics and phenomena in pulsed magnetrons: an overview, J Phys D Appl Phys. 42 (2009) 093001. https://doi.org/10.1088/0022-3727/42/9/093001.

[60] V. Kouznetsov, K. MacÁk, J.M. Schneider, U. Helmersson, I. Petrov, A novel pulsed magnetron sputter technique utilizing very high target power densities, Surf Coat Technol. 122 (1999) 290–293. https://doi.org/10.1016/S0257-8972(99)00292-3.

[61] K. Sarakinos, J. Alami, S. Konstantinidis, High power pulsed magnetron sputtering: A review on scientific and engineering state of the art, Surf Coat Technol. 204 (2010) 1661–1684. https://doi.org/10.1016/j.surfcoat.2009.11.013.

[62] U. Helmersson, M. Lattemann, J. Bohlmark, A.P. Ehiasarian, J.T. Gudmundsson, Ionized physical vapor deposition (IPVD): A review of technology and applications, Thin Solid Films. 513 (2006) 1–24. https://doi.org/10.1016/J.TSF.2006.03.033.

[63] W. Tillmann, D. Kokalj, D. Stangier, Influence of the deposition parameters on the texture and mechanical properties of magnetron sputtered cubic MoNx thin films, Materialia (Oxf). 5 (2019) 100186. https://doi.org/10.1016/j.mtla.2018.100186.

[64] A. Inspektor, P.A. Salvador, Architecture of PVD coatings for metalcutting applications: A review, Surf Coat Technol. 257 (2014) 138–153. https://doi.org/10.1016/j.surfcoat.2014.08.068.

[65] P.H. Mayrhofer, C. Mitterer, L. Hultman, H. Clemens, Microstructural design of hard coatings, Prog Mater Sci. 51 (2006) 1032–1114. https://doi.org/10.1016/j.pmatsci.2006.02.002.

[66] Y.X. Wang, S. Zhang, J.W. Lee, W.S. Lew, B. Li, Influence of bias voltage on the hardness and toughness of CrAlN coatings via magnetron sputtering, Surf Coat Technol. 206 (2012) 5103–5107. https://doi.org/10.1016/j.surfcoat.2012.06.041.

[67] D.A. Golosov, Balanced magnetic field in magnetron sputtering systems, Vacuum. 139 (2017) 109–116. https://doi.org/10.1016/j.vacuum.2017.02.018.

[68] V. Tiron, I.L. Velicu, I. Mihăilă, G. Popa, Deposition rate enhancement in HiPIMS through the control of magnetic field and pulse configuration, Surf Coat Technol. 337 (2018) 484–491. https://doi.org/10.1016/j.surfcoat.2018.01.065.

[69] P.J. Kelly, R.D. Arnell, Magnetron sputtering: a review of recent developments and applications, Vacuum. 56 (2000) 159–172. https://doi.org/10.1016/S0042-207X(99)00189-X.

[70] Y. Wang, L. Wang, L. Shang, G. Bai, J. Li, F. Xue, W. Gong, Fiber texture-dependent oxidation behaviour of Cr-coated zirconium alloy in high temperature steam, Corros Sci. 205 (2022) 110449. https://doi.org/10.1016/j.corsci.2022.110449.

[71] B.N. Popov, Chapter 1 - Evaluation of Corrosion, in: B.N.B.T.-C.E. Popov (Ed.), Elsevier, Amsterdam, 2015: pp. 1–28. https://doi.org/10.1016/B978-0-444-62722-3.00001-X.

[72] B.N. Popov, Chapter 2 - Thermodynamics in the Electrochemical Reactions of Corrosion, in: B.N.B.T.-C.E. Popov (Ed.), Elsevier, Amsterdam, 2015: pp. 29–92. https://doi.org/10.1016/B978-0-444-62722-3.00002-1.

[73] B.N. Popov, Chapter 3 - Electrochemical Kinetics of Corrosion, in: B.N.B.T.-C.E. Popov (Ed.), Elsevier, Amsterdam, 2015: pp. 93–142. https://doi.org/10.1016/B978-0-444-62722-3.00003-3.

[74] B.N. Popov, Chapter 4 - Passivity, in: B.N.B.T.-C.E. Popov (Ed.), Elsevier, Amsterdam, 2015: pp. 143–179. https://doi.org/10.1016/B978-0-444-62722-3.00004-5.

[75] B.N. Popov, Chapter 11 - High-Temperature Corrosion, in: B.N.B.T.-C.E. Popov (Ed.), Elsevier, Amsterdam, 2015: pp. 481–523. https://doi.org/10.1016/B978-0-444-62722-3.00011-2.

[76] B. Beverskog, I. Puigdomenech, Revised pourbaix diagrams for chromium at 25–300 °C, Corros Sci. 39 (1997) 43–57. https://doi.org/10.1016/S0010-938X(97)89244-X.

[77] W.G. Cook, R.P. Olive, Pourbaix diagrams for chromium, aluminum and titanium extended to high-subcritical and low-supercritical conditions, Corros Sci. 58 (2012) 291–298. https://doi.org/10.1016/j.corsci.2012.02.002.

[78] D. Cubicciotti, Potential-pH diagrams for alloy-water systems under LWR conditions, Journal of Nuclear Materials. 201 (1993) 176–183. https://doi.org/10.1016/0022-3115(93)90173-V.

[79] M. Hänsel, W.J. Quadakkers, D.J. Young, Role of Water Vapor in Chromia-Scale Growth at Low Oxygen Partial Pressure, Oxidation of Metals 2003 59:3. 59 (2003) 285–301. https://doi.org/10.1023/A:1023040010859.

[80] S. Henry, J. Mougin, Y. Wouters, J.P. Petit, A. Galerie, Characterization of chromia scales grown on pure chromium in different oxidizing atmospheres, Materials at High Temperatures. 17 (2000) 231–234. https://doi.org/10.1179/mht.2000.17.2.008.

[81] S. Mahboubi, H.S. Zurob, G.A. Botton, J.R. Kish, Effect of water vapour partial pressure on the chromia (Cr2O3)-based scale stability, Canadian Metallurgical Quarterly. 57 (2018) 89–98. https://doi.org/10.1080/00084433.2017.1373968.

[82] L. Latu-Romain, Y. Parsa, S. Mathieu, M. Vilasi, Y. Wouters, Chromia Scale Thermally Grown on Pure Chromium Under Controlled p(O2) Atmosphere: II—Spallation Investigation Using Photoelectrochemical Techniques at a Microscale, Oxidation of Metals. 90 (2018) 267–277. https://doi.org/10.1007/s11085-018-9848-3.

[83] S. Mahboubi, Y. Jiao, W. Cook, W. Zheng, D.A. Guzonas, G.A. Botton, J.R. Kish, Stability of Chromia (Cr2O3)-Based Scales Formed During Corrosion of Austenitic Fe-Cr-Ni Alloys in Flowing Oxygenated Supercritical Water, Corrosion. 72 (2016) 1170–1180. https://doi.org/10.5006/1982.

[84] I. Idarraga-Trujillo, M. le Flem, J.C. Brachet, M. le Saux, D. Hamon, S. Muller, V. Vandenberghe, M. Tupin, E. Papin, E. Monsifrot, A. Billard, F. Schuster, Assessment at CEA of coated nuclear fuel cladding for LWRS with increased margins in loca and beyond loca conditions, LWR Fuel Performance Meeting, Top Fuel 2013. 2 (2013) 860–867.

[85] J.-C. Brachet, I. Idarraga-Trujillo, M. Le Flem, M. Le Saux, V. Vandenberghe, S. Urvoy, E. Rouesne, T. Guilbert, C. Toffolon-Masclet, M. Tupin, C. Phalippou, F. Lomello, F. Schuster, A. Billard, G. Velisa, C. Ducros, F. Sanchette, Early studies on Cr-Coated Zircaloy-4 as enhanced accident tolerant nuclear fuel claddings for light water reactors, Journal of Nuclear Materials. 517 (2019) 268–285. https://doi.org/10.1016/j.jnucmat.2019.02.018.

[86] D. Caplan, M. Cohen, The Volatilization of Chromium Oxide, J Electrochem Soc. 108 (1961) 438. https://doi.org/10.1149/1.2428106.

[87] H. Asteman, J.E. Svensson, L.G. Johansson, M. Norell, Indication of chromium oxide hydroxide evaporation during oxidation of 304L at 873 K in the presence of 10% water vapor, Oxidation of Metals. 52 (1999) 95–111. https://doi.org/10.1023/a:1018875024306.

[88] H.J.T. Ellingham, Reducibility of oxides and sulphides in metallurgical processes, J. Soc. Chem. Ind. 63 (1944) 125–160.

[89] D.A. Porter, K.E. Easterling, Phase Transformations in Solids, Van Nostrand Reinhold Co. Ltd., Berkshire, England, 1981.

[90] G.M. Hood, R.J. Schultz, Tracer diffusion in α-Zr, Acta Metallurgica. 22 (1974) 459–464. https://doi.org/10.1016/0001-6160(74)90098-4.

[91] G.M. Hood, Point defect diffusion in α-Zr, Journal of Nuclear Materials. 159 (1988) 149–175. https://doi.org/10.1016/0022-3115(88)90091-8.

[92] R. v. Patil, G.P. Tiwari, B.D. Sharma, Self-diffusion in Zr-Cr and Zr-Fe alloys, Philosophical Magazine A: Physics of Condensed Matter, Structure, Defects and Mechanical Properties. 44 (1981) 717–733. https://doi.org/10.1080/01418618108236174.

[93] F. Seitz, On the porosity observed in the Kirkendall effect, Acta Metallurgica. 1 (1953) 355–369. https://doi.org/10.1016/0001-6160(53)90112-6.

[94] J. Han, S.L. Thomas, D.J. Srolovitz, Grain-boundary kinetics: A unified approach, Prog Mater Sci. 98 (2018) 386–476. https://doi.org/10.1016/j.pmatsci.2018.05.004.

[95] G. Gottstein, L.S. Shvindlerman, B. Zhao, Thermodynamics and kinetics of grain boundary triple junctions in metals: Recent developments, Scr Mater. 62 (2010) 914–917. https://doi.org/10.1016/j.scriptamat.2010.03.017.

[96] N. Hansen, D. Juul Jensen, Deformed metals - Structure, recrystallisation and strength, Materials Science and Technology. 27 (2011) 1229–1240. https://doi.org/10.1179/1743284711Y.0000000046.

[97] F. Najafkhani, S. Kheiri, B. Pourbahari, H. Mirzadeh, Recent advances in the kinetics of normal/abnormal grain growth: a review, Archives of Civil and Mechanical Engineering. 21 (2021) 29. https://doi.org/10.1007/s43452-021-00185-8.

[98] A.S. Argon, Mechanical properties of single-phase crystalline media: deformation at low temperatures, in: Physical Metallurgy, Elsevier, 1996: pp. 1877–1955.

[99] N. Hansen, C.Y. Barlow, Plastic Deformation of Metals Physical Metallurgy 5th edition ed. DE Laughlin and K Hono, Elsevier, 2014.

[100] M.F. Ashby, H. Shercliff, D. Cebon, Materials: engineering, science, processing and design, Butterworth-Heinemann, 2018.

[101] M. Grujicic, Particle/substrate interaction in the cold-spray bonding process, in: The Cold Spray Materials Deposition Process, Woodhead Publishing Limited, 2007: pp. 148–177. https://doi.org/10.1201/9781439824122.ch9.

[102] O. Bielousova, J. Kocimski, R.G. Maev, I. Smurov, W. Scharff, V. Leshchynsky, Localisation of deformation in cold gas dynamic spraying, Surface Engineering. 32 (2016) 655–662. https://doi.org/10.1179/1743294415Y.0000000059.

[103] H. Assadi, F. Gärtner, T. Stoltenhoff, H. Kreye, Bonding mechanism in cold gas spraying, Acta Mater. 51 (2003) 4379–4394. https://doi.org/10.1016/S1359-6454(03)00274-X.

[104] C. Lee, J. Kim, Microstructure of Kinetic Spray Coatings: A Review, Journal of Thermal Spray Technology. 24 (2015) 592–610. https://doi.org/10.1007/s11666-015-0223-5.

[105] M. Grujicic, C.L. Zhao, W.S. DeRosset, D. Helfritch, Adiabatic shear instability based mechanism for particles/substrate bonding in the cold-gas dynamic-spray process, Mater Des. 25 (2004) 681–688. https://doi.org/10.1016/j.matdes.2004.03.008.

[106] J.I. Goldstein, D.E. Newbury, J.R. Michael, N.W.M. Ritchie, J.H.J. Scott, D.C. Joy, Scanning electron microscopy and x-ray microanalysis, Springer, 2017. https://doi.org/10.1007/978-1-4939-6676-9.

[107] W. Zhou, Z.L. Wang, Scanning microscopy for nanotechnology: Techniques and applications, Springer New York, New York, NY, 2007. https://doi.org/10.1007/978-0-387-39620-0.

[108] A.J. Schwartz, M. Kumar, B.L. Adams, eds., Electron Backscatter Diffraction in Materials Science, Springer US, Boston, MA, 2000. https://doi.org/10.1007/978-1-4757-3205-4.

[109] D.B. Williams, C.B. Carter, Transmission electron microscopy: A textbook for materials science, 2009. https://doi.org/10.1007/978-0-387-76501-3.

[110] C.B. Carter, D.B. Williams, Transmission electron microscopy: Diffraction, imaging, and spectrometry, Springer US, Boston, MA, 2016. https://doi.org/10.1007/978-3-319-26651-0.

[111] M.K. Miller, R.G. Forbes, Atom-probe tomography: The local electrode atom probe, Springer US, Boston, MA, 2014. https://doi.org/10.1007/978-1-4899-7430-3.

[112] M.K. Miller, Atom Probe Tomography, Springer US, Boston, MA, 2000. https://doi.org/10.1007/978-1-4615-4281-0.

[113] B. Gault, M.P. Moody, J.M. Cairney, S.P. Ringer, Atom Probe Microscopy, Springer New York, New York, NY, 2012. https://doi.org/10.1007/978-1-4614-3436-8.

[114] O.C. Hellman, D.N. Seidman, Measurement of the Gibbsian interfacial excess of solute at an interface of arbitrary geometry using three-dimensional atom probe microscopy, Materials Science and Engineering A. 327 (2002) 24–28. https://doi.org/10.1016/S0921-5093(01)01885-8.

[115] B. Gault, M.P. Moody, J.M. Cairney, S.P. Ringer, Atom Probe Microscopy and Materials Science, in: Springer New York, New York, NY, 2012: pp. 299–311. https://doi.org/10.1007/978-1-4614-3436-8_9.

[116] R.M. Langford, M. Rogers, In situ lift-out: Steps to improve yield and a comparison with other FIB TEM sample preparation techniques, Micron. 39 (2008) 1325–1330. https://doi.org/10.1016/j.micron.2008.02.006.

[117] K. Thompson, D. Lawrence, D.J. Larson, J.D. Olson, T.F. Kelly, B. Gorman, In situ site-specific specimen preparation for atom probe tomography, Ultramicroscopy. 107 (2007) 131–139. https://doi.org/10.1016/j.ultramic.2006.06.008.

[118] L.A. Giannuzzi, F.A. Stevie, Introduction to focused ion beams: Instrumentation, theory, techniques and practice, Springer, 2005. https://doi.org/10.1007/b101190.

[119] D. Tomus, H.P. Ng, In situ lift-out dedicated techniques using FIB-SEM system for TEM specimen preparation, Micron. 44 (2013) 115–119. https://doi.org/10.1016/j.micron.2012.05.006.

[120] J. Wei, P. Frankel, E. Polatidis, M. Blat, A. Ambard, R.J. Comstock, L. Hallstadius, D. Hudson, G.D.W. Smith, C.R.M. Grovenor, M. Klaus, R.A. Cottis, S. Lyon, M. Preuss, The effect of Sn on autoclave corrosion performance and corrosion mechanisms in Zr-Sn-Nb alloys, Acta Mater. 61 (2013) 4200–4214. https://doi.org/10.1016/j.actamat.2013.03.046.

[121] M. Kopeć, O. Pašta, M. Malá, P. Halodová, L. Cvrček, J. Krejčí, On Debris-Fretting Impact—The Study of Oxide and Chromium Layer Application, Journal of Nuclear Engineering and Radiation Science. 7 (2021). https://doi.org/10.1115/1.4048239.

[122] G. Koster, M. Huijben, G. Rijnders, Oxide superlattices by PLD: A practical guide, Metal Oxide-Based Thin Film Structures. (2018) 27–52. https://doi.org/10.1016/B978-0-12-811166-6.00002-9.